Defect chemistry and thermoelectric behavior of *n*-type $Sr_xBa_{1-x}Nb_2O_6$

Christopher S. Dandeneau

A dissertation

submitted in partial fulfillment of the

requirements for the degree of

Doctor of Philosophy

University of Washington

2015

Reading Committee:

Fumio S. Ohuchi, Chair

Marjorie A. Olmstead

Jihui Yang

Rajendra K. Bordia

Program Authorized to Offer Degree:

Materials Science and Engineering

University of Washington

Abstract

Defect chemistry and thermoelectric behavior of *n*-type $Sr_xBa_{1-x}Nb_2O_6$

Christopher S. Dandeneau

Chair of the Supervisory Committee:
Professor Fumio S. Ohuchi
Materials Science and Engineering

Complex oxides with an intricate atomic structure and tunable stoichiometry are promising materials for use in high-temperature thermoelectric (TE) generators. Among this class of ceramics, highly disordered relaxor ferroelectrics are particularly interesting due to their very low thermal conductivity (κ), which serves to increase the dimensionless figure of merit (ZT). In this work, the defect chemistry and TE behavior of the *n*-type relaxor $Sr_xBa_{1-x}Nb_2O_6$ (SBN100*x*) were investigated. A solution combustion synthesis (SCS) route was first devised to fabricate SBN nanoparticles with excellent phase purity. X-ray photoelectron spectroscopy (XPS) data obtained for various SBN compositions confirmed that Sr atoms occupy two positions in the tetragonal tungsten bronze SBN lattice; a higher binding energy state was associated with Sr ions at pentagonal (A2) sites, presumably due to their increased coordination over Sr at tetragonal (A1) positions. Reduction heat treatments were carried out to raise the electrical conductivity (σ) of sintered SBN50 specimens, and a decrease in the average Nb valence was observed through the growth of lower binding energy Nb 3*d* XPS peaks. Both the Ba 3*d* photoemission and the A2

component of the Sr 3*d* spectra show shifting to lower binding energy as the reduction time is increased, indicating possible preferential oxygen vacancy formation adjacent to A2 sites. Electron transport by variable range hopping was identified at low temperatures (105 – 150 K), followed by a transition to small polaron hopping from 230 to ~550 K. Above ~550 K, the temperature dependence of σ becomes metallic-like (i.e., $d\sigma/dT < 0$), consistent with an Anderson transition; such a scenario is supported by high-temperature Seebeck coefficient (S) measurements. Based on the identified behavior, polymethylmethacrylate (PMMA) pore formers were utilized with the goal of decreasing κ through enhanced phonon scattering while preserving the electron transport characteristics. With the introduction of PMMA into SBN50 prior to sintering, κ was reduced by an average of 44%, and a slight increase in the power factor ($S^2\sigma$) was observed. Ultimately, a substantial increase in ZT by ~128% on average (peak value of 0.14 at 873 K) was achieved for SBN50 processed with 5 wt% PMMA.

TABLE OF CONTENTS

Chapter 1. Introduction and Project Objectives 1

1.1. Motivation for research 1

1.2. Project objectives and dissertation overview 5

Chapter 2. Theory and Background 8

2.1. Review of thermoelectric phenomena 8

2.2. Summary of thermoelectric oxide research 17

2.3. SBN: Properties and thermoelectric behavior 24

Chapter 3. Experimental Procedures 32

3.1. Sample fabrication and reduction 32

3.2. Specimen characterization 34

3.3. Thermoelectric property measurements 35

Chapter 4. Structure and Morphology of SBN 38

4.1. Particle size and structure analysis 38

4.2. Morphological examination 43

Chapter 5. X-ray Photoelectron Spectroscopy Analysis 47

5.1. Unreduced SBN with different Sr:Ba ratios 47

5.2. Reduced SBN photoemission 49

Chapter 6. Thermoelectric Performance of Reduced SBN 54

6.1. Variation of the reduction temperature 54

6.2. Variation of the Sr:Ba ratio 59

6.3. Variation of the reduction time 61

6.4. Electrical transport mechanisms 62

6.5. Effect of pore formers 79

6.6. Stability of reduced SBN 83

Chapter 7. Conclusions 88

7.1. Summary of research findings 88

7.2. Areas for future work 92

Appendix A. Sol-gel fabrication of SBN50 94

Appendix B. Sinter-forging of SBN 97

Appendix C. SBN with a bi-modal grain distribution 99

References 101

LIST OF FIGURES

Figure 1.1. (a) Illustration of the Seebeck effect in an *n*-type semiconductor. The diffusion of more energetic electrons from the hot side (T_{hot}) towards the cooler side gives rise to a potential gradient (ΔV). Figure redrawn from the work of T. Tritt.[4] (b) Schematic of a TE generator; the buildup of positive and negative charges at the base of the *p*- and *n*-type legs, respectively, allows for current flow and the generation of electrical power. 2

Figure 2.1. An illustration of one experiment conducted by Seebeck.[38] A bent piece of copper (K) forms a closed loop with a bismuth block at junctions A and B. Heating one junction causes deflection of a magnetic needle with poles N and S. 8

Figure 2.2. Schematic illustrations of charge flow in *n*- and *p*-type materials under a positive thermal gradient. (a) A negative Seebeck coefficient results in a positive J_{diff} and a net flow of electrons in the opposite direction, down the thermal gradient, as is consistent with an *n*-type material. (b) Positive *S* values produce negative diffusion current densities and a net flow of holes down the temperature gradient, in agreement with the behavior of *p*-type materials. 10

Figure 2.3. A schematic of a TE cooling device. Electrons and holes are represented by solid and open circles, respectively. 11

Figure 2.4. The parameters of *ZT* versus the carrier concentration; interrelationships among the factors make *ZT* optimization difficult. Figure redrawn from the work of Shakouri.[1] 14

Figure 2.5. An illustration of the Na_xCoO_2 crystal structure; pathways for electrical conduction are provided by CoO_2 layers (blue octahedra), while disordered planes of Na atoms (red) serve to scatter phonons. Figure redrawn from research by Li *et al*.[72] 18

Figure 2.6. Bar chart showing the yearly total of peer-reviewed articles according to a topical search for "thermoelectric oxides".[78] 19

Figure 2.7. Schematic of the SBN crystal structure with detailed views of the 12-fold coordinated tetragonal A1 (top right) and 15-fold coordinated pentagonal A2 (bottom right) sites. 25

Figure 2.8. A plot of the dielectric constant with respect to temperature for a sintered SBN50 pellet; the data were acquired at a frequency of 100 Hz. 26

Figure 3.1. A diagram of the SCS procedure for fabricating SBN50 powder. 32

Figure 4.1. TEM image obtained for as-processed SBN50 powder. 38

Figure 4.2. XRD patterns obtained for SBN50 powder samples after calcination at various temperatures. 39

Figure 4.3. (a) XRD patterns of sintered SBN20, 30, 50, and 61 pellets; all samples were found to be single phase with the TTB structure. (b) Close-up view of the patterns in (a); an increase in Sr content leads to a reduction in the lattice parameters and a shift in the XRD peaks to higher 2θ angles. 41

Figure 4.4. XRD patterns for SBN50 after reduction in (a) Ar/H_2 for 25 h and (b) N_2/H_2 for 3, 10, and 25 h; the pattern for unreduced, single-phase SBN50 is included for comparison. 42

Figure 4.5. SEM images obtained for SBN50 pellets sintered at (a) 1275 °C and (b) 1250 °C. Abnormal grain growth is observed at the 1275 °C sintering temperature, while the sample sintered at 1250 °C exhibits a morphology with equiaxed grains. 44

Figure 4.6. SEM images obtained for SBN50 sintered at 1250 °C for (a)-(b) 4 h and (c)-(d) 24 h. The inset of (c) shows an image acquired at a different region of the 24 h sample; abnormal grain growth is evident. 46

Figure 5.1. (a) Sr $3d_{5/2}$ XPS spectra for SBN with different Sr:Ba ratios; the relative A1 (open circles) and A2 (closed circles) peak intensities with respect to the Sr fraction are shown in the inset. (b) Ba $3d_{5/2}$ XPS results for the samples in (a). 48

Figure 5.2. The Nb $3d_{5/2}$ spectra for SBN50 reduced for 2 h at various temperatures before (top) and after (bottom) subtraction of the Nb^{5+} peaks..... 50

Figure 5.3. (a) Nb $3d_{5/2}$ XPS results for SBN50 before annealing and after reduction in N_2/H_2 for 3, 10, and 25 h (solid black lines); the spectrum obtained on the exterior after annealing in N_2/H_2 for 25 h is also shown (red dotted line) along with the Nb $3d_{5/2}$ photoemission after reduction in Ar/H_2 for 25 h (solid blue line). (b) Portion of the XPS survey spectra obtained at the exterior of SBN50 after reduction in N_2/H_2 for various time durations; the position of the N 1*s* peak is denoted with a red dotted line. 51

Figure 5.4. (a) Sr $3d_{5/2}$ and (b) Ba $3d_{5/2}$ XPS spectra after reduction in N_2/H_2 for various time durations. (c) Sr $3d_{5/2}$ XPS spectra obtained before annealing and after reduction in Ar/H_2 for 25 h. 52

Figure 6.1. (a) Magnitude of the Seebeck coefficient, (b) electrical conductivity, and (c) power factor of SBN50 pellets reduced at 900 – 1150 °C. 55

Figure 6.2. (a) The thermal conductivity of as-sintered (unreduced) and reduced (1000 °C) SBN50 with respect to temperature. (b) The dimensionless figure of merit (*ZT*) of SBN50 reduced at 1000 °C with respect to temperature. 56

Figure 6.3. Plots of $\ln(\sigma)$ vs. $10^4/T_{Re}$, where T_{Re} is the reduction temperature and σ is the electrical conductivity of the samples at various testing temperatures. 59

Figure 6.4. (a) Power factor, (b) thermal conductivity, and (c) *ZT* values obtained for SBN30, 50, and 61 specimens reduced for 3 h at 1000 °C. 60

Figure 6.5. (a) Magnitude of the Seebeck coefficient, (b) electrical conductivity, and (c) power factor obtained for SBN50 reduced at 1000 °C for various times. 61

Figure 6.6. (a) Magnitude of the Seebeck coefficient (b) electrical conductivity, and (c) power factor obtained for SBN50 (solid black circles) and CBN18 (solid blue squares) reduced for 25 h at 1000 °C. 65

Figure 6.7. The electrical conductivity of SBN61[001] single crystals after reduction at 1000 °C for different time durations. 66

Figure 6.8. (a) Electrical conductivity and (b) $|S|$ with respect to temperature for an SBN50 sample reduced at 1000 °C for 25 h; two separate regions can be identified in the σ-T plot based on the value of $d\sigma/dT$. 67

Figure 6.9. Plots of $\ln(\sigma T^s)$ vs. $10^3/T$ generated with the electrical conductivity data in Figure 6.8(a); fitting was performed in the temperature range of 300 – 545 K. The exponent s = 1 for adiabatic hopping (solid black circles) and 3/2 for non-adiabatic hopping (solid blue squares). 68

Figure 6.10. Plots of (a) $\ln(\sigma T)$ vs $10^3/T$ (SPH model) and (b) $\ln\sigma$ vs. $T^{-1/4}$ (VRH model) from 105 to 300 K for SBN50 reduced at 1000 °C for 25 h in N_2/H_2. The lines in (a) and (b) were generated by fitting data from 230 – 300 K and 105 – 150 K, respectively. 71

Figure 6.11. An array of potential wells with (a) no random potential and a bandwidth of B and (b) a disorder-induced random potential with mean U_0. The lattice spacing a remains unchanged, but disorder induces broadening of the density of states (right). Figure was redrawn from the work of Mott.[186] 75

Figure 6.12. Proposed density of states for reduced SBN. An impurity band formed from oxygen vacancy donor states overlaps with the Nb 4d conduction band; the Fermi level resides in the pseudogap formed between the two bands. Localized states (shaded regions) are separated from free electron states by a mobility edge in the Nb 4d conduction band. 76

Figure 6.13. Plots of $|S|$ vs. $\ln(T)$ for (a) polycrystalline SBN50 and (b) single crystalline SBN61; both samples were reduced for 25 h. Excellent linear fits to the data were obtained from 615 – 955 K. 78

Figure 6.14. XPS data obtained for SBN50 specimens reduced for 1 and 25 h. The appearance of a peak centered around 1.5 eV in the 25 h sample may be due to photoemission from the impurity band described in Figure 6.12. 79

Figure 6.15. (a) Seebeck coefficient, (b) electrical conductivity, and (c) power factor obtained for reduced SBN50 with (solid blue squares) and without (solid black circles) the use of PMMA pore formers. 80

Figure 6.16. (a) Thermal conductivity and (b) ZT obtained for reduced SBN50 processed with (solid blue squares) and without (solid black circles) PMMA pore formers. 81

Figure 6.17. SEM images obtained at different locations for SBN50 prepared (a)-(b) with PMMA and (c)-(d) no PMMA. Numerous pores with different sizes are evident (a)-(b) due to the vaporization of PMMA during sintering. 82

Figure 6.18. Weight gain and temperature profile for SBN50 powder reduced for 5 h in N_2/H_2(5%). 84

Figure 6.19. (a) Electrical conductivity of the sample in Figure 6.8 during the initial (black circles), second (blue squares), and third (red diamonds) TE tests; the σ values obtained during heating are denoted with filled markers, while those measured during cooling are represented by open markers. (b) Seebeck coefficients obtained for the

samples in (a) during heating. (c) Plot of ln(σT) vs. $10^3/T$ generated with σ data from (a); only the results from the heating portion of the tests are shown. 85

Figure 6.20. (a) Electrical conductivity and (b) Seebeck coefficient obtained for an SBN50 sample reduced at 1000 °C for 25 h in N_2/H_2; values were obtained as the specimen was heating to and cooled from 460, 560, 660, and 770 K. 87

ACKNOWLEDGEMENTS

The author would like to thank the Department of Energy (Grant #: DE-FE0007272) for providing the financial support necessary to conduct the research contained herein.

To Prof. Fumio Ohuchi: There are quite simply not enough superlatives to describe your abilities as both a mentor and an educator. From encouraging rigorous academic debate and independent thought, to your seemingly limitless capacity to employ creativity while adhering to sound scientific methods, you embody all that is good about institutions of higher learning. It has been an honor to work under your guidance, and I can only hope that this project will not be our last collaboration.

To Prof. Marjorie Olmstead: Your brilliance in understanding complex phenomena, as well as the passion and enthusiasm with which you convey such knowledge, led me to have more moments of clarity during this research than I can count. Moreover, I hope to someday emulate the way you adeptly handle the responsibilities of a tenured professor while remaining selflessly devoted to your family.

To Prof. Jihui Yang: The learning curve I encountered at the start of this project was made much smoother by your ability to explain thermoelectric concepts with proficiency and ease. Thank you for your willingness to engage in discussion, as well as your generosity in allowing us access to your lab; the MSE department at UW is much better as a whole with you among its faculty.

To Prof. Raj Bordia: From our interactions over the course of this research, I had the privilege of working with a true expert in their field. There never seemed to be an aspect of ceramics with which you were unfamiliar, and your consistent, on-point questioning during our meetings was crucial in moving the project forward. I would relish the opportunity to work with you again in the future.

To YiHsun Yang: There are many adjectives one could use when describing my demeanor, but I doubt "easy-going" would be among them. The fact that we have remained friends during my time here speaks volume about your patience. It has been a pleasure to see you meet a lovely woman, get married, and raise a beautiful son. You will no doubt excel in whatever path you choose after graduate school.

To Ben Krueger: Our interactions on both a social and academic level made my time at UW much more fulfilling. Your willingness to help others, even during the busiest of times, is a testament to your character. I will miss our intense and fruitful brainstorming sessions, but take solace in having forged a close friendship with a kindred spirit.

To Yzabel: Since the moment we met on that plane to Long Beach, my thoughts on what is truly important in life changed. With your kind heart, devotion to family, and fierce determination to make the world a better place, I look at you and see the best qualities of humanity. Mahal kita.

To my parents: There was a time when I perceived life as a series of highs and lows where, as one grows older, the undulations become less severe in a sort of regression to an average (and hopefully, content) state. Eventually, I have come to see such a viewpoint as ridiculous, since the degree in which an event is considered tragic or joyous is a matter of perspective, and it is our mental outlook that is transformed as we acquire wisdom from experience. I guess my point is that, while many of my beliefs may change with the passage of time, there is one thing about which I am absolutely certain: I was extremely fortunate to be raised by the two most extraordinary parents who provided nothing short of unconditional love and support. I am eternally grateful to you both.

Chapter 1. Introduction and Project Objectives

1.1. Motivation for research

The depletion of fossil fuel supplies and concerns over the environment have spurred research into sustainable energy technologies. One abundant source for low-cost sustainable energy is waste heat. It has been stated that nearly 60% of the energy produced in the United States is dissipated into the environment as heat rather than reused for practical purposes.[1] As such, waste heat recovery mechanisms have been explored to recycle the heat generated from various sources, including factories and automobiles.[2] A possibly strategy for recovering waste heat is to utilize a thermoelectric (TE) generator, whereby heat is converted to electrical energy via the Seebeck effect.[3] Shown in Figure 1.1(a) is a schematic illustration of the Seebeck effect for a typical *n*-type semiconductor.[4] The existence of a temperature gradient across the material will give rise to a larger concentration of more energetic electrons on the high-temperature side (T_{hot}) in accordance with Fermi-Dirac statistics. These electrons will have a longer mean free path and thus, there is a net diffusion of electrons from the higher temperature region into the cooler region of the material. This process continues until the electric field established as a result of electron migration to the cold side and the exposure of positive ion cores on the hot side is of sufficient magnitude so as to oppose further diffusion. The relevant parameter used to characterize the potential difference (ΔV) across the material in the presence of a temperature gradient (ΔT) is known as the Seebeck coefficient, defined as $S = \Delta V/\Delta T$. Figure 1.1(b) shows how the Seebeck effect is exploited in a TE generator. Here, a thermal gradient across the length of the *p*- and *n*-type legs of the device leads to a buildup of positive and negative charges at the base of the respective materials. This in turn allows for the flow of current and the generation of electrical power.

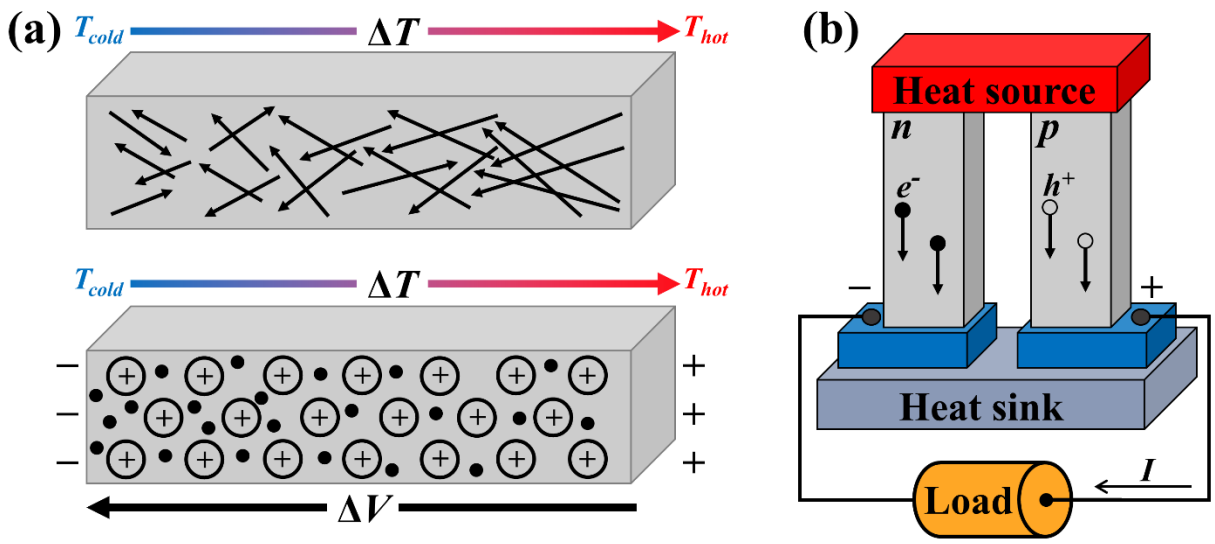

Figure 1.1. (a) Illustration of the Seebeck effect in an *n*-type semiconductor. The diffusion of more energetic electrons from the hot side (T_{hot}) towards the cooler side gives rise to a potential gradient (ΔV). Figure redrawn from the work of T. Tritt.[4] (b) Schematic of a TE generator; the buildup of positive and negative charges at the base of the *p*- and *n*-type legs, respectively, allows for current flow and the generation of electrical power.

When identifying ideal candidates for TE applications, the Seebeck coefficient is not the only variable that must be considered. In fact, the efficiency of TE materials is often evaluated on the basis of the dimensionless figure of merit, *ZT*, which may be expressed as:[5]

$$ZT = \frac{S^2 \sigma T}{\kappa} \tag{1.1}$$

where σ is the electrical conductivity, T is temperature, and κ is the total thermal conductivity, i.e., the sum of the lattice (κ_l) and electronic (κ_e) thermal conductivities. Current state-of-the-art, commercially available TE materials generally exhibit a *ZT* of around unity at room temperature.[6] However, it is believed that a $ZT \geq 4$ would need to be achieved for TE devices to be competitive with mechanical power generation.[7] In addition, the cost per watt associated with current TE modules is often too high to justify their use on a large scale.[8] This last point reveals a particular advantage of utilizing TE generators in waste heat recovery applications: poor conversion efficiencies and low *ZT* values may be offset by the fact that the cost of energy input (i.e., waste

heat) is negligible. In such a scenario, a more important consideration is the power factor, defined as $S^2\sigma$.[9] It has indeed been reported that, when a free or inexpensive energy source is available, the cost per watt is primarily determined by the power per unit area (which involves optimization of the device geometry) and the operational lifetime.[10,11]

For commercial applications, the most widely used TE materials are Bi_2Te_3-based alloys, which exhibit *ZT* values close to unity at room temperature.[12] However, in addition to the relatively high cost of its component elements, Bi_2Te_3 has a rather low melting point of approximately 860 K,[13] and decomposition of the alloy at elevated temperatures can lead to the evolution of toxic tellurium fumes.[14] Furthermore, since Bi_2Te_3 is a narrow bandgap semiconductor, the possibility of minority charge carrier diffusion (which serves to reduce the magnitude of the Seebeck coefficient) at elevated temperatures must be considered.[15] Given these factors, the utilization of Bi_2Te_3-based TE generators in practical applications is generally restricted to temperatures below 550 K.

While other semiconductor alloys have been developed for use in high-temperature TE power generators (e.g., SiGe)[16], complex metal oxides are often cited as among the most promising candidates for these devices.[17] The underlying basis for such optimism lies in the inherent advantages common to many oxide systems, including: (1) good high-temperature stability, which is not only beneficial for applications such as waste heat recovery, but also allows for a large temperature gradient to be established across the material in order to increase the Carnot efficiency,[18,19] (2) an intricate structure, which leads to a reduction in the lattice thermal conductivity due to enhanced phonon scattering, and (3) the reduced cost and low toxicity of the raw component materials.

Significant progress has been made in the development of *p*-type TE oxides after large power factors (~50 μW/cm·K) were observed for single crystalline $NaCo_2O_4$.[20] Promising results have also been obtained for *p*-type polycrystalline $Na_{1.7}Co_2O_4$ (ZT = 0.8 at 955 K),[21] $Ca_{2.7}Ag_{0.3}Co_4O_9$/Ag-10 wt% (ZT = 0.5 at 1000 K),[22] and BiCuSeO (ZT = 1.4 at 923 K)[23] compounds. However, as will be discussed in Chapter 2, relatively fewer advances have been reported for *n*-type TE oxides when compared to their *p*-type counterparts.[17] At present, the most promising *n*-type TE ceramics include $Zn_{0.98}Al_{0.02}O$ (ZT = 0.65 at 1250 K)[24] and $CaMn_{0.98}Nb_{0.02}O_3$ (ZT = 0.32 at 1060 K).[25] Since thermoelectric devices require both *n*- and *p*-type materials, the overall performance of *n*-type TE oxides must be improved so that the full potential of high-temperature TE devices may be realized.

The *n*-type relaxor ferroelectric strontium barium niobate ($Sr_xBa_{1-x}Nb_2O_6$, or SBN100*x*) has been extensively studied for its pyroelectric,[26] photorefractive,[27] and electro-optic properties.[28] However, it was recently found that reduced (i.e., oxygen deficient) SBN is a promising candidate for use as an *n*-type oxide in TE generators.[29] While the structure, stability, and electrical transport behavior of this material will be detailed in subsequent chapters, it should be mentioned here that certain characteristics associated with SBN and its fabrication are advantageous for achieving enhanced TE performance. Firstly, SBN crystallizes into a complex tetragonal tungsten bronze (TTB) structure, which facilitates phonon scattering and serves to lower the thermal conductivity. The ability to dope SBN and/or vary the Sr:Ba ratio also provides great versatility in terms of tailoring the composition to optimize material properties. Furthermore, the raw component materials employed in the processing of polycrystalline SBN are quite inexpensive, a factor that can effectively lower the cost per watt if suitable power factors are generated.

Given the relatively recent interest in thermoelectric oxides, along with the aforementioned paucity of high-performance *n*-type TE ceramics, the impact that obtained findings may have on the field as a whole should be considered. Like numerous other *n*-type oxides,[30-32] an oxygen deficiency must be created in SBN to produce viable room-temperature electrical conductivity values. However, there appears to be little if any work published regarding the high-temperature stability of reduced SBN in air. As this lack of available research also exists for other oxide systems, information gleaned from a reduced SBN stability study may have broad applicability. In addition, the ferroelectric nature of SBN allows for an exploration of the possibility that polarization and/or disorder may impact the thermoelectric performance, as the existence of such effects has been alluded to in previous work.[33,34] Confirming the presence or lack of such a correlation not only adds to the body of SBN-related literature, it could also prove useful to researchers investigating the TE behavior of other uniaxial ferroelectric *n*-type oxides, such as doped $Sr_nNb_nO_{3n+2}$.[35]

1.2. Project objectives and dissertation overview

In this dissertation, suitable processing protocols for the synthesis of phase-pure SBN powders with various Sr:Ba ratios were developed. Bulk polycrystalline specimens sintered from the powders were subsequently examined via X-ray photoelectron spectroscopy (XPS) so as to elucidate the nature of local cation environments and site occupancy in the SBN lattice. SBN compositions were ultimately annealed in a reducing environment and tested for their TE properties. Using $Sr_{0.5}Ba_{0.5}Nb_2O_6$ (SBN50) as a representative stoichiometry, XPS analysis was performed on reduced samples so that a firm understanding of the defect state could be derived. Such experiments have the additional benefit of allowing correlations to be made between the

defect structure and TE performance. A comprehensive investigation of electrical conductivity and Seebeck coefficient trends was also carried out. Through the application of polaron hopping models and solid-state physics concepts, a clearer scenario of charge transport in SBN was formulated. Based on an analysis of the electrical characteristics, a strategy to increase the TE performance by establishing a suitable pore structure was implemented. Results pertaining to the high-temperature stability of reduced SBN in air are also presented.

It must be stressed that, when referring to the primary objectives of this project, the attainment of high *ZT* and/or power factor values, while quite desirable, was not the sole overarching goal. Rather, the attainment of fundamental insight regarding local chemical environments and the nature of charge transport in SBN was viewed as paramount. Such an approach was adopted on the belief that significant progress can more easily be achieved if research paths are forged based on a complete understanding of the material as a whole. To this end, the specific aims of this work may be summarized as follows:

1) Acquire firm knowledge of the structure, local chemical environments, and defect states associated with SBN in both its as-processed and reduced forms.
2) Obtain viable TE data for reduced SBN, and use the results to formulate a coherent scenario of charge transport in the material.
3) Based on the observed electrical and thermal transport behavior, formulate and implement a strategy by which the TE performance may be enhanced.

In Chapter 2 of this dissertation, fundamental concepts and theory related to thermoelectric phenomena are discussed. Previous work in the field of TE oxides is also reviewed. The properties

of SBN, including its structure and ferroelectric behavior, are outlined, and recent research into the use of reduced SBN as an *n*-type TE oxide is summarized. Experimental details regarding the processing, characterization, and TE testing of SBN specimens are provided in Chapter 3.

Structural and morphology data obtained from processed SBN specimens are presented in Chapter 4. The results of an XPS analysis to ascertain site occupancy in unreduced SBN with various Sr:Ba ratios are discussed in Chapter 5. An XPS investigation of local cation environments and Nb valence states for SBN50 reduced in different gas mixtures is also included. In Chapter 6, thermoelectric measurements acquired for SBN50 reduced at different temperatures and times are described; the TE performance of different SBN compositions is also outlined. An analysis of trends in the observed TE data at various testing temperatures is then provided, and the likely mechanisms of charge transport in the material are detailed. Results obtained by modifying the microstructure so as to exploit the advantageous characteristics of SBN are also discussed. The final section of Chapter 6 contains findings related to the high-temperature stability of reduced SBN in low-pressure or air environments.

A comprehensive summary of the research presented in this dissertation is provided in Chapter 7. Possible avenues for future work based on the results contained herein are also proposed.

Chapter 2. Theory and Background

2.1. Review of thermoelectric phenomena

Before reviewing some of the concepts relevant to TE power generation, the historical origins of thermoelectricity will be briefly discussed. While there have been varying reports as to the date of discovery, it appears that the first observations of TE behavior were made in 1820-21 by Thomas Johann Seebeck, as detailed in the published record of the Berlin Academy of Sciences.[36,37] An illustration of the type of experiment conducted by Seebeck is shown in Figure 2.1.[38] Upon heating one junction of a closed loop formed by two different conductors, deflections in a magnetic needle were noted. Seebeck incorrectly attributed such a phenomenon to magnetic polarization induced by a temperature difference, i.e., thermomagnetism.[37,39] It should be pointed out that many researchers at the time were aware of (and perhaps inspired by) findings reported by Hans Christian Oersted, who in 1820 published a study showing that a magnetic needle will be deflected when near an electrical current flowing in a parallel direction.[40,41] In fact, the term "thermoelectric" is believed to have first been coined by Oersted himself when discussing Seebeck's results.[42] Regardless, the generation of a voltage by establishing a thermal gradient

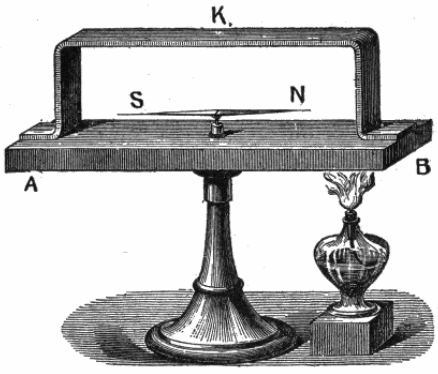

Figure 2.1. An illustration of one experiment conducted by Seebeck.[38] A bent piece of copper (K) forms a closed loop with a bismuth block at junctions A and B. Heating one junction causes deflection of a magnetic needle with poles N and S.

across a material is now eponymously known as the Seebeck effect, while the intrinsic material parameter representing the ratio of the potential gradient to the temperature difference is denoted as the Seebeck coefficient ($S = \Delta V/\Delta T$). In terms of the experiment in Figure 2.1, the heating of one junction in a circuit of two dissimilar metals leads to the formation of a current loop due to the different temperature responses of each material, i.e., their contrasting Seebeck coefficients. This current in turn produces a magnetic field and thus, deflection of a magnetic needle is observed.

The Seebeck coefficient can also be understood from a diffusion perspective using current density equations. To begin, the total electrical current density (J_{total}) can be defined as the sum of the drift current density (J_{drift}), which arises as a result of an applied electrical field (E), and the diffusion current density (J_{diff}), which is produced due to a gradient in the carrier density (n) and the associated diffusivity (D). This may be expressed as follows:[43,44]

$$J_{total} = J_{drift} + J_{diff} = \sigma E + q\left(n\frac{\Delta D}{\Delta x} + D\frac{\Delta n}{\Delta x} \right) \tag{2.1}$$

where $J_{drift} = \sigma E$ (σ is the electrical conductivity) and J_{diff} is represented by the terms in parentheses multiplied by the elementary charge (q). If it is assumed that the material in question is homogeneous (i.e., there is no significant change in the material properties with respect to position), then the only driving force for net charge carrier migration is a temperature gradient. As such, the diffusion current density can be re-written as:

$$J_{diff} = q\left(n\frac{\Delta D}{\Delta T} + D\frac{\Delta n}{\Delta T} \right)\frac{\Delta T}{\Delta x} \tag{2.2}$$

In the case of an open circuit (i.e., $J_{total} = 0$), Eq. (2.1) becomes:

$$-\sigma E = q\left(n\frac{\Delta D}{\Delta T} + D\frac{\Delta n}{\Delta T} \right)\frac{\Delta T}{\Delta x} \tag{2.3}$$

Since $S = \Delta V/\Delta T$ and $E = \Delta V/\Delta x$, it can be seen that the right-hand side of Eq. (2.3), excluding $\Delta T/\Delta x$, is equal to the negative of the Seebeck coefficient multiplied by the electrical conductivity, i.e.,

$$J_{diff} = -\sigma S \frac{\Delta T}{\Delta x} \tag{2.4}$$

A comparison of Eq. (2.4) to Fick's first law of diffusion[45] ($J = -D\Delta C/\Delta T$, where J is the diffusion flux, D is the diffusion coefficient, and C is the concentration of a species) shows that, in the presence of a thermal gradient, the diffusion coefficient is equivalent to the Seebeck coefficient "scaled" by the electrical conductivity.[43] Furthermore, the negative sign in Eq. (2.4) denotes that diffusion occurs down the gradient, from high to low temperature. In the presence of a positive thermal gradient, a negative Seebeck coefficient will yield a positive value for the diffusion current density. For the coordinate system shown in Figure 2.2(a), this means that electrons will flow down the thermal gradient, from high to low temperature, in a manner consistent with the behavior observed for *n*-type materials. Conversely, a positive Seebeck coefficient [Figure 2.2(b)] produces a negative diffusion current density, resulting in a net flux of holes down the temperature gradient. Such transport behavior is in agreement with the characteristics of *p*-type materials.

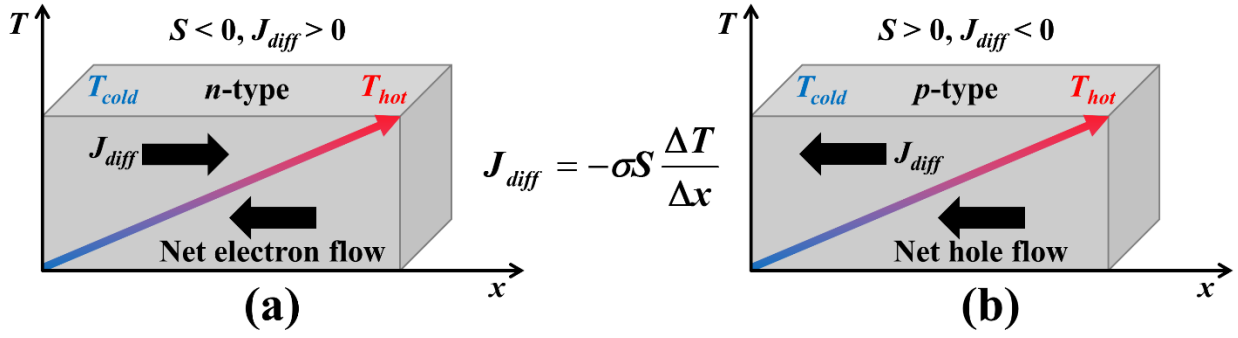

Figure 2.2. Schematic illustrations of charge flow in *n*- and *p*-type materials under a positive thermal gradient. (a) A negative Seebeck coefficient results in a positive J_{diff} and a net flow of electrons in the opposite direction, down the thermal gradient, as is consistent with an *n*-type material. (b) Positive S values produce negative diffusion current densities and a net flow of holes down the temperature gradient, in agreement with the behavior of *p*-type materials.

A little more than a decade after the initial TE findings of Seebeck, Jean Charles Peltier observed that current passing through dissimilar conductive materials produced a temperature change.[46,47] Subsequent work by Heinrich Lenz showed that heat is either generated or absorbed at a junction between conductors depending on the direction of an electrical current.[48] This TE phenomenon is now known as the Peltier effect; it can be thought of as the reverse of the Seebeck effect. In terms of formalism, the Peltier coefficient (Π) represents the constant of proportionality between the rate of heat generated or absorbed (dQ/dt) at a junction, and the current flow (I) through the junction.[49] In addition, the Seebeck and Peltier coefficients are related such that $\Pi = ST$, where T is temperature.

While the research contained herein is more focused on efficient TE power generation, the mechanisms by which TE cooling devices (or Peltier coolers) operate are nonetheless interesting. A schematic of a Peltier cooler is shown in Figure 2.3. Beginning at the left of the figure, the first junction that will be encountered by electrons traveling through the device will be that between the metal and the *p*-type semiconductor. As the valence band of the *p*-type semiconductor is at a

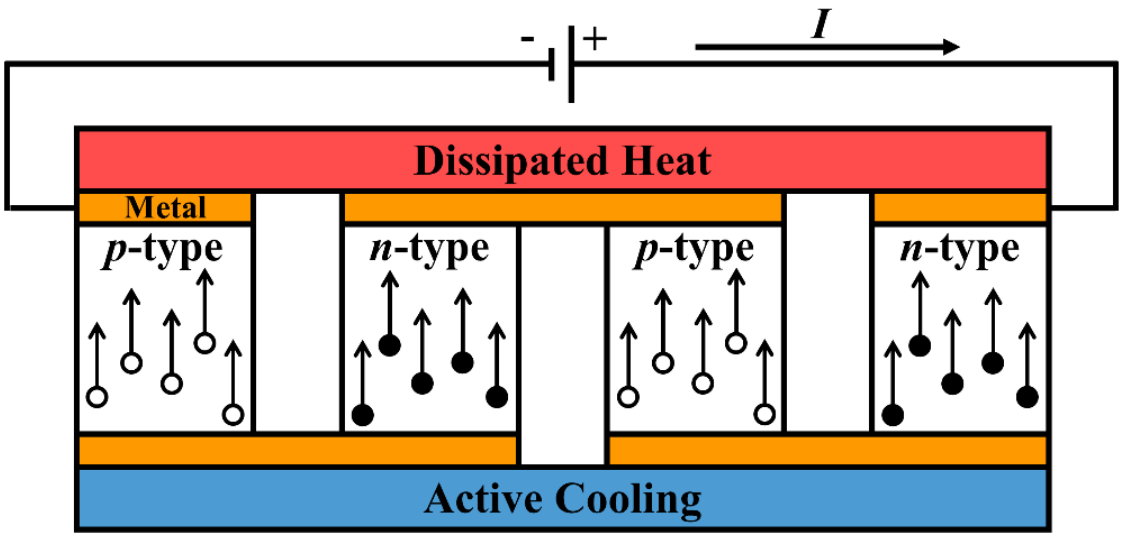

Figure 2.3. A schematic of a TE cooling device. Electrons and holes are represented by solid and open circles, respectively.

lower energy than that of the metal, energy is released in the form of heat at the metal/*p*-type junction. Next, the electron must move through *p*-type/metal and metal/*n*-type interfaces in order to enter the *n*-type semiconductor. Heat is absorbed at both of these locations, first due to the aforementioned valence band difference, and then as a result of the higher energy of the conduction band in the *n*-type material when compared to that in the metal. Lastly, heat is again evolved, this time at the *n*-type/metal junction, due to the difference in the conduction band position of the two materials. The above process occurs repeatedly and, consequently, one side of a Peltier device serves as a heat sink while the opposite side provides active cooling.

When discussing ideal materials for use in TE generators, one must first examine the parameters by which the efficient conversion of heat into electrical power can be evaluated. To begin, it should be noted that the conversion efficiency (η) of a TE generator, such as that shown in Figure 1.1(b), represents the ratio of the electrical power supplied to an external circuit to the heat adsorbed at the source (i.e., the hot junction of the generator).[50,51] Using expressions for Joule and Peltier heating, as well as accounting for the thermal conductivity (κ) of each TE generator leg, the maximum efficiency (η_{max}) obtained via differentiation can be expressed as:

$$\eta = \frac{T_h - T_c}{T_h} \cdot \frac{M - 1}{M + (T_c / T_h)} \tag{2.5}$$

where

$$M = [1 + Z(T_h + T_c)/2]^{1/2} \tag{2.6}$$

Here, T_h and T_c are the temperatures at the hot and cold junctions, respectively, and Z is expressed as follows:

$$Z = \frac{(S_p - S_n)^2}{[(\kappa_p / \sigma_p)^{1/2} + (\kappa_n / \sigma_n)^{1/2}]^2} \tag{2.7}$$

where the subscripts "*p*" and "*n*" denote properties of the *p*-type and *n*-type materials, respectively. While *Z* should technically be employed to assess pairs of TE elements (since the Seebeck and Peltier effects are exploited only when there is a coupling of dissimilar conductors), the dimensionless figure of merit (*ZT*), as defined in Eq. (1.1), is often used to evaluate the TE efficiency of individual TE materials.

It is evident from Eq. (1.1) that maximization of *ZT* requires a material with a large Seebeck coefficient, high electrical conductivity, and low thermal conductivity. However, as shown in Figure 2.4,[1] the development of such TE elements is often difficult due to the interrelationships among the relevant TE parameters. For example, the Seebeck coefficient of a heavily-doped (i.e., degenerate) *n*-type semiconductor can be expressed as:[52]

$$S = \frac{8\pi^2 k_B^2 T}{3qh^2} m^* \left(\frac{\pi}{3n}\right)^{2/3} \tag{2.8}$$

where k_B is the Boltzmann constant, h is Planck's constant, m^* is the electron effective mass, and n is the carrier concentration. Inspection of Eq. (2.8) reveals that high $|S|$ values may be obtained with an increase in the electron effective mass and a reduction in the carrier concentration, both of which serve to reduce the electrical conductivity. In addition, the electronic contribution to the thermal conductivity (κ_e) is directly proportional to the electrical conductivity at a given temperature through the Wiedemann-Franz law, expressed as $\kappa_e = L\sigma T$, where L is a constant known as the Lorenz number.[53] Consequently, an increase in σ may lead to a corresponding increase in κ, which in turn reduces *ZT*.

In order to maximize TE performance, it is helpful to examine previous research into the electrical transport behavior associated with the different material classes. Fritzsche derived the Seebeck coefficient by first writing the electrical conductivity as an integral over single electron

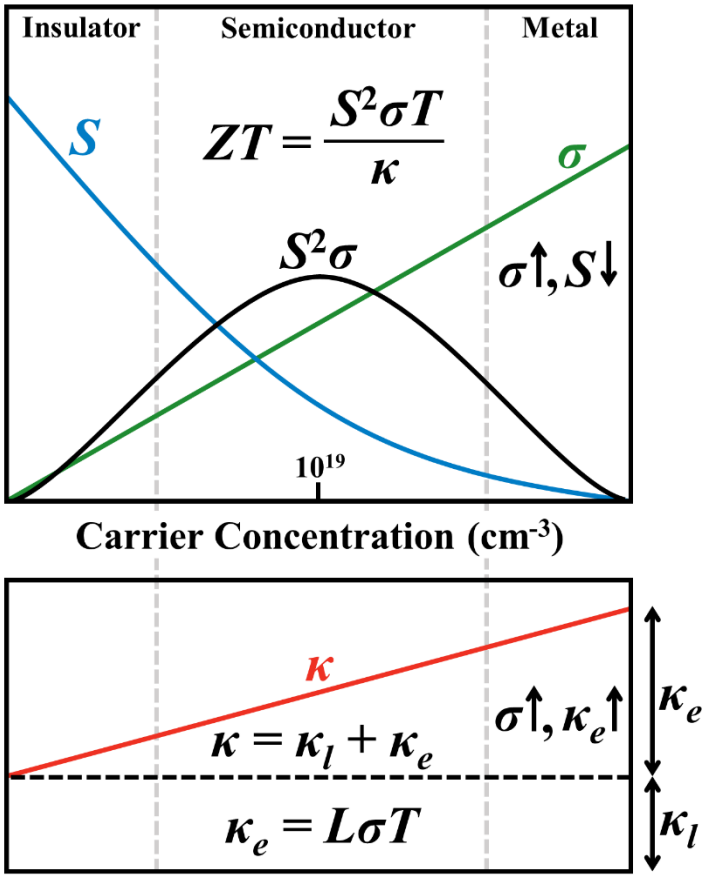

Figure 2.4. The parameters of *ZT* versus the carrier concentration; interrelationships among the factors make *ZT* optimization difficult. Figure redrawn from the work of Shakouri.[1]

states:[54]

$$\sigma = \int \sigma(E)dE = q\int g(E)\mu(E)\,f(E)[1-f(E)]dE \tag{2.9}$$

where $\sigma(E)$, $g(E)$, $\mu(E)$, and f(E) are the electrical conductivity, density of states, mobility, and Fermi function at energy E. Here, it is noted that the Peltier coefficient is representative of the energy carried by electrons, relative to the Fermi level (E_F), per unit charge; this is apparent by the definition of the Peltier coefficient, $\Pi = ST$. The contribution each electron makes to Π is scaled by its relative impact to the total conduction, which can written as $\sigma(E)dE/\sigma$. This leads to the following expressions for the Peltier and Seebeck coefficients:[54]

$$\Pi = -\frac{1}{q}\int (E - E_F)\frac{\sigma(E)}{\sigma}dE \tag{2.10}$$

$$S = -\frac{k_B}{q}\int\left(\frac{E - E_F}{k_B T}\right)\frac{\sigma(E)}{\sigma}dE \tag{2.11}$$

For metals, only charge carriers in the vicinity of the Fermi level, i.e., those with energies ~kT, contribute to electrical current. Consequently, $|S|$ values for metals tend to be quite low, in the range of 1 – 10 μV/K.[55] The high thermal conductivity of metals also limits their TE performance. On the other end of the materials spectrum, insulators have low κ and high $|S|$, but their poor electrical conductivity leads to small ZT values. Ultimately, the best thermoelectrics tend to be highly-doped (usually degenerate) semiconductors with carrier concentrations in the range of 10^{19} – 10^{21} cm^{-3}.[12,56]

Strategies to optimize ZT in highly-doped and/or degenerate semiconductors have been developed based on a form of the Mott relation derived from Eq. (2.11):[57]

$$S = \frac{\pi^2 k_B^2 T}{3q}\left(\frac{1}{n}\frac{dn(E)}{dE} + \frac{1}{\mu}\frac{d\mu(E)}{dE}\right)_{E=E_F} \tag{2.12}$$

where $n(E)$ is the carrier concentration at energy E. From Eq. (2.12), it can be seen that an increase in $|S|$ may be achieved while maintaining good electrical conductivity if the slope of the density of states with respect to energy, $dg(E)/dE$, at E_F is increased, but the value of $g(E)$ is itself kept finite (since $n(E) = g(E)f(E)$). Heremans *et al*. successfully applied this concept by doping PbTe with thallium so as to produce additional energy levels (called "resonant levels") at the Fermi level.[57] An approximately 100% increase in ZT, from 0.71 for $Na_{0.01}Pb_{0.99}Te$ to 1.5 for $Tl_{0.02}Pb_{0.98}Te$, was observed at 773 K after the introduction of thallium dopants. While the TE behavior of bulk structures were evaluated in this work, it should be noted that the energy dependence of the density of states can also be increased via size quantization effects.[58] In particular, when moving from

conventional bulk materials to one- or two-dimensional structures, the shape of the density of states can change from parabolic to one with rather sharp features.[59]

Inspection of Eq. (2.12) reveals another method by which enhancements in $|S|$ may be obtained: an increase in the energy dependence of the mobility, $d\mu(E)/dE$. This can be achieved via electron energy filtering, whereby electrons are preferentially scattered according to their energy. Since $\mu(E)$ is proportional to the relaxation time, $\tau(E)$, the intent is to increase $d\tau(E)/dE$ such that a corresponding rise in $d\mu(E)/dE$ will occur.[59] The energy filtering mechanism has been successfully demonstrated for $Pb_{1.06}Te$ with 30 – 40 nm-sized Pb precipitates.[60] However, one disadvantage to scattering charge carriers to increase $|S|$ is that undesirable decreases in σ may be observed. In an ideal scenario, a sizable increase in $|S|$ is attained without significant degradation in the electron mobility.

Of the individual parameters that constitute the dimensionless figure of merit, S, σ, and κ_e (the electronic contribution to the total κ) are primarily related to the electronic structure of a given material, while κ_l (the lattice thermal conductivity) is associated with the propagation of phonons.[61] Therefore, one approach to improve TE performance has been to focus on minimizing κ_l while preserving the electrical transport properties. Reductions in the lattice thermal conductivity have been responsible for increased ZT values in many different systems, including skutterudites that contain "rattling" rare earth ions,[62,63] thin film superlattices and structures with embedded nanoparticles,[64-66] nanostructured alloys with a large grain boundary area,[16] and bulk nanocomposites composed of micro-sized and nanoscale constituents.[67]

In the field of TE oxides, reducing the lattice thermal conductivity is especially important given the sizable contribution of phonons to the total thermal conductivity. Furthermore, as the atomic mass ratio of metal cations to oxygen approaches unity, the thermal conductivity generally

increases due to the strong bonding characteristics of light atoms.[12,68] Many of the oxides that exhibit low thermal conductivities contain heavier elements, crystallize into a complex structure, or have favorable porosity profiles. Such topics will be addressed in the next section of this review, where the field of TE oxides is discussed in more detail.

2.2. Summary of thermoelectric oxide research

In order to obtain *ZT* values that are sufficient to justify the widespread adoption of TE technology, materials that exhibit rather unique characteristics are required. G. A. Slack proposed that an ideal TE material should behave as a phonon-glass and electron-crystal (PGEC).[69] Such a notion comes from the fact that crystalline semiconductors typically display a good combination of $|S|$ and σ, while very low κ values are measured for glasses.[70] One breakthrough in realizing the PGEC concept, and a suitable starting point for a discussion of TE oxides, was achieved through the discovery of high power factors in layered cobaltites, which are among the best *p*-type TE oxides currently studied.

In the late 1990s, Terasaki *et al*. were examining bronze-type oxide structures as a reference for high-temperature superconductors when they discovered large room temperature $|S|$ values (100 μV/K) in single crystalline Na_xCoO_2, a layered transition metal oxide.[20] These findings were surprising given that the material also exhibited a high electrical conductivity of 5000 $\Omega^{-1}\cdot cm^{-1}$, resulting in a room temperature power factor of 50 μW/cm·K. Eventually, *ZT* values of 1.2 and 0.8 were obtained for single crystal and polycrystalline Na_xCoO_2 specimens, respectively.[21,71] Such high dimensionless figure of merits have been attributed to a few factors. Firstly, the layered configuration of atoms in Na_xCoO_2 can be viewed as a sort of manifestation of the PGEC concept, where distinct "nanoblocks" perform different functions.[3] As shown in Figure 2.5, the Na_xCoO_2

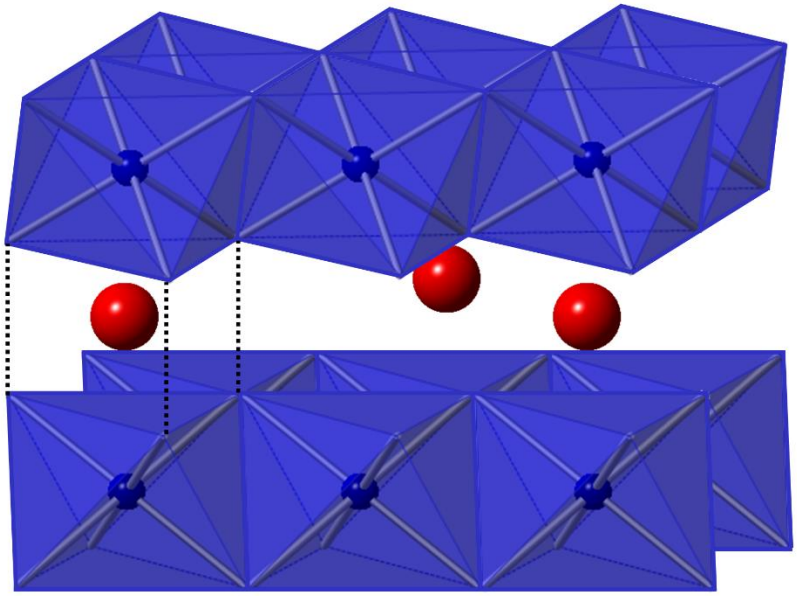

Figure 2.5. An illustration of the Na_xCoO_2 crystal structure; pathways for electrical conduction are provided by CoO_2 layers (blue octahedra), while disordered planes of Na atoms (red) serve to scatter phonons. Figure redrawn from research by Li *et al*.[72]

structure consists of CdI_2-type CoO_2 planes (shown as blue octahedra) separated by disordered layers of Na atoms (shown in red).[72] A pathway for electrical conduction is provided by the edge-sharing octahedra in the CoO_2 substructure, while phonons are effectively scattered by the random distribution of vacancies in Na planes.[73] Furthermore, the sizable power factors observed for Na_xCoO_2 may be related to contributions from spin and orbital entropy.[74,75] In particular, it has been proposed that the degeneracies of electron states associated with Co^{3+} and Co^{4+} ions serve to enhance $|S|$ and thus, increase the power factor.[76,77]

The findings reported for Na_xCoO_2 are often cited as being responsible for a significant increase in TE oxide research. Indeed, the results of a topical search for "thermoelectric oxide" in the Web of Science database (see Figure 2.6) reveal a noticeable increase in the number of peer-reviewed articles published since the late 1990s.[78] In addition, various layered cobalt oxide-based compositions are still among the best *p*-type TE ceramics currently available. For polycrystalline structures, doped *p*-type $Ca_3Co_4O_9$ exhibits improved TE performance with an increase in

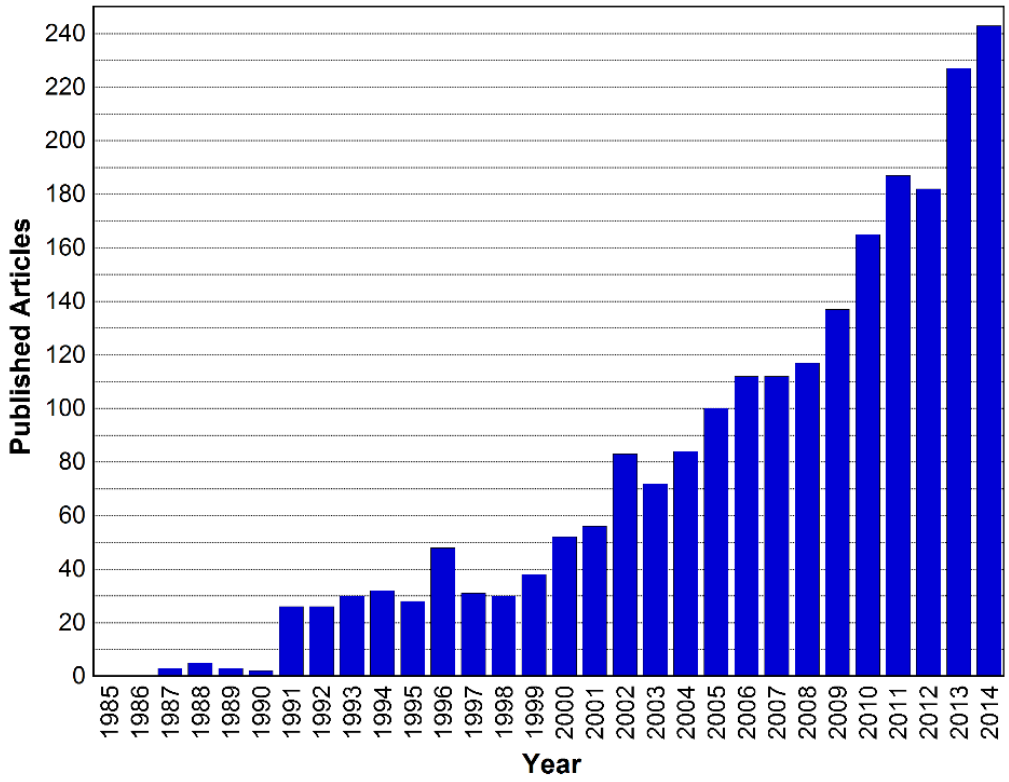

Figure 2.6. Bar chart showing the yearly total of peer-reviewed articles according to a topical search for "thermoelectric oxides".[78]

temperature, as *ZT* values of 0.3 and 0.36 have been obtained at 1000 and 1073 K, respectively.[79,80] As of this writing, textured *p*-type $Bi_{0.875}Ba_{0.125}CuSeO$ has displayed the largest *ZT* value of any polycrystalline TE oxide, with a recorded value of 1.4 at 923 K.[23] While not a member of the layered cobaltite family, BiCuSeO does crystallize into a layered structure composed of conductive $(Cu_2Se_2)^{2-}$ and insulating $(Bi_2O_2)^{2+}$ planes.

Although promising advances have been made in the area of *p*-type TE oxides, relatively fewer breakthroughs (in terms of peak *ZT*) have been achieved in the development of suitable *n*-type TE ceramics. One of the significant barriers limiting the overall performance of *n*-type TE oxides is their higher thermal conductivity. This issue is particularly evident when examining some of the more well-known *n*-type systems that have produced encouraging results. For example, the perovskite compound $SrTiO_3$ has been widely investigated for its TE properties, partly due to the

ease with which its electrical properties can be tuned through the use of various dopants. Upon the substitution of La^{3+} ions at Sr^{2+} sites in the $SrTiO_3$ lattice, a large room temperature power factor of 36 μW/cm·K^2 (comparable to that of Bi_2Te_3) was reported.[81,82] Such an unusually high power factor has been attributed to the triply degenerate Ti 3*d*-t_{2g} orbitals (a consequence of crystal field splitting), which make a sizable contribution to the density of states effective mass and thus, increase the value of |*S*|.[50,83] However, the room temperature *ZT* of the same La-doped $SrTiO_3$ specimen was only 0.09 due to a large measured thermal conductivity of ~11 W/m·K, approximately 95% of which was ascribed to phonons (i.e., κ_l). The high degree of symmetry and strong bonding of light atoms in the perovskite structure are considered to be responsible for the elevated κ_l values in $SrTiO_3$. While the doping of $SrTiO_3$ with other rare earth metals (e.g., Y, Sm, Gd) was found to reduce the room temperature thermal conductivity to ~3.6 – 5.8 W/m·K, a concurrent decrease in the power factor served to reduce *ZT*.[84] Furthermore, similar peak *ZT* values of ~0.35 were calculated at 1000 K for epitaxial films, polycrystalline films (200 nm grain size), and bulk polycrystalline specimens (20 μm grain size) of Nb-doped $SrTiO_3$, indicating that κ was not significantly affected by grain boundary scattering at elevated temperatures.[85]

The wide bandgap semiconductors ZnO and In_2O_3 have also been investigated for their potentiality as *n*-type TE oxides. At carrier concentrations as high as 10^{21} cm^{-3}, the electron mobility in these materials can reach 10 – 40 cm^2/V·s,[86] which could serve to increase the power factor. However, sizable thermal conductivity values still limit the overall performance of these transparent conducting oxides. For In_2O_3, the introduction of Ge led to an order of magnitude increase in the electrical conductivity, from ~40 Ω·m (In_2O_3) to approximately 400 Ω·m ($In_{1.8}Ge_{0.2}O_3$) at 1000 K, while |*S*| was found to decrease from 225 μV/K (In_2O_3) to 110 uV/K ($In_{1.8}Ge_{0.2}O_3$) at the same temperature.[87] Consequently, a more than two-fold increase in the power

factor was observed with the addition of Ge. Moreover, the precipitation of fine $In_2Ge_2O_7$ particles was found to occur in the parent material, leading to a decrease in κ from ~10 (In_2O_3) to ~3.5 W/m·K ($In_{1.8}Ge_{0.2}O_3$) and approximately 2.8 (In_2O_3) to ~1.7 W/m·K ($In_{1.8}Ge_{0.2}O_3$) at room temperature and 1273 K, respectively. Ultimately, a *ZT* of 0.45 was measured at 1273 K for the $In_{1.8}Ge_{0.2}O_3$ sample.

Suitable dopants such as Ga and Al have commonly been employed to enhance the electrical properties of ZnO, and hall mobilities of up to 80 $cm^2/V{\cdot}s$ have been measured for polycrystalline Al-doped ZnO samples.[68] However, the rather light component elements and strong bonding in the wurtzite structure of ZnO contribute to a high sound velocity.[88] This in turn leads to undesirably large lattice thermal conductivities according to the following expression:

$$\kappa_l = \frac{1}{3} C_v v l \tag{2.13}$$

where C_v is the lattice heat capacity, v is the velocity of sound in the material, and l is the phonon mean free path.[58] As such, total thermal conductivities of up to 40 W/m·K at room temperature and 5 W/m·K at 1000 K have been measured for polycrystalline Al-doped ZnO specimens.[68] While reductions in κ due to grain boundary scattering were observed in fine-grained bulk ZnO (from 15 W/m·K for a 20 μm grain size to 7 and 3.5 W/m·K for 200 and 30 nm grain sizes, respectively, at 500 K), the smaller electron mobility and more significant decrease in σ for these samples actually served to lower *ZT* further.[89] Proper co-doping of ZnO with both Al and Ga has proven to be a far more effective approach to improving the TE performance. One of the highest *ZT* values to date for any *n*-type TE oxide was obtained by Ohtaki *et al*. for bulk polycrystalline $Zn_{0.96}Al_{0.2}Ga_{0.2}O$.[90] The introduction of Ga atoms into Al-doped ZnO led to the formation of a secondary Ga-containing phase. While a slight reduction in the electrical conductivity was noted after Ga incorporation, $|S|$ increased significantly (150 μV/K for $Zn_{0.98}Al_{0.2}O$ to 250 μV/K for

$Zn_{0.96}Al_{0.2}Ga_{0.2}O$ at 1247 K) and lower κ values (7.5 W/m·K for $Zn_{0.98}Al_{0.2}O$ and 5 W/m·K for $Zn_{0.96}Al_{0.2}Ga_{0.2}O$) were measured. Consequently, a *ZT* of 0.65 at 1247 K was reported for bulk $Zn_{0.96}Al_{0.2}Ga_{0.2}O$.

The variety of synthesis techniques available for the processing of bulk oxides provides a certain degree of flexibility in terms of tailoring the microstructure so as to enhance the TE behavior. For example, the thermal conductivity of TE oxides could be lowered substantially by establishing favorable porosity levels, as air has a very low κ of approximately 0.026 W/m·K.[91] Furthermore, it is possible that pores could act to increase the energy dependence of the relaxation time ($d\tau(E)/dE$), thereby increasing $|S|$ via electron energy filtering. Of course, a subsequent improvement in *ZT* would require that a sufficient conduction path exists for charge carriers so that sizable decreases in σ are avoided. The efficacy of the above strategy was demonstrated in a study by Ohtaki *et al.*, where 150 nm-sized polymethylmethacrylate (PMMA) powder was employed as a sintering additive to produce nanovoids in sintered $Zn_{0.98}Al_{0.02}O$ specimens.[24] At a 10 wt% concentration of PMMA, the magnitude of $|S|$ increased by almost 100 μV/K at 1250 K, while no significant change in σ was observed. In addition, κ was reduced by approximately 16% at the same temperature, leading to a *ZT* value of 0.65. The details of our work regarding the use of PMMA to form porous SBN ceramics will be detailed in Chapter 6.

One disadvantage of certain *n*-type TE oxide systems, particularly reduced niobates and titanates, is their tendency to oxidize in air at elevated temperatures. This in turn can cause sizable decreases in the electrical conductivity, to the point where the material may become practically insulating. Such poor thermal stability in reduced *n*-type ceramics, especially when compared to their *p*-type counterparts, can be understood by examining the nature of charge carrier generation

in the two classes of materials. For *p*-type ceramics, excess holes may be generated via an uptake of oxygen as follows:

$$\frac{1}{2}\mathrm{O}_2 \rightarrow V_{\mathrm{M}}'' + 2h^{\bullet\bullet} + \mathrm{O}_{\mathrm{O}}^{x} \tag{2.14}$$

Here, oxidation of the *p*-type ceramic induces the formation of metal vacancies (V_{M}''), which are in turn compensated by positively-charged holes so as to maintain electroneutrality. (Note: Kröger-Vink notation is used here, where prime symbols represent a negative charge with respect to the lattice, *x* indicates no net charge, and dots denote positive charges.)[92] For the *p*-type TE oxide $Ca_3Co_4O_9$, average valences of 3.23+ and 3.5+ have been given for the Co ion, resulting in an oxygen-rich compound.[93,94] Moreover, an increase is σ upon heating in air has been noted for $Ca_3Co_4O_9$, even at temperatures of up to 1000 K.[95]

In contrast to many *p*-type materials, it is a deficiency of oxygen in the lattice that induces the generation of free electrons in reduced *n*-type oxides; this reaction may be represented as follows:

$$\mathrm{O}_{\mathrm{O}}^{x} \rightarrow V_{\mathrm{O}}^{\bullet\bullet} + 2e' + \frac{1}{2}\mathrm{O}_2(g) \tag{2.15}$$

For this reaction, oxygen evolved from the lattice donates electrons back to the material to compensate for positively charged oxygen vacancies ($V_{\mathrm{O}}^{\bullet\bullet}$). For titanates and niobates, these electrons are donated back to transition metal cations, leading to a decrease in valence and a corresponding rise in the electrical conductivity. A typical processing protocol to promote the reaction in Eq. (2.15) is to anneal *n*-type oxides in a suitable reducing gas mixture, followed by quenching to preserve the defective, but highly conductive state. Unfortunately, this treatment produces a thermodynamically unstable defect state that is prone to oxidation. Therefore, an

analysis of thermal stability should be conducted in oxide systems where σ is increased via reduction procedures.

As mentioned previously, oxides with a complex structure are advantageous for reducing the thermal conductivity via phonon scattering. One class of materials with an intricate, disordered structure is the so-called relaxor ferroelectrics. Unlike conventional ferroelectrics, relaxors exhibit a broad, frequency-dependent transition from a polarized (ferroelectric) to non-polarized (paraelectric) state as the temperature is raised.[96] Furthermore, polarized nanoregions (PNRs) are present in relaxors up to what is known as the Burns temperature (T_B), at which point the PNRs are effectively eliminated and the material becomes fully paraelectric.[97] Such nanoscale phase inhomogeneities not only impart unique attributes, but also allow for investigations into the influence of polarization and disorder on other material properties. With this in mind, the structure and characteristic behavior of $Sr_xBa_{1-x}Nb_2O_6$ (SBN), a relaxor ferroelectric that has only recently been explored as a TE oxide, will now be discussed.

2.3. SBN: Properties and thermoelectric behavior

The complex and disordered configuration of atoms in crystallized SBN is responsible for many of the material's interesting characteristics. SBN exhibits a tetragonal tungsten bronze (TTB) structure with the unit cell $(A1)_2(A2)_4(C)_4(B1)_2(B2)_8O_{30}$.[98,99] An illustration of the SBN crystal structure is given in Figure 2.7. The Nb^{5+} cations fully occupy B1 and B2 sites, resulting in two distinct types of NbO_6 octahedra that are aligned only along the *c*-axis. These NbO_6 octahedra are arranged in such a way so as to produce a unit cell with three different interstitial sites. The 12-fold coordinated tetragonal A1 sites (Figure 2.7, top right) are occupied solely by Sr^{2+} cations, while the larger 15-fold coordinated pentagonal A2 sites are populated by both Sr^{2+} and Ba^{2+}

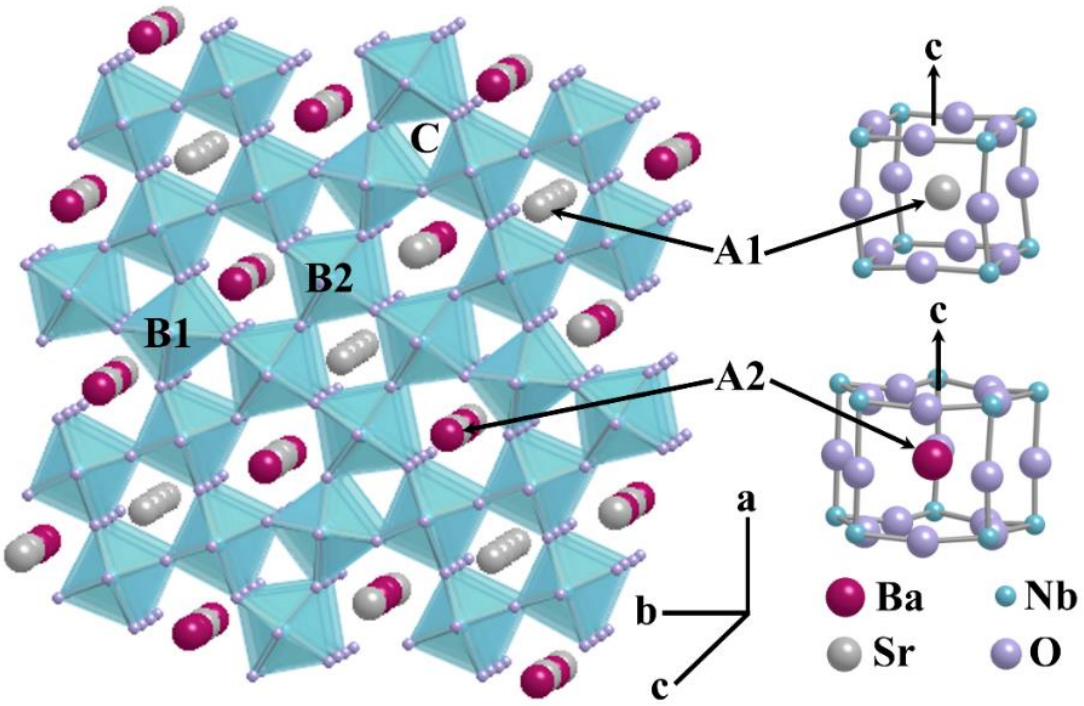

Figure 2.7. Schematic of the SBN crystal structure with detailed views of the 12-fold coordinated tetragonal A1 (top right) and 15-fold coordinated pentagonal A2 (bottom right) sites.

(Figure 2.7, bottom right). The trigonal C sites, which are too small to accommodate Sr or Ba, are vacant in the structure, as are one-sixth of the total number of A1 and A2 sites.[100] Such disorder leads to enhanced phonon scattering and thus, thermal conductivities as low as 0.8 W/m·K have been reported for SBN single crystals.[101] While the region of single-phase stability in the SBN system is often given as $0.25 \leq x \leq 0.75$ (with the congruent composition being $Sr_{0.61}Ba_{0.39}Nb_2O_6$, or SBN61), the compositional limits may vary depending on the processing conditions.[102]

In the polarized state, all three cationic elements in SBN are displaced from oxygen planes in the same sense.[103] As the temperature is raised towards T_B, a maximum in the dielectric constant (ε_r) is observed; this temperature is commonly denoted as T_m. Over a composition range of $0.25 \leq x \leq 0.75$, T_m may vary from 325 (x = 0.75) to 470 K (x = 0.25), although this range does change depending on the study.[104] A plot of the dielectric constant (at a frequency of 100 Hz) with respect to temperature for a sintered SBN50 pellet is shown in Figure 2.8; the T_m of ~408 K is comparable

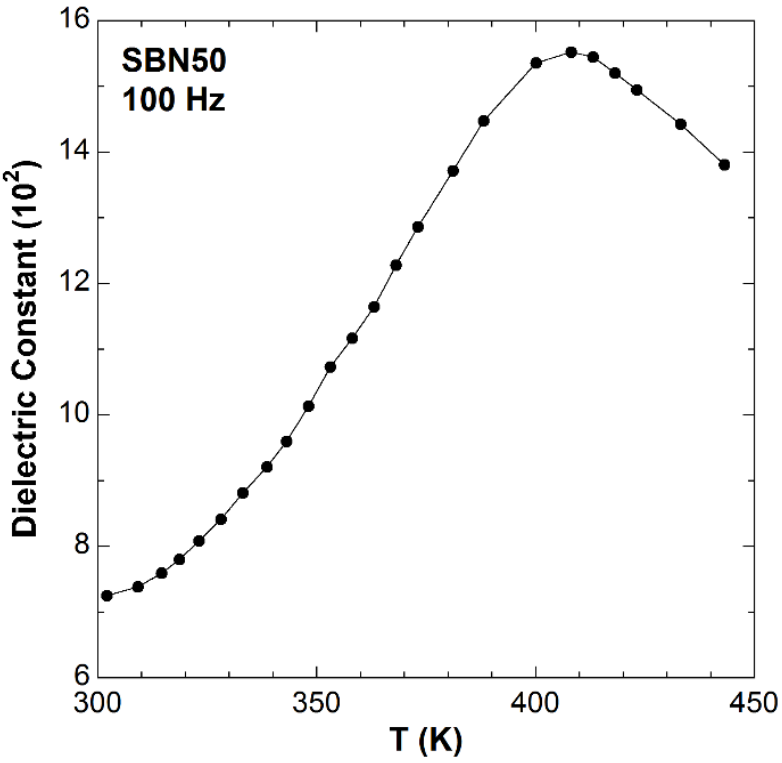

Figure 2.8. A plot of the dielectric constant with respect to temperature for a sintered SBN50 pellet; the data were acquired at a frequency of 100 Hz.

to that obtained in other studies on SBN50.[105,106] In contrast to conventional ferroelectrics (where the peak in ε_r is denoted as the Curie temperature, T_C), cooling below T_m does not result in a phase transition characterized by long-range ferroelectric order and homogenous polarization within macroscopic domains.[107] Rather, polarization exists on the nanoscale in what are known as polarized nanoregions (PNRs), and it is only after heating a relaxor ferroelectric above T_B that thePNRs are eliminated and the material becomes non-polar. In a non-polarized state, Sr, Ba, and 20% of the Nb cations move into alignment with oxygen planes, while the remaining 80% of the Nb cations are equally displaced below or above oxygen planes.[103,108] For SBN, the Burns temperature has been given as ~350 °C (~623 K).[96] It should be noted that gradual changes in the polarization behavior occur for SBN as the Sr:Ba ratio is varied, with Sr-rich compounds exhibiting more relaxor-type characteristics and Ba-rich compositions (x = 0.25 – 0.4) displaying

properties similar to those of a conventional ferroelectric (i.e., polarization with long-range order and an abrupt phase transition at T_C that does not change with frequency).[109,110]

Prior to recent TE investigations, the majority of research on SBN was conducted on samples with low electrical conductivity so as to examine electro-optic and dielectric behavior. Indeed, some of the largest linear electro-optic coefficients have been measured for SBN75 due to the lack of inversion symmetry in the SBN unit cell.[28] However, Lee *et al*. recently reported a high power factor of 40 μW/cm·K (at 550 K) parallel to the polar *c*-axis for reduced single crystalline samples of SBN61, suggesting that the ferroelectric nature of the oxide may have a significant impact on the TE properties.[29] In addition to spurring research into the TE behavior of reduced polycrystalline SBN, such results have served as motivation to study both the fundamental defect structure and underlying conduction mechanisms associated with the material.

Little work has been reported on the nature of local electronic and chemical environments in highly reduced SBN. The electrical conductivity of SBN is enhanced upon annealing the material in a suitable reducing environment so as to induce the reaction shown in Eq. (2.15). Specifically, oxygen evolved from the SBN lattice donates electrons back to the material to compensate for positively charged oxygen vacancies and preserve electroneutrality. These electrons are presumably donated back to Nb cations, leading to a decrease in the average Nb valence and a rise in the electrical conductivity. The overall reaction may be expressed as:[34]

$$\mathrm{Sr}_x\mathrm{Ba}_{1-x}\mathrm{Nb}_2\mathrm{O}_6 \rightarrow \mathrm{Sr}_x\mathrm{Ba}_{1-x}\mathrm{Nb}^{5+}_{2-y}\mathrm{Nb}^{n+}_{y}\mathrm{O}_{6-\delta} + \frac{\delta}{2}\mathrm{O}_2 \tag{2.16}$$

Before discussing previous findings related to the mechanisms of electrical conduction in SBN, the topic of charge localization in an ionic crystal must be addressed. In many transition (and rare-earth) metal oxides,[111-113] the presence of localized charge carriers leads to polarization of the lattice due to strong electron-phonon interactions. Here, the electron and its associated lattice

distortion (sometimes referred to as a "phonon cloud") can be viewed as quasiparticle known as a polaron.[114] When the radius of this quasiparticle is smaller than a unit cell dimension, the electron mobility becomes strongly tied to the lattice in what is referred to as a small polaron.[115] In such cases, the electron is essentially "trapped" at a single cation site.[116] However, charge transport may proceed via successive "hopping" events between localized states. Furthermore, at a sufficiently high defect concentration (such as that in a highly reduced oxide), localized states may overlap, leading to the formation of an impurity band in the semiconductor band gap.

The existence of Nb^{4+} polarons in doped and/or reduced SBN single crystals has been reported in previous work via optical absorption measurements.[117] In particular, it was found that electrons are excited from donor states into the conduction band, at which point they eventually become trapped at Nb^{5+} sites. The end result is the formation of a stable Nb^{4+} polaron. Excitation from these Nb^{4+} polaron states was observed in the form of a broad absorption band centered at 0.72 eV for single crystalline SBN61 specimens reduced in Ar.[118] The temperature-dependent electrical conductivity behavior of reduced SBN has also been studied in relation to polaron hopping mechanisms. At low temperatures, the thermal energy available for electron hopping is reduced and the spatial separation between energetically favorable hop sites increases. Consequently, electrons may exhibit a tendency to hop to a more distant site with a lower energy requirement rather than to a closer site with a larger potential barrier.[119] Such behavior, described by Mott, is known as variable range hopping (VRH); it may be modeled with the following expression:[120]

$$\sigma = \sigma_0 \exp[-(T_0 / T)]^{1/(d+1)} \tag{2.17}$$

where σ_0 is a pre-exponential term, T_0 is the characteristic temperature coefficient (a function of both the localization length and the density of states at the Fermi level), and d is the dimensionality

of hopping. Electrical conductivity via the VRH mechanism has been reported below ~250 K (approximately -20 °C) in polycrystalline SBN61 reduced at 1573 K for 30 h at an oxygen partial pressure (pO_2) of ~10^{-14} atm.[29]

Extensive theoretical research carried out by Holstein in the late 1950s showed that polaron hopping behavior may be divided into two distinct temperature regimes.[121,122] Below approximately $0.5\Theta_D$, where Θ_D is the Debye temperature, polaron band conductivity dominates. However, the widths of these bands are the product of an electron overlap integral and a vibrational overlap integral, the latter of which decreases exponentially with a rise in temperature. As a result, the polaron bandwidth (and thus, the electron mobility) decreases at higher temperatures to a point where, at approximately $0.5\Theta_D$, the Bloch-type band picture breaks down.[123] It is at this point, Holstein states, that polaron hopping becomes a diffusion process characterized by random hops to nearest-neighbor sites.[121] Consequently, charge mobility above $0.5\Theta_D$ exhibits an exponential increase at successively higher temperatures. For SBN, Θ_D has been calculated as ~468 K.[103,121]

While Mott's VRH expression has often been employed to model electron transport below $0.5\Theta_D$ (especially in disordered systems), electrical conductivity by nearest-neighbor small polaron hopping at higher temperatures is typically modeled with the general expression:[124]

$$\sigma = \frac{A}{T^s}\exp\left(\frac{-E_a}{k_B T}\right) \tag{2.18}$$

where A is a pre-exponential factor, s = 1 or 3/2 in the adiabatic or non-adiabatic regimes, respectively (this will be discussed in Section 6.4), and E_a is the activation energy for hopping. Small polaron hopping has been observed for reduced polycrystalline SBN61 specimens above 350 K (~80 °C).[125]

Single crystalline samples with the congruent $Sr_{0.61}Ba_{0.39}Nb_2O_6$ (SBN61) composition have been widely utilized in many previous SBN studies. This is understandable, as single crystals are quite useful when studying certain fundamental phenomena, such as the effect of structural anisotropy on phonon/electron transport. Furthermore, the additional variable of grain boundaries can be eliminated so that a more direct correlation between crystal structure and observed behavior can be made. However, due to the high cost and intense labor associated with the single crystal fabrication process, randomly-oriented or textured polycrystalline samples are much more practical for use in real-world applications. Given the broad range of stable SBN compositions, a suitable method to synthesize phase pure polycrystalline specimens with a homogeneous stoichiometry must be employed. Many different approaches have been utilized to fabricate SBN powders, including solid-state processing,[126-128] sol-gel-based synthesis,[129-131] and aqueous organic gel routes.[132-134] However, these techniques have a few disadvantages. For example, in solid-state procedures, the cation sources are combined in solid form prior to the application of a specific heat treatment to form the SBN structure. As a result, sufficient intermixing of the cations is not ensured and secondary phases may form. In addition, solid-state routes typically involve long calcination times and repeated grinding steps, which may hinder efficiency. With regards to wet chemical methods of fabricating SBN, many techniques are quite complex and involve refluxing or aging steps, procedures that are not compatible with mass production. In recent years, solution combustion synthesis (SCS) has attracted a great deal of interest as a simple, low-cost strategy to synthesize phase-pure, ultrafine ceramic powders.[135-137] In the SCS process, the desired material is formed via an exothermic redox reaction that is initiated between metal salts and a suitable fuel in a homogeneous solution. The use of aqueous precursors ensures intermixing of the cations on the atomic level, resulting in excellent phase purity. Furthermore, the rapid nature of the

combustion reaction and the high temperatures reached upon ignition allow for the formation of ultrafine (<100 nm) particles with enhanced sinterability. Such advantages, when combined with the inherent simplicity of the process, make the SCS method highly amenable to mass production.

For this study, sol-gel and SCS methods were devised to fabricate SBN powders. While both techniques yielded satisfactory results, the SCS route was adopted due to its inherent simplicity and speed. In the following section, details regarding the SCS procedure employed in this work are given, and various characterization and testing protocols are described. Information related to the sol-gel method devised over the course of this research is provided in Appendix A.

Chapter 3. Experimental Procedures

3.1. Sample fabrication and reduction

As mentioned in Chapter 2, the solution combustion synthesis (SCS) technique was employed to fabricate powder SBN samples; a diagram of the specific SCS process devised in this work is shown in Figure 3.1.[138] The method is similar to that employed in previous research.[139,140] However, in contrast to earlier studies, water was employed as the solvent for all precursor solutions. Different compositions may be synthesized by simply changing the volumetric ratio of the component solutions in the combustion mixture. Aqueous 0.25 M solutions of $Sr(NO_3)_2$ (99.0%, Alfa Aesar) and $Ba(NO_3)_2$ (99+%, Alfa Aesar) were made by dissolving the metal salts in

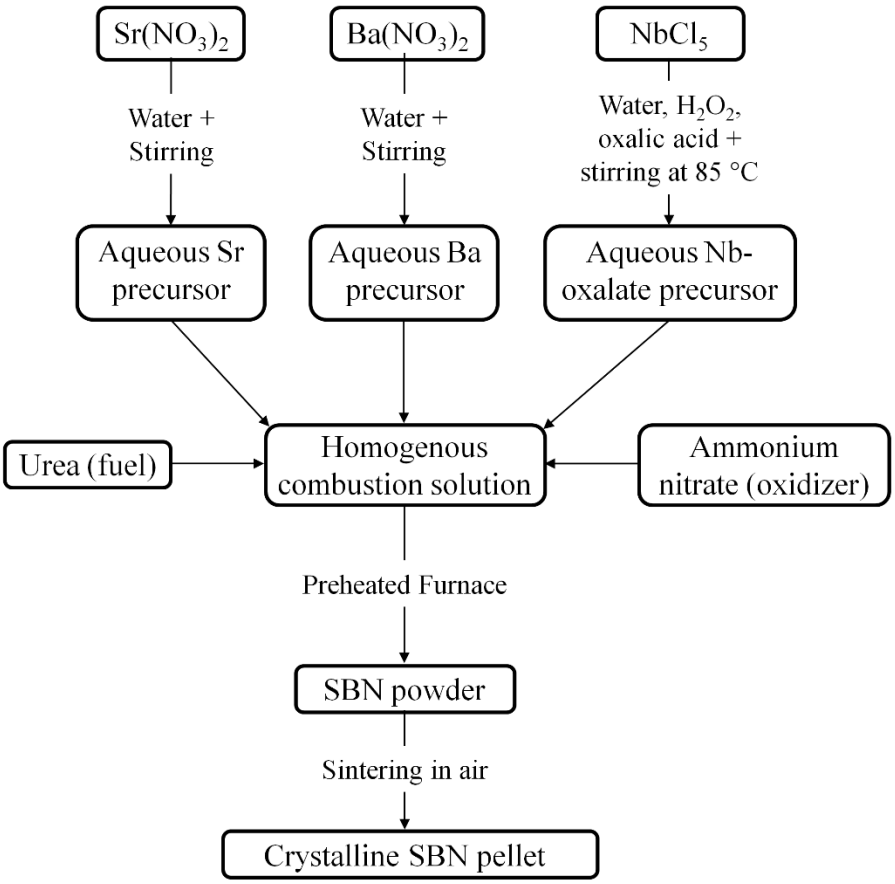

Figure 3.1. A diagram of the SCS procedure for fabricating SBN50 powder.

water under constant stirring at room temperature. To create a stable 0.25 M Nb solution, $NbCl_5$ (99%, Alfa Aesar) was first dissolved in water and H_2O_2 was added to the mixture so as to break up polymeric chains of hydrated Nb_2O_5 and ensure homogeneity.[141] Oxalic acid (≥ 99%, Sigma-Aldrich) was then added to the mixture and the precursor was heated to 85 °C for 2 h under vigorous stirring in order to form stable Nb-oxalate complexes. The pH of the Nb solution was maintained around 1 so as to ensure stability.[142] Next, the homogeneous Sr, Ba, and Nb precursors were combined in a 1:1:4 volume ratio. Urea (99.3+%, Alfa Aesar) and ammonium nitrate (NH_4NO_3, ≥ 99.0%, Sigma-Aldrich) were subsequently added to the mixture as a fuel and additional oxidizer, respectively, to yield a homogenous combustion solution. The solution was transferred to an Erlenmeyer flask and placed in a box furnace preheated to 550 °C in order to drive out excess water and initiate the desired combustion reaction. As the solution became more concentrated, flameless combustion ensued, resulting in the formation of a fluffy white powder. The combustion reaction for SBN50 powder may be written as:

$$0.5Sr(NO_3)_2 + 0.5Ba(NO_3)_2 + Nb_2(C_2O_4)_5 + 5NH_4NO_3 + \frac{5}{3}CO(NH_2)_2 \rightarrow Sr_{0.5}Ba_{0.5}Nb_2O_6 + \frac{35}{3}CO_2 + \frac{40}{3}H_2O + \frac{23}{3}N_2 \quad (3.1)$$

To fabricate sintered SBN specimens, as-processed powder was uniaxially cold-pressed in a square 20×20 mm die with no binder at a pressure of approximately 90 MPa. The green pellets were then sintered in air at 1250 °C for 4 h so as to produce polycrystalline SBN samples; the heating and cooling rates were 10 °C/min. The density (ρ) of the sintered pellets was measured by the Archimedes method, and percentages of the theoretical density (i.e., the relative density, ρ_{rel}) at each composition were calculated using lattice parameters extracted from the X-ray diffraction (XRD) patterns. Preliminary research into the use of sinter-forging to induce texture in SBN was also conducted; the results of those experiments are detailed in Appendix B.

Sintered SBN pellets were reduced in a custom-built quartz tube furnace. Upon loading the samples into the furnace, the system was purged with Ar gas for 5 min. The pellets were then reduced at temperatures of 900 – 1150 °C under a flow of N_2/H_2(5%) or Ar/H_2(5%) for various time durations; the heating rate was 30 °C/min, and the pO_2 level, as measured with a yttria-stabilized zirconia sensor (DS-Probe, Australian Oxytrol Systems), was approximately 10^{-22} atm. Strict control of the flow rate was achieved through the use of a mass flow controller (Model 1258B, MKS). To preserve the defect state induced by the reduction treatment, the furnace was simply shut off and its lid was opened after the specified time was reached. The pellets were subsequently allowed to cool to room temperature under a constant flow of forming gas.

Experiments involving the use of pore formers were also conducted. SBN50 powder synthesized according to the aforementioned SCS method was first placed in a Nalgene bottle containing water and yytria-stabilized zirconia milling media. Various weight percentages of monodispersed polymethylmethacrylate nanoparticles (PMMA, average diameter = 150 nm, Soken Chemical and Engineering Co., Ltd.) were then added and the components were mixed via ball milling for 48 h. As milling can reduce the particle size and break up large aggregates, a mixture of SBN50 and water with no PMMA was milled under the same conditions to ensure an accurate comparison of the data. Lastly, the powders were pressed, sintered, and annealed according to the procedures outlined above.

3.2. Specimen characterization

The particle size of the SBN powders was examined via transmission electron microscopy (TEM, Tecnai G2 F20, FEI) with an acceleration voltage of 200 kV. To prepare the TEM samples, the powders were dispersed in isopropanol, sonicated, and then drop-cast onto a copper grid. The

crystal structure of the fabricated specimens was verified by XRD patterns obtained with a Bruker D8 Discover instrument (Cu K_α radiation, λ = 1.5418 Å) equipped with a laser alignment system, while the morphology of the sintered pellets was analyzed by scanning electron microscopy (SEM, JSM-7000, JEOL) with an accelerating voltage of 5 – 15 kV.

A PHI 5000 VersaProbe X-ray photoelectron spectroscopy (XPS) system (Al K_α radiation, hv = 1486.6 eV) was employed to examine local cation environments and Nb valence states. Specifically, Sr, Ba, and Nb 3*d* photoemission was analyzed from both unreduced samples with different Sr:Ba ratios and reduced SBN50 pellets. Unless otherwise indicated, sintered samples were fractured prior to the photoemission spectroscopy measurements so as to obtain information characteristic of the bulk specimen and not the more highly reduced surface. All XPS spectra were acquired at a take-off angle of 45°. For a more clear presentation of the XPS results, the $3d_{3/2}$ components were removed from the Nb 3*d* and Sr 3*d* spectra using a Fourier transform deconvolution procedure.[143] This is simply a numerical manipulation of the data and requires only the spin-orbit splitting (2.72 and 1.75 eV for Nb and Sr, respectively) and spin-orbit ratio (3:2) as inputs. The raw data were employed for all component fitting.

3.3. Thermoelectric property measurements

The Seebeck coefficient and electrical conductivity of reduced SBN pellets with respect to temperature were measured with a ZEM-3 thermoelectric property measurement system (ULVAC-RIKO, Japan) in an inert, low-pressure (0.1 atm) helium gas environment via static DC and four-point probe methods, respectively. For this procedure, bar-shaped specimens with a length of ~12 mm and cross-section dimensions of 2.5 mm × 2.5 mm were first cut from the sintered pellets. The samples were then sandwiched vertically between two spring-loaded Ni electrodes covered with

carbon paper, thereby allowing a current to pass through the specimens in the lengthwise direction. Two spring-loaded Pt/Pt-Rh (R-type) thermocouples separated by a distance of 5.4 mm were placed in contact with one side of the specimens for measurements of both temperature and voltage. The testing system was equipped with a digital microscope camera so that the spacing between the thermocouples could be verified. An *I-V* plot was generated for each specimen at room temperature to ensure that the electrodes and thermocouples were in good contact with the samples. To obtain S and σ measurements with respect to temperature, the testing assembly was sealed in a quartz vacuum chamber surrounded by an infrared reflective furnace. After evacuating and purging the chamber three times with helium gas, an inert, low-pressure (0.1 atm) helium environment was established for testing. A built-in heater in one of the Ni electrodes allowed for a temperature gradient to be established across the material. The difference in voltage (ΔV) and temperature (ΔT) between the thermocouples was calculated at different furnace temperatures, and the Seebeck coefficient was obtained as the slope of the ΔV-ΔT plot. A separate apparatus was employed to acquire low-temperature electrical conductivity data in the range of 105 – 300 K. These measurements were conducted in a four-point probe configuration using a liquid nitrogen-cooled cryostat. Current was supplied with a Keithley 6220 DC current source, while voltage readings were obtained with a Keithley 2182A nanovoltmeter; electrical conductivity was calculated from least-squares fitting with Labview software.

The thermal conductivity of as-processed (unreduced) and reduced SBN pellets with respect to temperature were evaluated. A laser flash analyzer (LFA 457 MicroFlash, Netzsch) was first used to measure the thermal diffusivity (K) of the samples in an inert Ar environment. Prior to the laser flash tests, the pellets were coated with a thin layer of carbon so as to increase the absorption of energy from the laser. A high-temperature differential scanning calorimeter (DSC

404 F1 Pegasus, Netzsch) was employed to determine the specific heat (C_p) of the samples over a temperature range of 300 – 1000 K; a sapphire standard was used as a reference. For the DSC measurements, approximately 0.1 g of the sintered pellets was loaded into a Pt crucible, and scans were performed in an inert Ar environment at a rate of 5 K/min with a step size of 1 K. The total thermal conductivity of the samples was calculated according to the expression, $\kappa = KC_p\rho$. To evaluate the thermal stability of reduced SBN, as-synthesized powder was first annealed under a flow of N_2/H_2(5%) at 1000 °C for 5 h. A thermogravimetric analyzer (TGA 7, Perkin-Elmer) was then utilized to determine the weight gain due to oxidation. For the TGA scans, the powder was heated in air to 1000 °C at a rate of 10 °C/min.

Chapter 4. Structure and Morphology of SBN

4.1. Particle size and structure analysis

In order to optimize processing parameters and confirm the efficacy of the devised SCS method, structural and morphological data were first obtained. Shown in Figure 4.1 is a TEM image obtained for as-processed SBN50 powder. The particles appear to be highly agglomerated with diameters in the range of 10 – 20 nm. As stated above, ultrafine particles can be produced via SCS due to the rapid nature of the combustion reaction and the high temperatures reached in solution upon ignition. In this work, the concentration of fuel was chosen so that a stoichiometric redox mixture was established, i.e., the sum of the valences for the oxidizing and reducing components (*O* and *R*, respectively) in the mixture was such that the elemental stoichiometric coefficient, $\phi_e = O/R$, was unity.[144] This in turn ensures that maximum energy is released during the combustion reaction and ultrafine particles are produced.[145] As detailed in Appendix C,

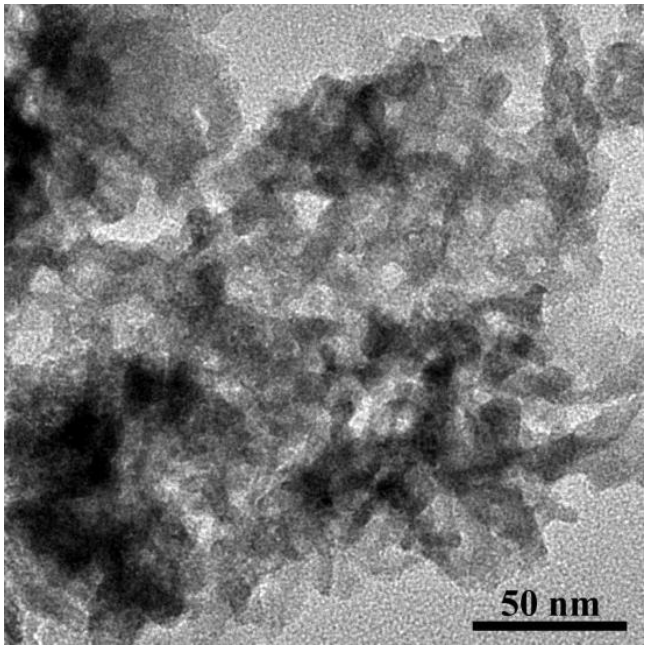

Figure 4.1. TEM image obtained for as-processed SBN50 powder.

nanosized SBN powders synthesized via SCS were also employed in the fabrication of micro-nano composite structures with bi-modal grain distributions.

Using SBN50 as a representative compound, as-synthesized powders were calcined in air from 700 – 900 °C and then analyzed to confirm phase purity; the resulting XRD patterns are displayed in Figure 4.2. Only peaks corresponding to SBN50 were observed, and reflections from secondary phases were absent from the patterns. As the calcination temperature was increased, the intensity of the SBN50 peaks also increased due to an enhancement in crystallinity. The existence of only SBN50 peaks in the XRD patterns may be attributed to the thorough intermixing of metal cations in a homogeneous solution prior to the onset of the combustion reaction.

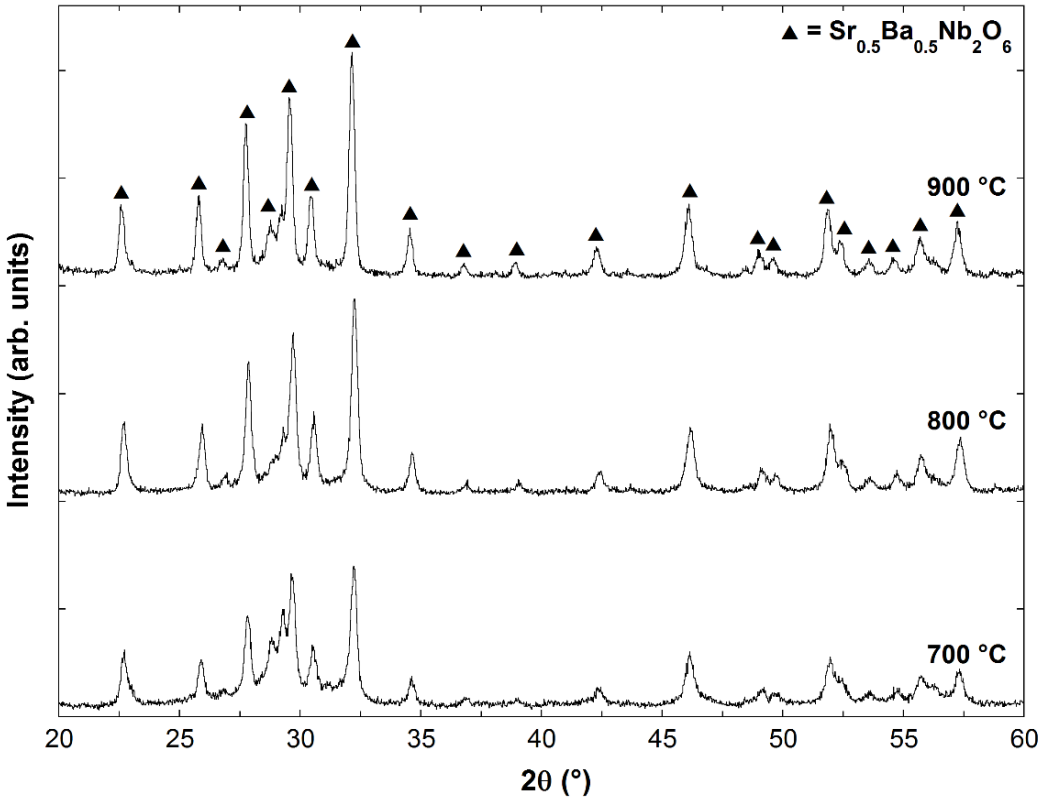

Figure 4.2. XRD patterns obtained for SBN50 powder samples after calcination at various temperatures.

With the efficacy of the SCS process confirmed, a range of SBN powders with different Sr:Ba ratios were synthesized. The XRD patterns of SBN20, 30, 50, and 61 pellets sintered at 1250 °C are shown in Figure 4.3(a); all reflections correspond to those of the tetragonal tungsten bronze SBN phase. A closer examination of the patterns [Figure 4.3(b)] shows the effect of the Sr:Ba ratio on the lattice parameters of the SBN specimens. As the value of x (i.e., the Sr content) is increased, the patterns exhibit a slight shift to higher 2θ angles. Such a trend is due to the smaller ionic size of Sr when compared Ba, as an increase in the Sr content leads to a smaller interplanar spacing and thus, a larger diffraction angle according to the Bragg relation ($n\lambda = 2d\sin\theta$, where n is an integer, λ is the wavelength of incident X-rays, d is the interplanar spacing, and θ is the diffraction angle).

The crystal structure of sintered and reduced SBN specimens was also examined. Shown in Figure 4.4(a) is the XRD pattern collected for SBN50 after reduction in Ar/H_2 for 25 h; the pattern for unreduced, single-phase SBN50 is included for comparison.[146] After annealing in Ar/H_2, peaks corresponding to the (400), (222), and (440) planes of NbO_2 appear. Furthermore, reflections from the SBN50 phase after the Ar/H_2 reduction exhibit a shift to lower 2θ angles when compared to those in the unreduced SBN50 pattern. It should be noted that grazing-incidence X-ray diffraction was not employed here and thus, the degree to which NbO_2 formation occurred in the interior of sample is unclear at this point.

The XRD data for SBN50 in its unreduced state and after annealing in N_2/H_2 for 3, 10, and 25 h are shown in Figure 4.4(b). Low-intensity peaks from the (400) and (222) planes of NbO_2 appear in the XRD pattern after 3 h. As the reduction time is extended to 10 h, the intensity of the NbO_2 (400) peak increases slightly, while the position of maximum intensity for the NbO_2 (222) reflection shifts to higher 2θ angles due to the contribution of reflections from the (111) plane of

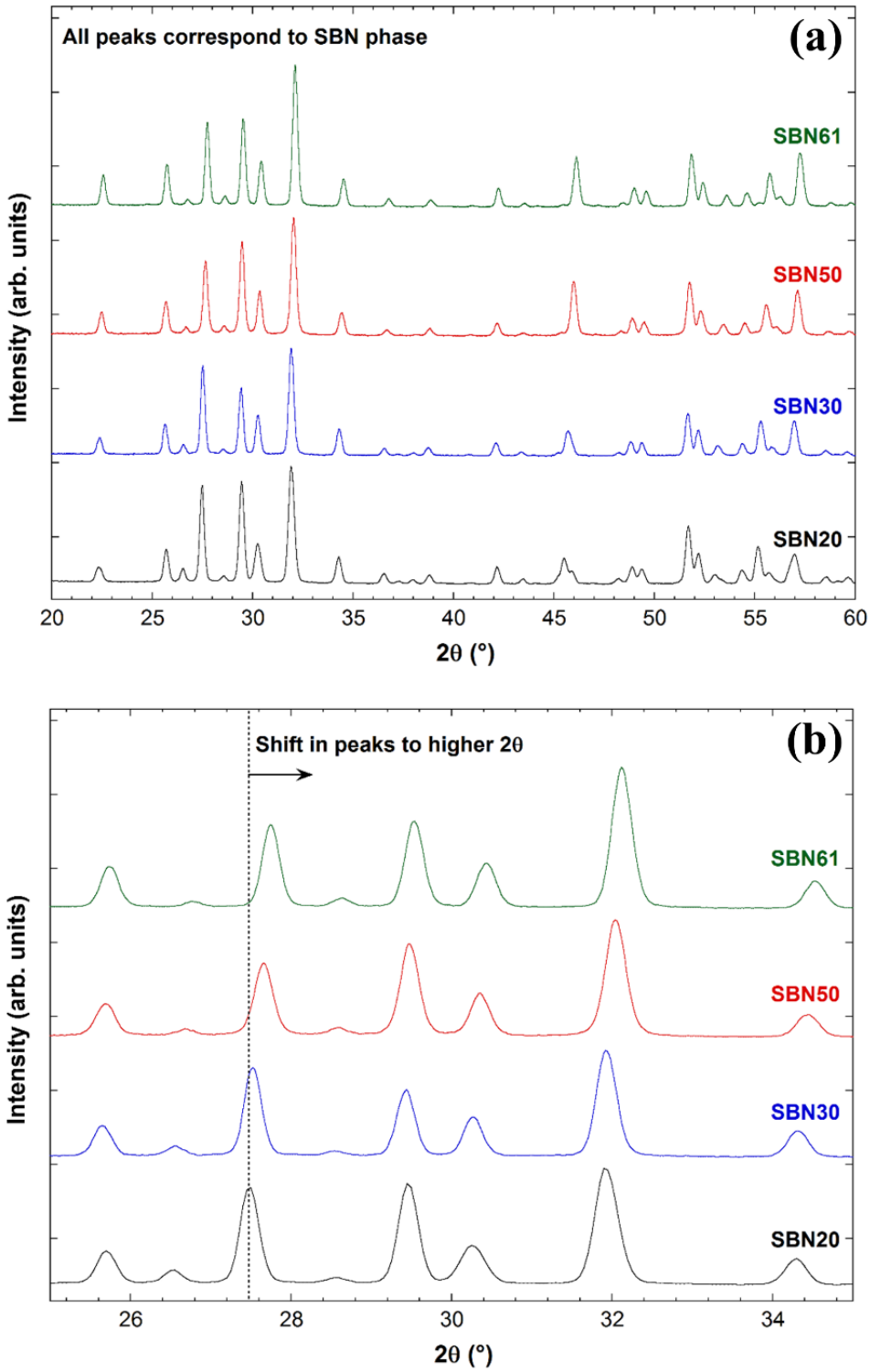

Figure 4.3. (a) XRD patterns of sintered SBN20, 30, 50, and 61 pellets; all samples were found to be single phase with the TTB structure. (b) Close-up view of the patterns in (a); an increase in Sr content leads to a reduction in the lattice parameters and a shift in the XRD peaks to higher 2θ angles.

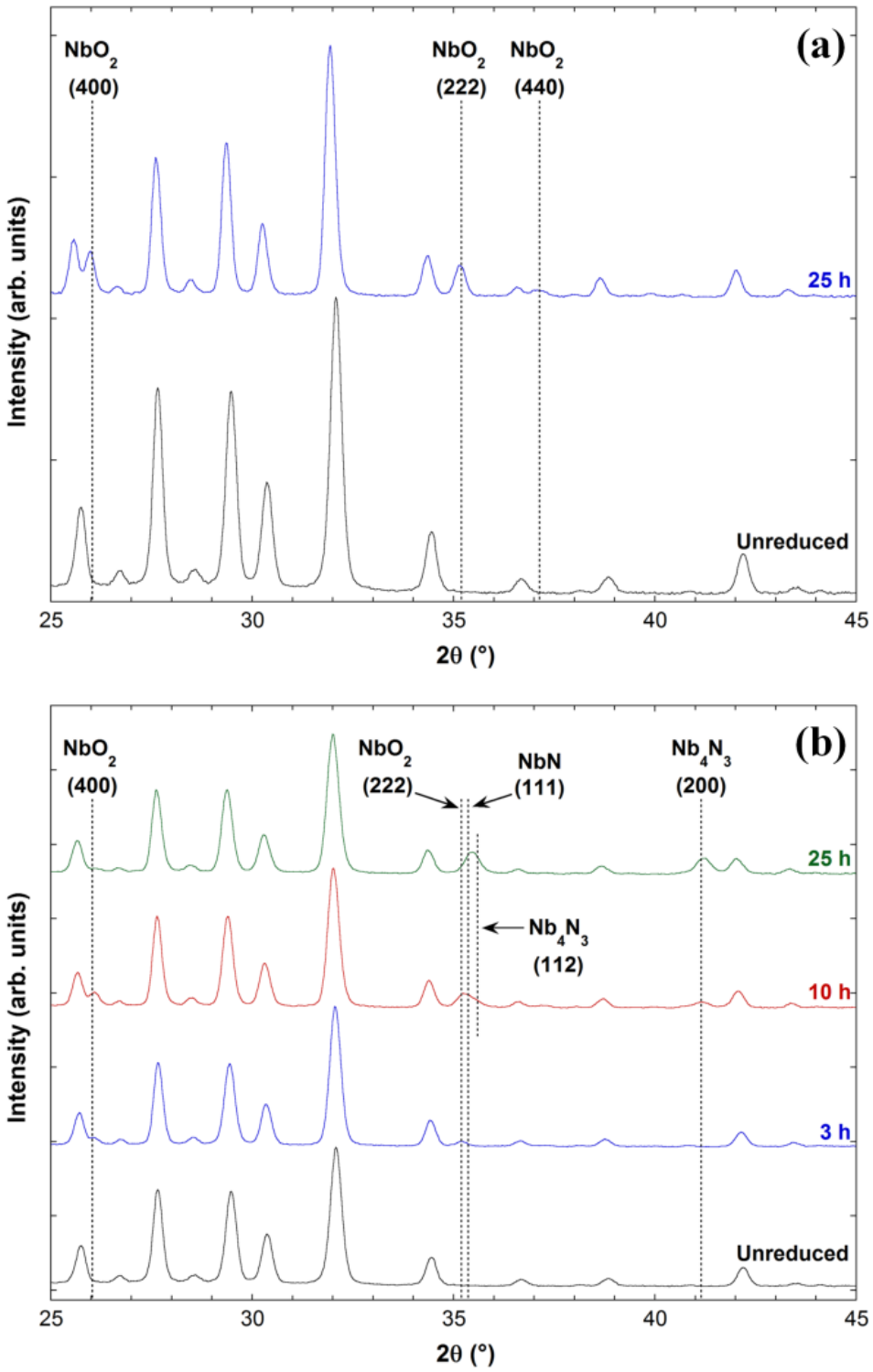

Figure 4.4. XRD patterns for SBN50 after reduction in (a) Ar/H_2 for 25 h and (b) N_2/H_2 for 3, 10, and 25 h; the pattern for unreduced, single-phase SBN50 is included for comparison.

NbN and/or the (112) plane of Nb_4N_3. Furthermore, an additional peak corresponding to the (200) plane of Nb_4N_3 appears after 10 h. Upon increasing the reduction time to 25 h, the NbO_2 (400) peak disappears almost completely, and the maximum intensity of the peak initially located at the NbO_2 (222) position continues to shift toward higher 2θ angles, likely due to the elimination of NbO_2 and the increased formation of NbN/Nb_4N_3. This scenario is supported by the increase in intensity of the (200) peak from Nb_4N_3 after the 25 h reduction time. From the XRD findings, it would appear that under the current N_2/H_2 and Ar/H_2 reduction conditions, a certain amount of octahedrally coordinated Nb in the SBN lattice is converted to NbO_2. For the case of annealing SBN in N_2/H_2 ambient, NbO_2 serves as an intermediate phase in the formation of NbN and/or nitrogen-deficient NbN. The presence of H_2 in this reaction is essential, as no secondary phases were detected for a sample reduced in N_2 only (not shown).

When the charge transport properties of both NbO_2 and NbN are considered, the results obtained here may be utilized to increase the thermoelectric performance of SBN ceramics. At room temperature, NbN displays metallic behavior, while NbO_2 is an *n*-type semiconductor with a low electrical conductivity and high Seebeck coefficient.[147,148] Therefore, maximization of the power factor could be realized by reducing SBN powders in each reduction environment and then combining them in various proportions prior to sintering.

4.2. Morphological examination

Initially, SBN50 pellets were sintered in air at a temperature of 1275 °C. However, as shown in the SEM image of Figure 4.5(a), a morphology consisting of very large grains surrounded by smaller rod-like grains was observed. The formation of such a structure has been noted in previous research and is indicative of abnormal grain growth (AGG). In a study on SBN60

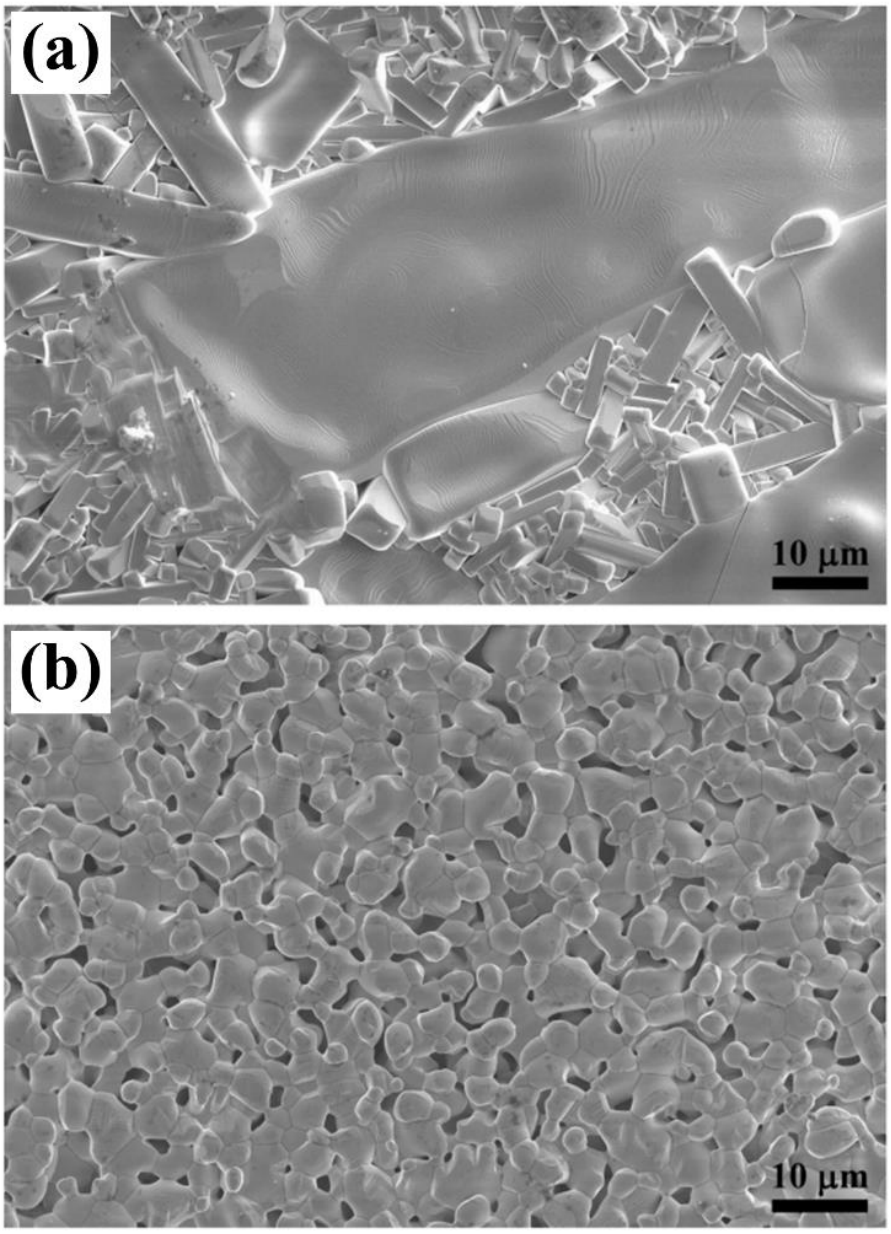

Figure 4.5. SEM images obtained for SBN50 pellets sintered at (a) 1275 °C and (b) 1250 °C. Abnormal grain growth is observed at the 1275 °C sintering temperature, while the sample sintered at 1250 °C exhibits a morphology with equiaxed grains.

fabricated via solid-state processing, an increase in the sintering temperature by only 10 °C (from 1250 to 1260 °C) induced the formation of abnormally large grains.[99] When the sintering temperature was further increased to 1300 °C, a duplex structure consisting of smaller rod-like grains and abnormally large grains was observed. The authors attributed the onset of abnormal

grain growth to localized melting of Nb-rich, Ba-poor phases at the grain boundaries. In other work on sol-gel-processed SBN50, a rod-like morphology and abnormal grain growth were observed for samples sintered at 1150 °C.[131] Since the particles in that study were fabricated via a wet chemistry route, it was suggested that abnormal grain growth could occur without localized melting. Instead, preferential sintering of aggregates may occur early on in the sintering process (~1000 °C). In the latter stages of sintering at higher temperatures, the shape of many grains changes from sphere to rod-like and preferential growth of the rod-like structures ensues along the *c*-axis. It was suggested that a reduction in the formation of aggregates and a lowering of the sintering temperature could serve to eliminate the onset of abnormal grain growth. Given the findings in previous research, the sintering temperature was lowered to 1250 °C and the morphology of the pellets was re-examined. Figure 4.5(b) shows an SEM image obtained for an SBN50 sample sintered at 1250 °C for 4 h. As evident in the figure, a morphology consisting of equiaxed grains was produced at this lower sintering temperature.

The effect of sintering time on morphology was also explored. Shown in Figure 4.6(a) and (b) are SEM images obtained for the SBN50 sample in Figure 4.5(b). It should be noted that the images in Figure 4.6 were acquired at a higher accelerating voltage of 15 kV (rather than 5 kV for the images in Figure 4.5) so that the more intricate features of the microstructure could be resolved. A rather porous microstructure with grains approximately 1 – 3 μm in size was produced at a 4 sintering time; the relative density of the sample was found to be ~74%. An increase in the sintering time to 24 h yielded a denser (~88% relative density) specimen with significantly larger grains, as evident from the SEM images shown in Figure 4.6(c) and (d). However, as displayed in the inset of Figure 4.6(c), AGG was observed at different regions of the 24 h sample. Given that extensive cracking was also noted at numerous locations after longer sintering durations, a 4 h sintering time

was employed in future experiments. Upon proper calibration of the furnace thermocouples, consistent relative densities of approximately 80-81% were achieved for SBN50 after a 4 h sintering treatment.

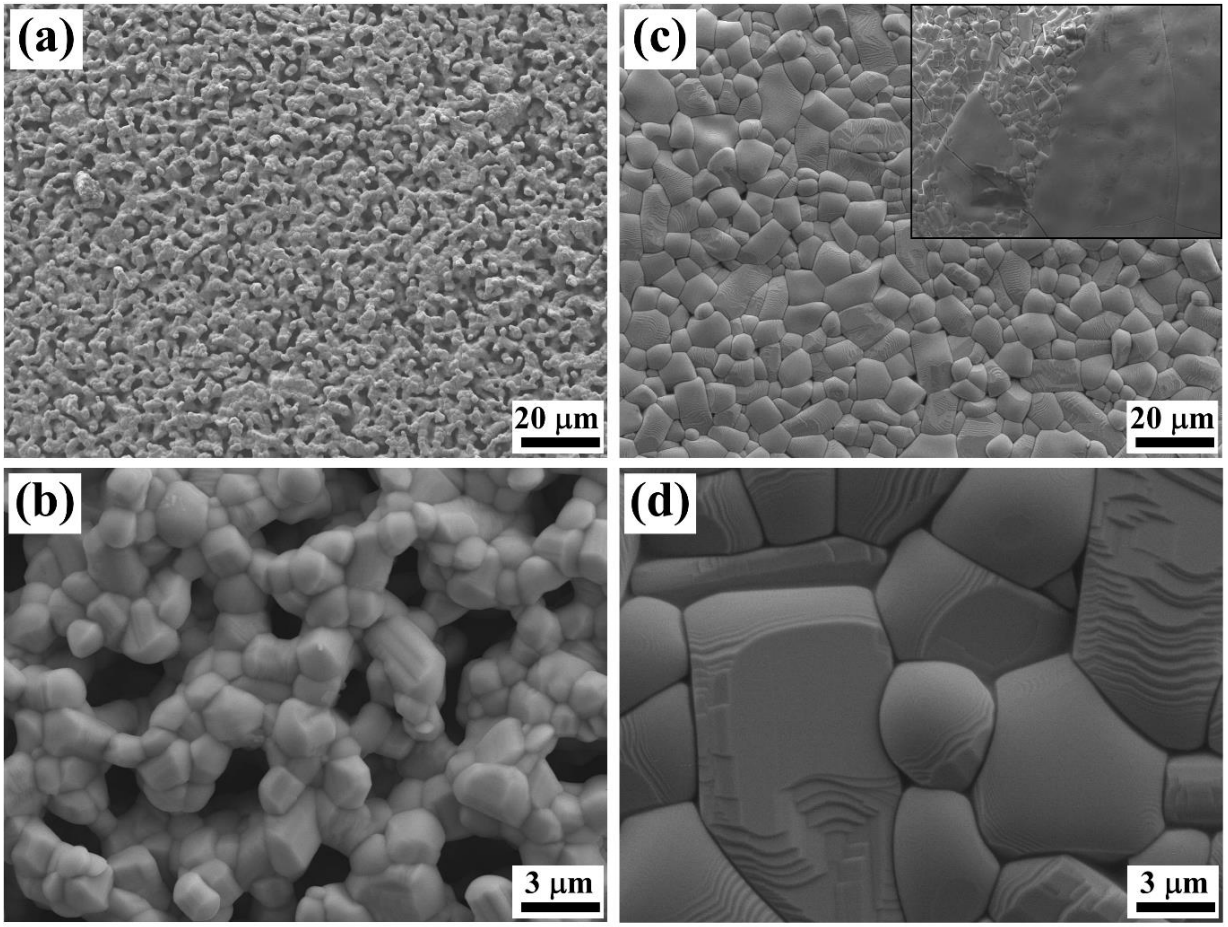

Figure 4.6. SEM images obtained for SBN50 sintered at 1250 °C for (a)-(b) 4 h and (c)-(d) 24 h. The inset of (c) shows an image acquired at a different region of the 24 h sample; abnormal grain growth is evident.

Chapter 5. X-ray Photoelectron Spectroscopy Analysis

5.1. Unreduced SBN with different Sr:Ba ratios

Prior to detailing results obtained from the TE testing of reduced SBN, the findings from XPS analyses will be discussed. For an examination of cation site occupancy in unreduced SBN, Sr and Ba $3d_{5/2}$ XPS spectra were acquired from unreduced $Sr_xBa_{1-x}Nb_2O_6$ samples with x = 0.20, 0.30, 0.50, and 0.61 (the congruent composition); the results are shown in Figure 5.1(a) and (b), respectively. The Sr 3*d* spectra were deconvolved using a spin-orbit splitting of Δ = 1.75 eV and a $3d_{3/2}$:$3d_{5/2}$ ratio of 2:3.[149] Both the Sr and Ba 3*d* data for each sample were scaled to the Nb 3*d* emission intensity and shifted such that the Nb^{5+} peaks have the same energy as that observed for the SBN50 specimen (this was necessary to account for both slight charging of the insulating pellets and surface contamination that shifted the work function during transfer to the XPS system). Upon aligning the Nb^{5+} peaks, a very slight shift in the Ba 3*d* and Sr 3*d* XPS spectra toward lower binding energies is observed with an increase in the Sr content; the shift is consistent for each individual Sr and Ba spectrum at the specific compositions. Fitting performed on the un-deconvolved Sr spectra revealed two distinct spin-orbit pairs separated by 1.12 ± 0.05 eV, which is much larger than the shift observed after aligning the Nb^{5+} peaks. The low binding energy Sr $3d_{5/2}$ peak dominates for SBN20 and saturates in intensity with increasing x (Sr concentration). In contrast, the intensity of the higher binding energy peak is initially small but increases steadily with x. Furthermore, only one spin-orbit pair was observed in the Ba $3d_{5/2}$ spectra and, as expected, its intensity decreases with increasing x.

We assign the high and low binding energy components in Figure 5.1(a) to Sr in A2 and A1 sites, respectively, and the single $3d_{5/2}$ peak in Figure 5.1(b) to Ba occupying A2 sites. In a

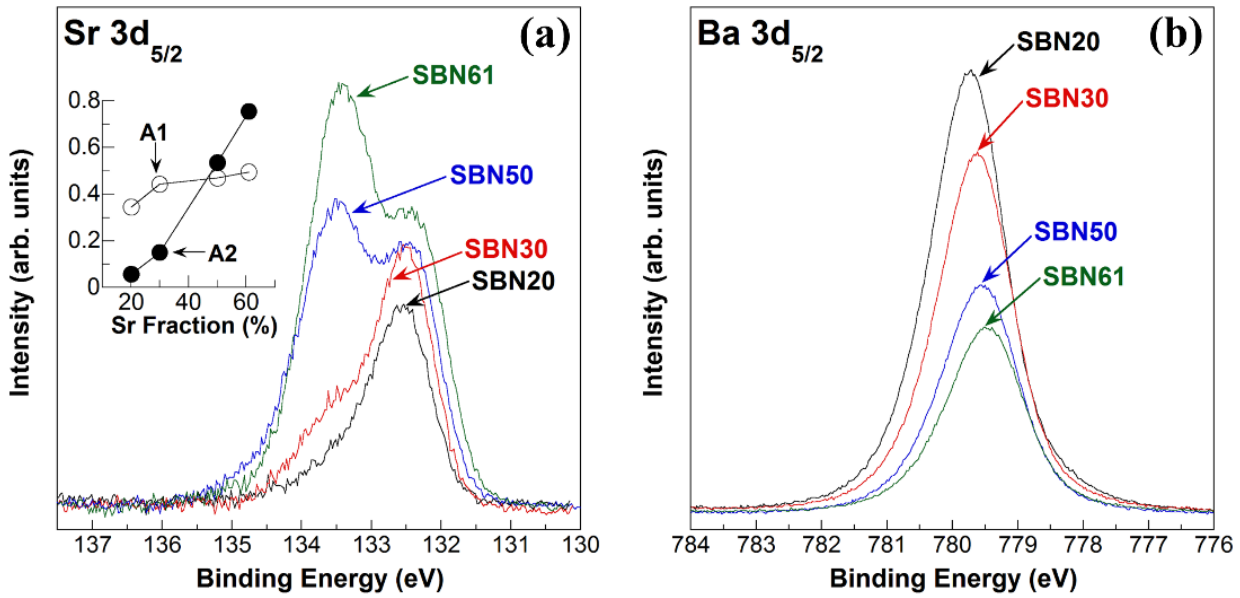

Figure 5.1. (a) Sr $3d_{5/2}$ XPS spectra for SBN with different Sr:Ba ratios; the relative A1 (open circles) and A2 (closed circles) peak intensities with respect to the Sr fraction are shown in the inset. (b) Ba $3d_{5/2}$ XPS results for the samples in (a).

comprehensive XRD study on SBN single crystals, the site occupancy of Sr in the A1 site was found to vary only slightly in the range of $0.25 \leq x \leq 0.75$, while that of Sr in the A2 site decreased toward zero and that of Ba in the A2 site increased as the Sr fraction was reduced.[150] The same trend is observed in the inset of Figure 5.1(a) if we attribute the low binding energy peak (open circles) to the A1 site and the higher binding energy peak (closed circles) to Sr in the A2 site. Furthermore, it was stated earlier that the SBN unit cell has the general formula $(A1)_2(A2)_4(C)_4(B1)_2(B2)_8O_{30}$, with one out of the six total A1 and A2 sites vacant. Each unit cell comprises five SBN formula units and thus, in the case of SBN20, there are 4 Ba atoms and 1 Sr atom in each unit cell. Since Ba can only occupy the A2 site regardless of the SBN composition, all A2 positions in the SBN20 unit cell must be occupied by Ba atoms, leading to an absence of an A2 peak in the Sr 3*d* spectrum for SBN20. The higher binding energy for Sr in the A2 site is likely a result of the larger coordination number for Sr atoms on the A2 site (15) when compared to those at the A1 site (12) [see Figure 2.7]. Increased coordination may result in a lower electron density

around Sr cations in the A2 position, which in turns leads to an increase in binding energy when compared to Sr 3*d* electrons at A1 sites. In previous work on SBN61 single crystals, the Sr peak at higher binding energy was attributed to a surface component, but no take-off angle dependence was observed for these bulk polycrystalline samples.[151]

5.2. Reduced SBN photoemission

To investigate the change in the Nb oxidation state after reduction annealing, exterior Nb 3*d* XPS spectra were acquired from SBN50 specimens reduced in N_2/H_2 at 900 – 1150 °C for 2 h. The top graph in Figure 5.2 shows the Nb $3d_{5/2}$ XPS spectra obtained for as-sintered (unreduced) and reduced SBN50 pellets; the binding energy corresponding to Nb in the 5+ state is set to zero on the *x*-axis. It is evident that as the reduction time is increased, the peak areas associated with Nb^{5+} decrease, while those corresponding to Nb with a lower valence increase. Such behavior is consistent with Eq. (2.16), where Nb undergoes a change in valence during the reduction heat treatment. To further analyze the Nb 3*d* XPS data, the Nb^{5+} peak was subtracted from the spectra to allow for a closer examination of the lower valence Nb signals. As shown in the bottom graph of Figure 5.2, peaks located at two different binding energies are observed after reduction at temperatures of 1000 – 1150 °C. When considering these two classes of peaks, it was found that the intensity ratio of the higher binding energy peak to lower binding energy peak is maximum for the specimen reduced at 1000 °C. As will be shown in Chapter 6, such observations could allow for the possibility of using XPS to configure reduction conditions for optimum TE performance.

Changes in the local environment after reduction annealing were investigated with XPS. Shown in Figure 5.3(a) are the interior Nb $3d_{5/2}$ spectra for SBN50 in its unreduced state and after reduction in N_2/H_2(5%) for 3, 10, and 25 h (black lines); the spectrum obtained after a 25 h

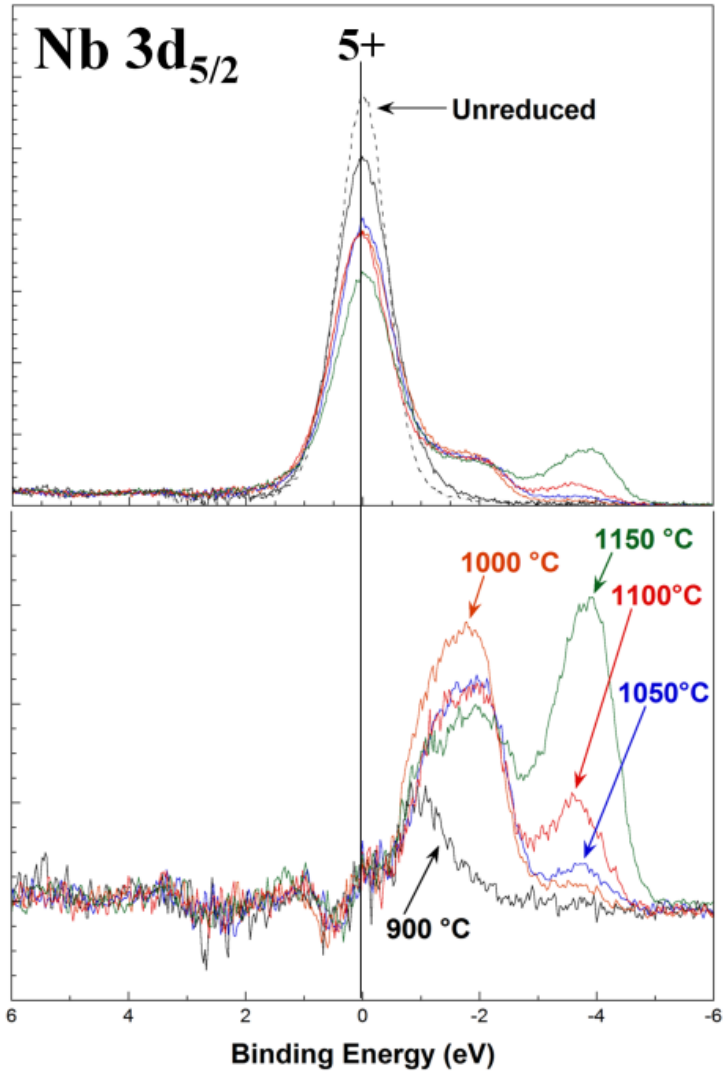

Figure 5.2. The Nb $3d_{5/2}$ spectra for SBN50 reduced for 2 h at various temperatures before (top) and after (bottom) subtraction of the Nb^{5+} peaks.

reduction in Ar/H_2(5%) is also displayed (blue line). In both reducing environments, the Nb emission intensity shifts out of the Nb^{5+} peak into lower binding energy states associated with lower valence. Such a scenario is in agreement with the reaction given in Eq. (2.16). Furthermore, Nb $3d_{5/2}$ data from the exterior of the specimen reduced for 25 h in N_2/H_2 (red dotted line) showed a distinct peak at a binding energy approximately 3.5 eV lower than that of the Nb^{5+} peak (similar to the samples reduced from 1000 – 1150 °C in Figure 5.2). This binding energy difference is consistent with the separation between the Nb $3d_{5/2}$ peaks of Nb_2O_5 and NbN,[149] indicating the

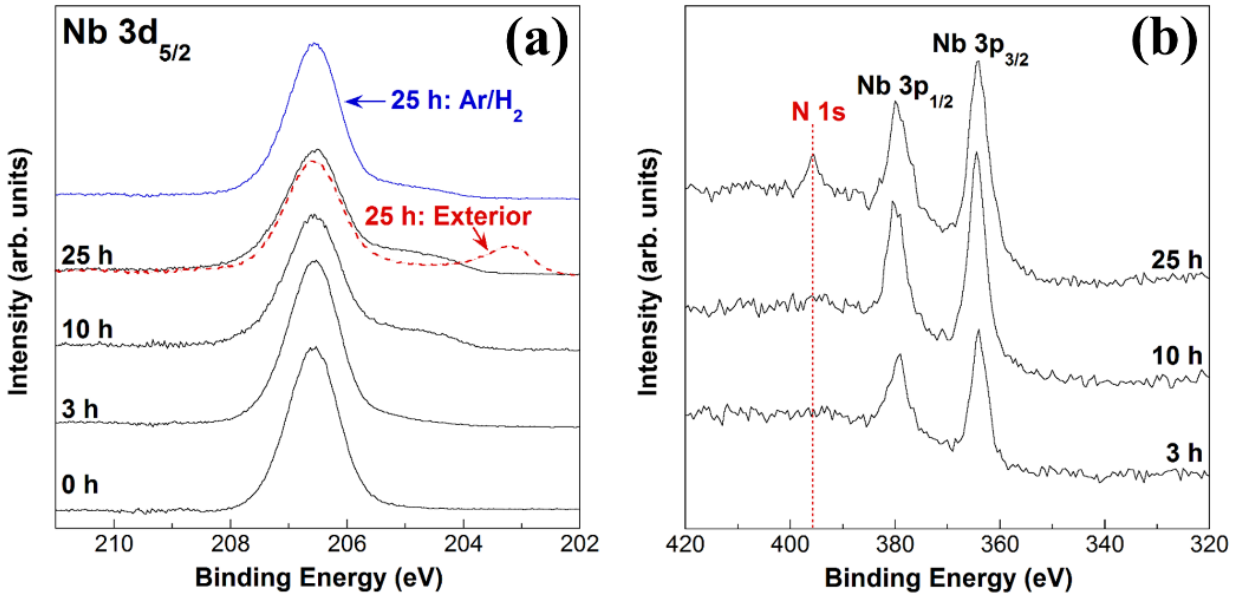

Figure 5.3. (a) Nb 3$d_{5/2}$ XPS results for SBN50 before annealing and after reduction in N_2/H_2 for 3, 10, and 25 h (solid black lines); the spectrum obtained on the exterior after annealing in N_2/H_2 for 25 h is also shown (red dotted line) along with the Nb 3$d_{5/2}$ photoemission after reduction in Ar/H_2 for 25 h (solid blue line). (b) Portion of the XPS survey spectra obtained at the exterior of SBN50 after reduction in N_2/H_2 for various time durations; the position of the N 1*s* peak is denoted with a red dotted line.

formation of NbN phases at the surface upon reduction in N_2/H_2. Confirmation of NbN formation with N_2/H_2 reduction was provided in Figure 4.4(b), and additional evidence of nitrogen incorporation is provided by XPS survey scans acquired for the exterior of the 3, 10, and 25 h specimens [Figure 5.3(b)], where a N 1*s* peak appears and then grows in intensity as the reduction time in N_2/H_2 is increased.

Shown in Figure 5.4(a) are the interior Sr 3$d_{5/2}$ XPS spectra for SBN50 in its as-sintered (unreduced) state and after reduction in N_2/H_2 for 3, 10, and 25 h. While the component corresponding to Sr on the A1 site displays little change in position with respect to reduction time, the peak associated with Sr occupancy at the A2 site exhibits a shift to lower binding energy as the reduction time is increased, suggesting a change in the local environment around the A2 site and an increase in the electron density at this location. This phenomenon was also observed in the Sr 3$d_{5/2}$ spectrum obtained for SBN50 annealed in Ar/H_2 for 25 h [Figure 5.4(c)].

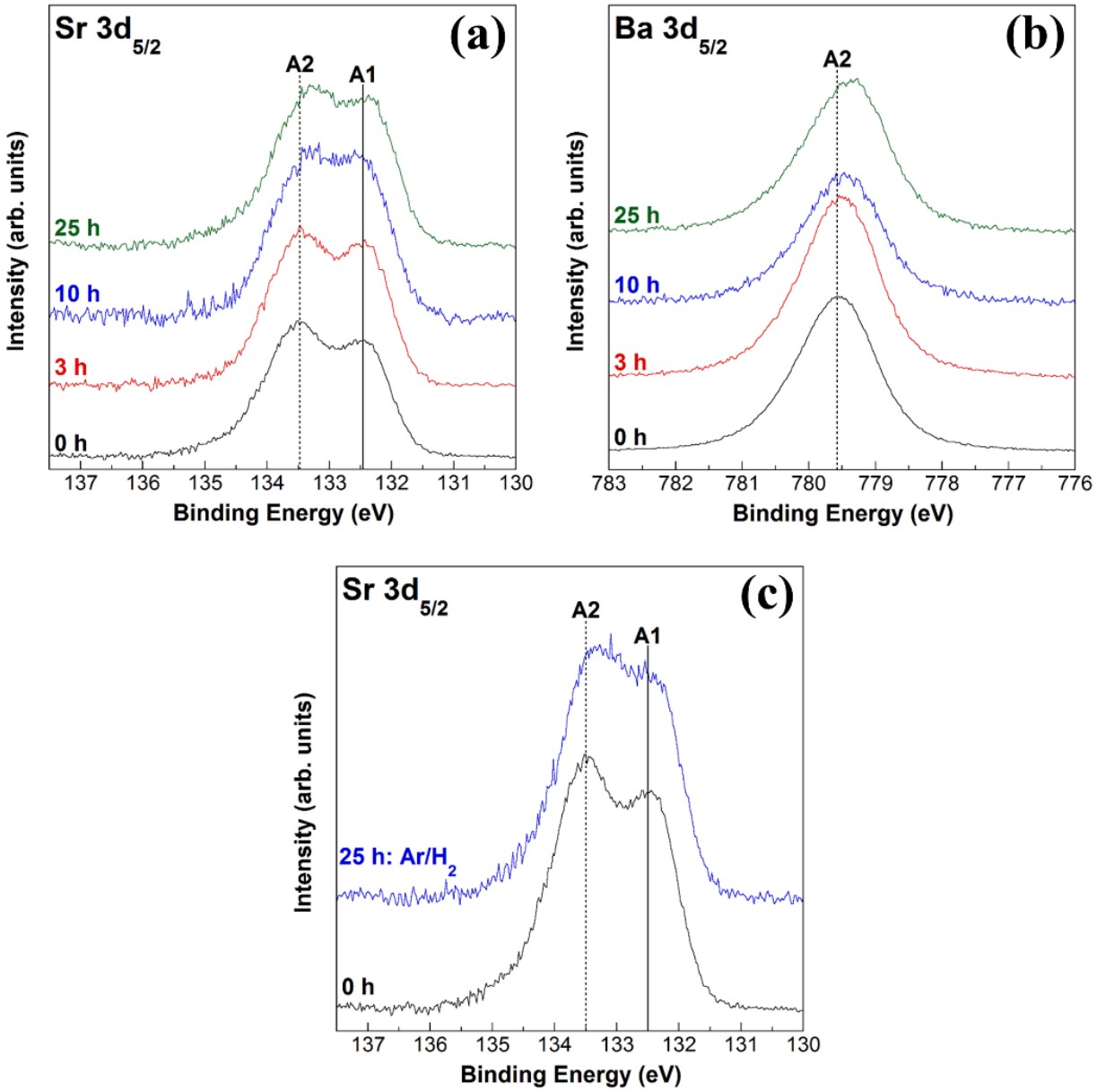

Figure 5.4. (a) Sr $3d_{5/2}$ and (b) Ba $3d_{5/2}$ XPS spectra after reduction in N_2/H_2 for various time durations. (c) Sr $3d_{5/2}$ XPS spectra obtained before annealing and after reduction in Ar/H_2 for 25 h.

As the A2 site in the SBN lattice is occupied by both Sr and Ba ions, additional photoemission data were acquired for the Ba $3d_{5/2}$ state; the results are shown in Figure 5.4(b). A shift in the Ba $3d_{5/2}$ peak to lower binding energy is apparent at longer reduction times. One possible mechanism to explain the observed trends may be the preferential formation of oxygen vacancies at octahedral 4*c* sites, which lie adjacent to both A2 positions and vacant C sites in the

SBN structure. The creation of an oxygen vacancy at this position serves to increase the electronic density around the adjacent Nb atom, which in turn has a small secondary effect on the cation in the A2 site. Consequently, Sr^{2+} and Ba^{2+} ions may be transformed to $Sr^{(2-\alpha)+}$ and $Ba^{(2-\beta)+}$, respectively, where $\alpha > \beta$ due to the slightly higher electronegativity of Sr when compared to Ba (1 for Sr versus 0.9 for Ba).[45] This could give rise to the observed shift in photoemission from Sr and Ba cations at A2 sites. Such a scenario is consistent with findings from previous research, where the oxygen vacancy formation energy was found to be lowest at octahedral 4*c* sites.[152]

Chapter 6. Thermoelectric Performance of Reduced SBN

6.1. Variation of the reduction temperature

The TE results obtained for reduced SBN50 will now be discussed. For the initial experiments, SBN50 samples annealed in N_2/H_2 at various temperatures for 2 h were tested for their TE properties. It should be noted that these specimens are in fact the same ones utilized to examine the effect of reduction temperature on the Nb oxidation state (see Figure 5.2). Shown in Figure 6.1(a) – (c) are plots of $|S|$, σ, and the power factor, respectively, for the reduced SBN50 pellets. The magnitude of the Seebeck coefficient increased over the entire measurement range for all samples, and a maximum $|S|$ of 261 μV/K was observed at 930 K for the sample reduced at 900 °C. Interestingly, the electrical conductivity of the samples reduced at temperatures of 1000 – 1150 °C increased with respect to the testing temperature ($d\sigma/dT > 0$) up to approximately 650 K, then decreased with a further rise in T ($d\sigma/dT<0$). It has been proposed that this change is due to the existence of polarized nanodomains above T_m for particular SBN compositions. However, as will be discussed in Section 6.4, the findings obtained in this study seem to contradict such a notion.

The power factors obtained for the SBN50 samples demonstrate the importance of finding an optimal balance between S and σ. While the sample reduced at 900 °C displayed the highest Seebeck coefficients, the lowest power factor (1.09 μW/cm·K^2) was obtained for this specimen at 930 K due to the reduced electrical conductivity of the material. At the same time, the σ values of the samples reduced at temperatures of 1050 – 1150 °C were offset by the lower Seebeck coefficients of these materials and thus, lower power factors were also observed. In contrast, the sample reduced at 1000 °C exhibited a maximum power factor of 1.78 μW/cm·K^2 at 930 K due to an ideal combination of S and σ. It is worth recalling that, in the XPS spectra acquired for the

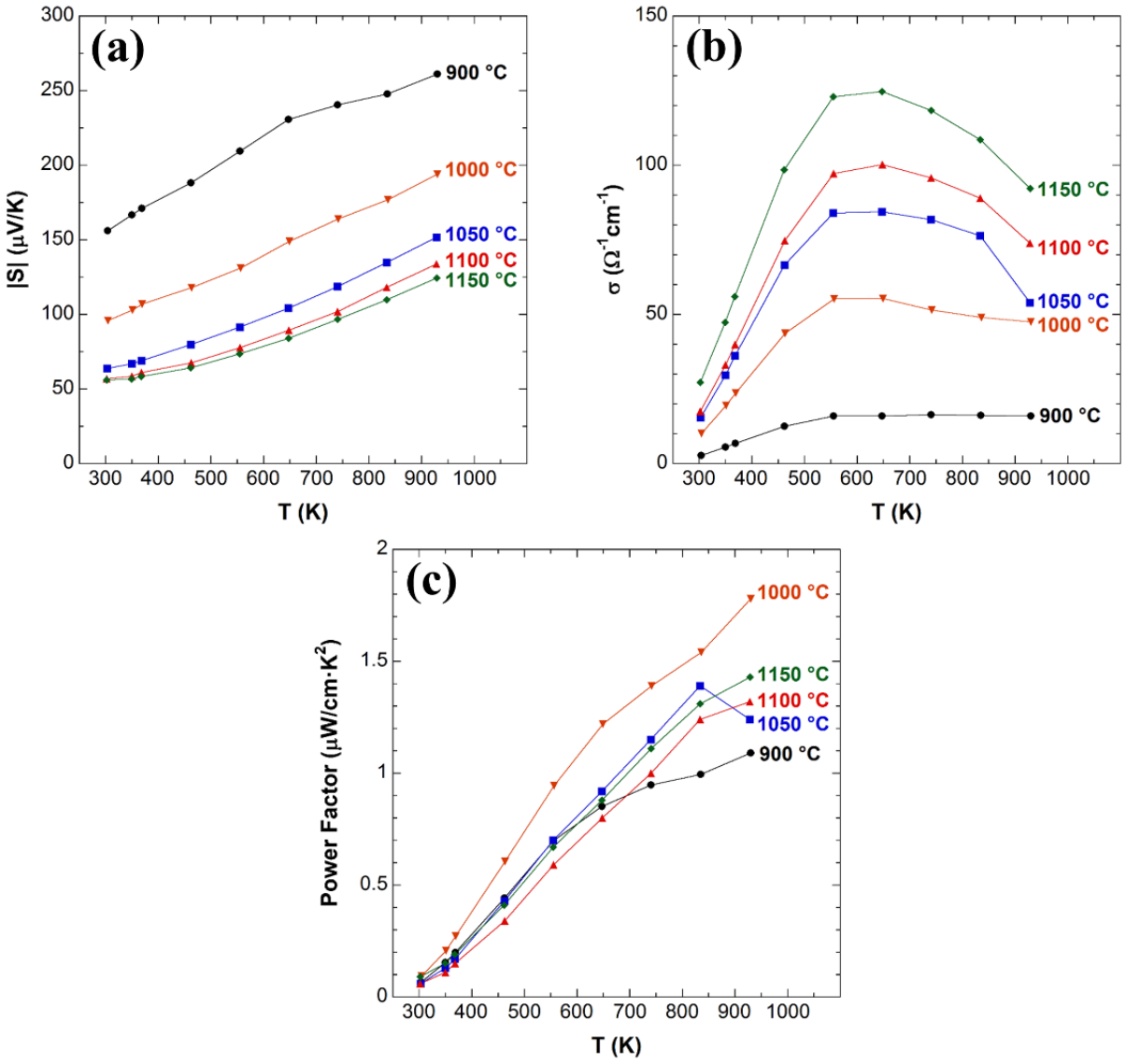

Figure 6.1. (a) Magnitude of the Seebeck coefficient, (b) electrical conductivity, and (c) power factor of SBN50 pellets reduced at 900 – 1150 °C.

SBN50 specimens (Figure 5.2), subtraction of the Nb^{5+} peak from the data allowed two distinct classes of peaks with different binding energies to be resolved. Furthermore, it was the 1000 °C sample that also displayed the largest intensity ratio of the high binding energy peak to low binding energy peak. Such a finding points to the possibility that XPS could be used as a tool for optimizing the reduction conditions for maximum TE performance.

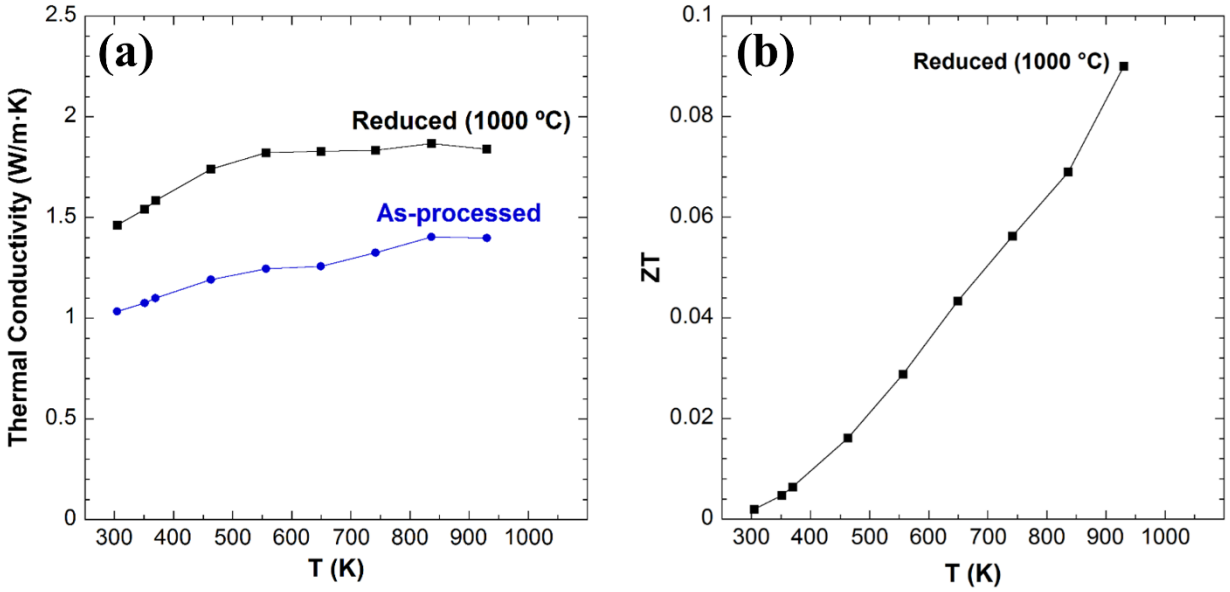

Figure 6.2. (a) The thermal conductivity of as-sintered (unreduced) and reduced (1000 °C) SBN50 with respect to temperature. (b) The dimensionless figure of merit (*ZT*) of SBN50 reduced at 1000 °C with respect to temperature.

Thermal conductivity values with respect to temperature were obtained for SBN50 in its as-sintered state (unreduced) and after reduction at 1000 °C; the results are shown in Figure 6.2(a). As-sintered SBN50 was found to exhibit a low κ of approximately 1.03 W/m·K at room temperature. This value increased to about 1.4 W/m·K at 930 K. In previous research, a roomtemperature κ value of 1.6 – 1.7 W/m·K was measured for an unreduced single crystal of SBN52 at room temperature.[103] For the SBN50 sample reduced at 1000 °C for 2 h, the thermal conductivity was approximately 1.46 W/m·K at room temperature and 1.84 W/m·K at 930 K. When compared to earlier work, the room temperature κ value is almost identical to that obtained at 300 K for a polycrystalline SBN61 sample reduced at 1300 °C for 30 h. Overall, the trends in the thermal conductivity behavior are consistent with the findings of previous research, where it was noted that the κ of SBN does not conform to conventional crystalline solid behavior and instead exhibits magnitudes and trends similar to those of amorphous SiO_2.[103,153,154] It has been proposed that the low κ values observed for SBN and other relaxor ferroelectrics is the result of

enhanced phonon scattering due to the existence of PNRs.[29] Such a notion would explain the rise in κ with temperature, as the gradual disappearance of PNRs up to the Burns temperature (T_B) could serve to increase the thermal conductivity.

To examine the impact of electron transport on the increase in thermal conductivity after reduction, the electronic contribution to the thermal conductivity (κ_e) was calculated from the Wiedemann-Franz law. It was found that, at 300 K, κ_e was approximately 7.51×10^{-3} W/m·K (~0.5% of the total thermal conductivity), while at 930 K, κ_e was about 0.11 W/m·K (~5.8% of the total thermal conductivity). In other words, the overall thermal conductivity is dominated by the contribution from phonons (κ_l), as is typical with many ceramic materials.

Based on the obtained κ and power factor values, the value of *ZT* with respect to the testing temperature was calculated for SBN50 reduced at 1000 °C; the results are shown in Figure 6.2(b). The *ZT* value increased over the entire temperature range, and a peak *ZT* of 0.09 was achieved at 930 K. This maximum *ZT* value is comparable to that reported for the $CaMnO_3$ system, where a *ZT* of 0.16 was obtained at 1000 K for $Ca_{0.9}Yb_{0.1}MnO_3$.[155]

The electrical conductivity values obtained at specific temperatures for each reduction condition were used to estimate the formation enthalpy (Δh) of a doubly-ionized oxygen vacancy. For the reduction reaction in Eq. (2.15), the equilibrium constant (K_{Re}) may be expressed as:

$$K_{\mathrm{Re}} = [V_{\mathrm{O}}^{\bullet\bullet}]n^2(p\mathrm{O}_2)^{\frac{1}{2}} = K^{\circ}\exp\left(\frac{\Delta s}{k_B}\right)\exp\left(-\frac{\Delta h}{k_B T_{\mathrm{Re}}}\right) \tag{6.1}$$

where T_{Re} is the reduction temperature, K° is a normalizing constant, and Δs is the formation entropy of a doubly-ionized oxygen vacancy. Here, Δs is mainly related to the vibrational entropy,

the contributions of which tend to be small and on the same order when comparing different defect states.[156,157] Therefore, Eq. (6.1) can be written as:

$$K_{\mathrm{Re}} = [V_{\mathrm{O}}^{\bullet\bullet}]n^2(p\mathrm{O}_2)^{\frac{1}{2}} = K_1 \exp\left(-\frac{\Delta h}{k_B T_{\mathrm{Re}}}\right) \tag{6.2}$$

where K_1 is a constant that includes the entropy term. Utilizing the condition for electroneutrality, $n = [V_{\mathrm{O}}^{\bullet\bullet}]$, and assuming that the partial pressure of oxygen does not vary significantly at each reduction temperature (a reasonable assumption considering the constant flow rate of forming gas), the oxygen vacancy concentration may be expressed as:

$$[V_{\mathrm{O}}^{\bullet\bullet}] = K_2 \exp\left(-\frac{\Delta h}{3kT_{\mathrm{Re}}}\right) \tag{6.3}$$

where K_2 ($=4^{-1/3}p(\mathrm{O}_2)^{-1/6}K_1^{1/3}$) is a constant. Substitution of Eq. (6.3) into the electrical conductivity expression, $\sigma = qn\mu_e$ (where μ_e is the electronic mobility), and taking the natural logarithm of both sides yields the following:

$$\ln\sigma = \left(\frac{1}{T_{\mathrm{Re}}}\right)\left(-\frac{\Delta h}{3k}\right) + \ln K_3 \tag{6.4}$$

where K_3 ($=2K_2q\mu_e$) is a constant containing the electronic mobility term. It should be noted that, as a first approximation, we are assuming that the mobility does not vary significantly at one particular testing temperature for each of the samples. Plots of $\ln(\sigma)$ vs. $(10^4/T_{\mathrm{Re}})$, where σ is the electrical conductivity of the samples at various testing temperatures, are shown in Figure 6.3. The room temperature formation enthalpy associated with doubly-ionized oxygen vacancy formation is estimated to be ~3.85 eV.

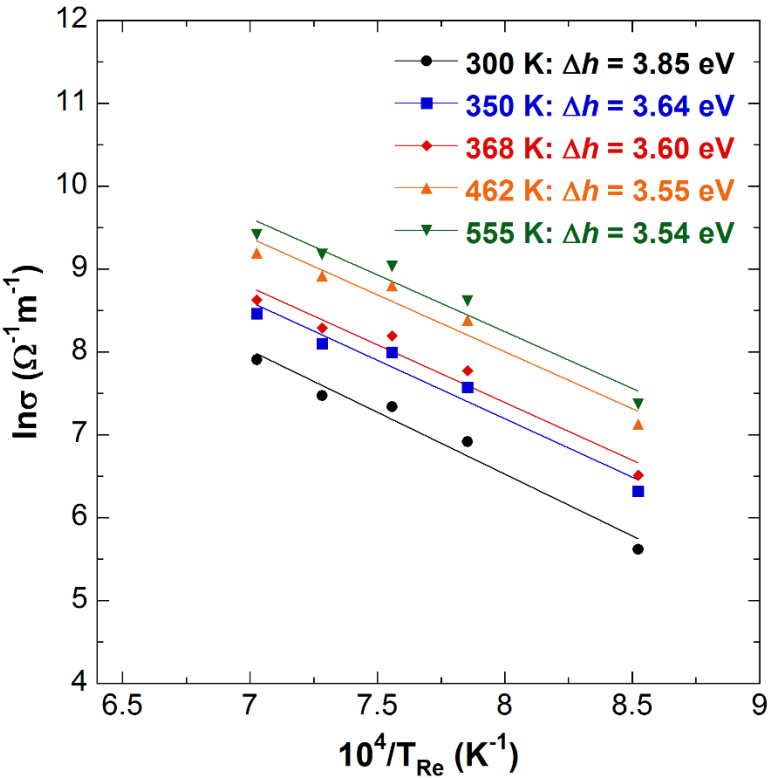

Figure 6.3. Plots of ln(σ) vs. $10^4/T_{Re}$, where T_{Re} is the reduction temperature and σ is the electrical conductivity of the samples at various testing temperatures.

6.2. Variation of the Sr:Ba ratio

To examine the effects of the Sr:Ba ratio on the TE performance, SBN30, SBN50, and SBN61 samples were reduced for 3 h at 1000 °C in N_2/H_2. The resulting power factor, κ, and ZT obtained for the specimens are shown in Figure 6.4(a) – (c), respectively. It should be noted here that the heat capacities used to determine the thermal conductivity values displayed in (b) were calculated by dividing $3R$ (where R is the universal gas constant) by the average atomic weight for each composition. It can be seen that the power factor and thermal conductivity of the SBN50 and SBN61 samples are quite comparable, and the values of both parameters for these compositions are higher than those measured for the SBN30 specimen. However, due to the reduction in κ for

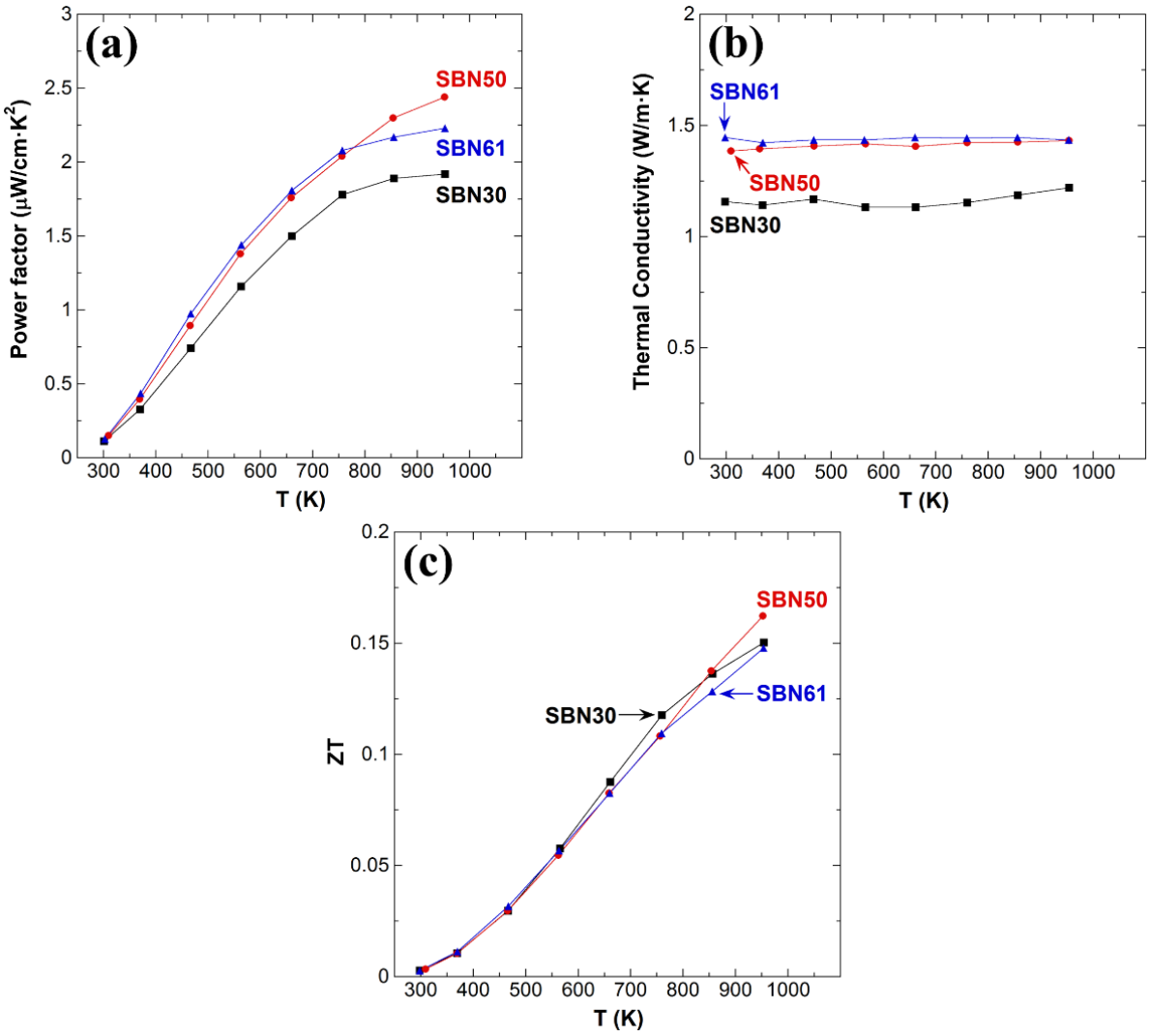

Figure 6.4. (a) Power factor, (b) thermal conductivity, and (c) *ZT* values obtained for SBN30, 50, and 61 specimens reduced for 3 h at 1000 °C.

SBN30, the *ZT* values calculated for all samples are very similar, with a peak *ZT* of ~0.16 obtained for reduced SBN50. Due to the similarities in the overall TE performance of the materials, SBN50 was used a representative material for further research into both the SBN conduction mechanism and the effects of reduction on TE performance.

6.3. Variation of the reduction time

Having selected SBN50 as a representative composition, sintered pellets were reduced at 1000 °C for different time durations. Shown in Figure 6.5(a) – (c) are the resulting |*S*|, σ, and power factor values for the tested specimens. From the figure, it can be seen that an increase in the reduction time led to both a decrease in |*S*| and a rise in σ. Furthermore, the trend of a parallel rise in |*S*| and σ up to a testing temperature of approximately 650 K was also observed for samples

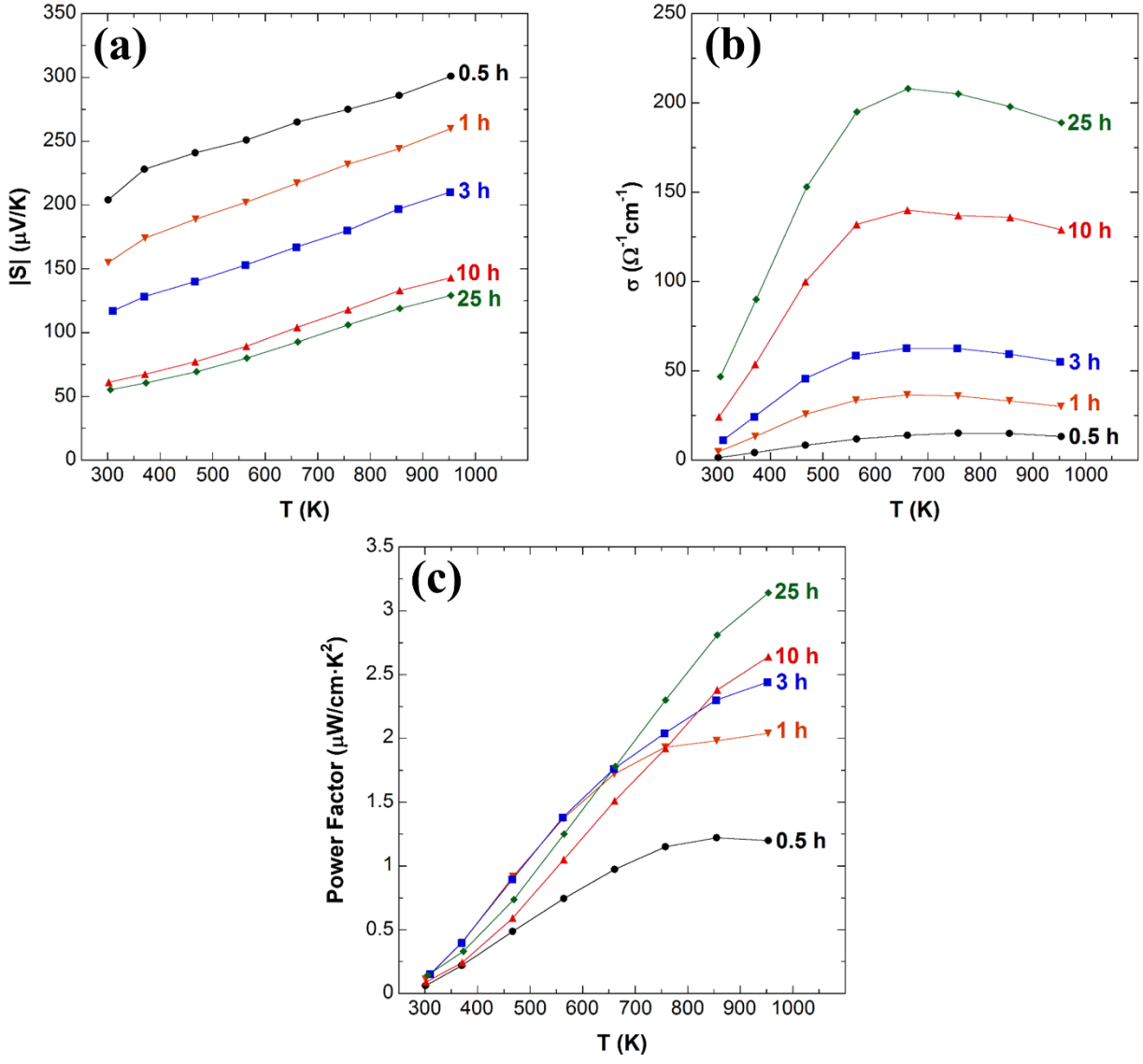

Figure 6.5. (a) Magnitude of the Seebeck coefficient, (b) electrical conductivity, and (c) power factor obtained for SBN50 reduced at 1000 °C for various times.

reduced at times exceeding 0.5 h. Ultimately, a peak power factor of 3.1 uW/cm·K^2 was obtained at ~950 K for SBN50 reduced for 25 h.

As evident in Figure 6.5(b), the electrical conductivity of the reduced SBN50 samples initially exhibits a temperature dependence consistent with that of a conventional *n*-type semiconductor, i.e., $d\sigma/dT > 0$. However, as the testing temperature is increased further, the electrical conductivity of the SBN specimens presents a more metallic-like temperature dependence with negative $d\sigma/dT$ values. One of the primary goals we seek to achieve is to develop a firm understanding of the electrical conductivity mechanisms in reduced SBN. Therefore, a sintered SBN50 was reduced for 25 h in N_2/H_2, and additional data points were acquired during the TE testing procedure. A thorough investigation of both the Seebeck coefficient and electrical conductivity trends was then conducted using models developed for charge transport in systems with localized carriers.

6.4. Electrical transport mechanisms

When examining the Seebeck coefficient and electrical conductivity data obtained thus far for reduced SBN samples, two primary trends are evident: 1) a parallel rise in $|S|$ and σ over a certain temperature range and 2) the gradient of the electrical conductivity with respect to temperature, $d\sigma/dT$, is initially positive (semiconductor-like temperature dependence) but then decreases, ultimately becoming negative (metallic-like temperature dependence) in more heavily reduced samples at elevated temperatures. To elucidate the underlying mechanisms responsible for the observed charge transport behavior, experiments were first conducted with the goal of evaluating the validity of an existing hypothesis proposed to explain the electrical conductivity of reduced SBN relaxor ferroelectrics.

It has been postulated that the aforementioned change in the sign of $d\sigma/dT$ for reduced SBN may be due to the existence of polarized nanoregions (PNRs) above the temperature of maximum dielectric constant (T_m).[29] As stated earlier, SBN relaxor ferroelectrics exhibit a broad, frequency-dependent transition from a ferroelectric to paraelectric state as the temperature is raised. Such behavior can be linked to the existence of PNRs, which continue to be present in the material several hundred degrees above T_m until the Burns temperature (T_B) is reached.[158,159] For the SBN system, T_B is stated to be approximately 350 °C (623 K) and is rather invariant to the degree of reduction (and thus, the carrier concentration).[33,96] Interestingly, the change in the sign of $d\sigma/dT$ for reduced SBN occurs very close to this temperature. Thus, it has been theorized that PNRs in SBN sustain semiconductor-like electrical conductivity behavior (i.e. $d\sigma/dT > 0$), even after extensive reduction, by hindering the extensive percolation of electrons through the material. Once the testing temperature is brought above T_B, the PNRs are eliminated and metallic-like electrical conductivity behavior (i.e., $d\sigma/dT < 0$) is observed due to the high carrier concentration induced during reduction annealing. For high-temperature TE applications, it would be beneficial if a positive $d\sigma/dT$ could be sustained at increasingly elevated temperatures, as this would serve to increase the power factor.

To test the above hypothesis, the TE characteristics of SBN were compared to those of an isostructural relaxor ferroelectric, $Ca_xBa_{1-x}Nb_2O_6$, (CBN100x, where $0.18 \leq x \leq 0.35$). While CBN and SBN possess very similar tetragonal tungsten bronze (TTB) structures,[160] T_m and T_B are both significantly higher for CBN. In particular, the Burns temperature of $Ca_{0.18}Ba_{0.82}Nb_2O_6$ (CBN18) has been reported to be as high as 1200 K, more than 500 K higher than that of SBN61.[161] It was thus proposed that if PNRs are primarily responsible for extending the region of semiconductor-like electrical behavior with respect to temperature, than the value of $d\sigma/dT$ should remain positive

up to higher temperatures during the testing of CBN. To determine if this is indeed the case, CBN18 powder was produced via SCS by simply replacing $Sr(NO_3)_2$ with a proper amount of $Ca(NO_3)_2$, and then adjusting the quantity of $Ba(NO_3)_2$ accordingly. The powder was then cold-pressed and sintered at 1350 °C for 12 h in air; XRD analysis confirmed the formation of single-phase CBN with the TTB structure. It should be noted that the relative density of the sintered CBN18 pellets was rather low, ~70% of the theoretical density. Under the same reduction annealing conditions, this lower density when compared to SBN could lead to a slightly higher carrier concentration due to the ease with which the N_2/H_2 mixture can permeate the specimen. However, given the much higher T_B of CBN18, it is unlikely that a change in $d\sigma/dT$ would occur at a lower temperature for reduced CBN18 if the presence of PNRs are primarily responsible for sustaining a semiconducting state.

Shown in Figure 6.6(a) – (c) are the respective values of $|S|$, σ, and the power factor obtained for CBN18 and SBN50 specimens reduced at 1000 °C for 25 h in N_2/H_2. The Seebeck coefficients of both compounds show similar trends, with $|S|$ increasing over the entire range of testing temperatures. An examination of the electrical conductivity data in Figure 6.6(b) reveals that a change in the sign of $d\sigma/dT$, from positive to negative, occurs at a lower temperature for CBN when compared to SBN reduced under the same conditions. Such a finding casts doubt on the notion that PNRs are chiefly responsible for sustaining a semiconductor-like temperature dependence of the electrical conductivity in reduced SBN. Moreover, the observed metallic-like temperature dependence of σ at lower temperatures for CBN18 implies that the point at which the sign of $d\sigma/dT$ changes may in fact be heavily influenced by the degree of reduction. This last point is evident in Figure 6.7, which shows the electrical conductivity measured for SBN61[100] single crystals reduced at 1000 °C for 25 and 50 h in N_2/H_2. As displayed in the figure, the point at which

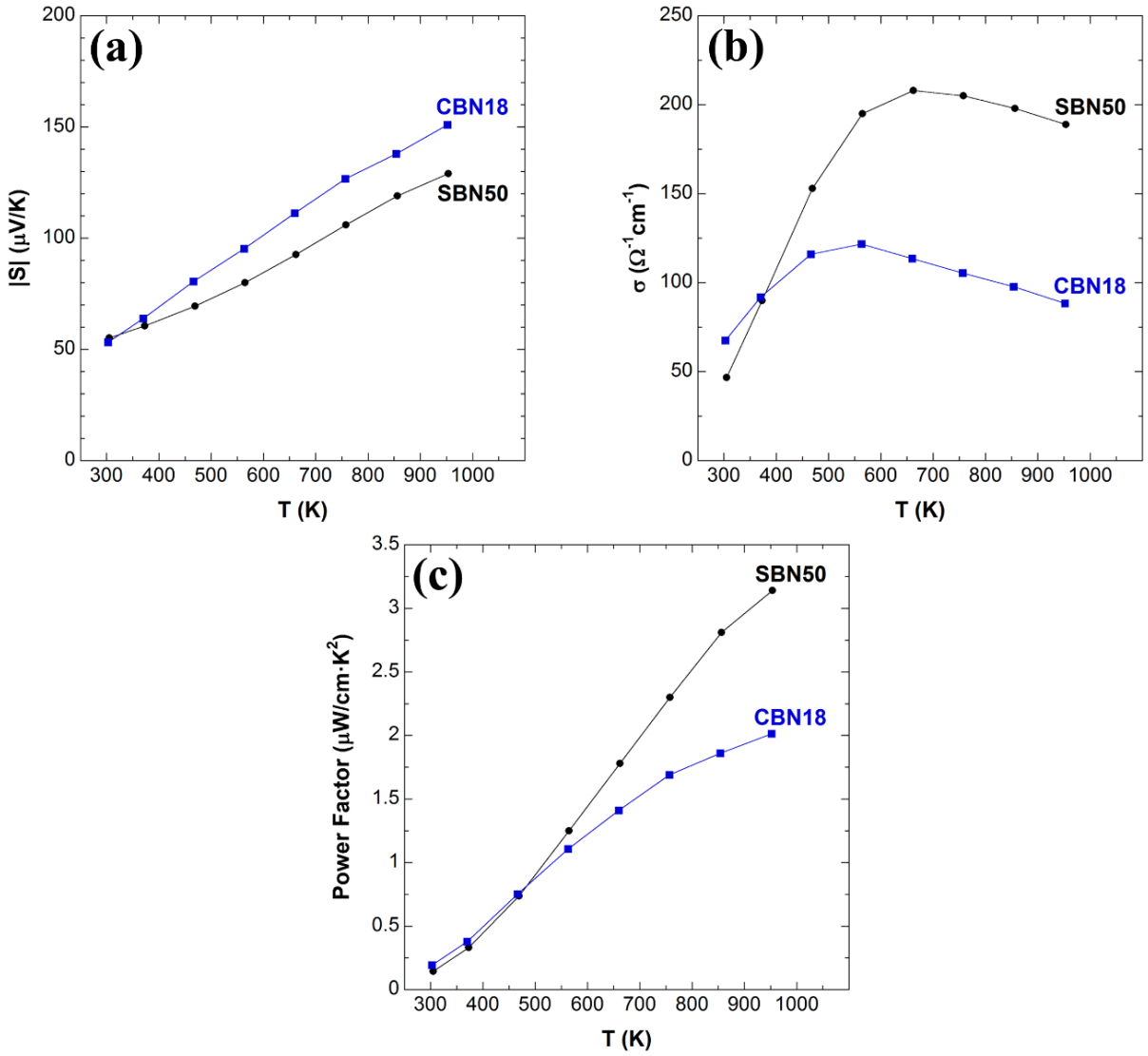

Figure 6.6. (a) Magnitude of the Seebeck coefficient (b) electrical conductivity, and (c) power factor obtained for SBN50 (solid black circles) and CBN18 (solid blue squares) reduced for 25 h at 1000 °C.

$d\sigma/dT$ changes from positive to negative appears to shift by ~100 K to lower temperatures as the reduction time is doubled.

In order to more clearly elucidate the mechanisms of electrical transport in reduced SBN, additional data points were acquired during the TE testing of an SBN50 sample reduced at 1000 °C for 25 h in N_2/H_2; the resulting plots of σ and $|S|$ are shown in Figure 6.8(a) and (b), respectively. The electrical conductivity can be roughly divided into two regions based on the observed trends

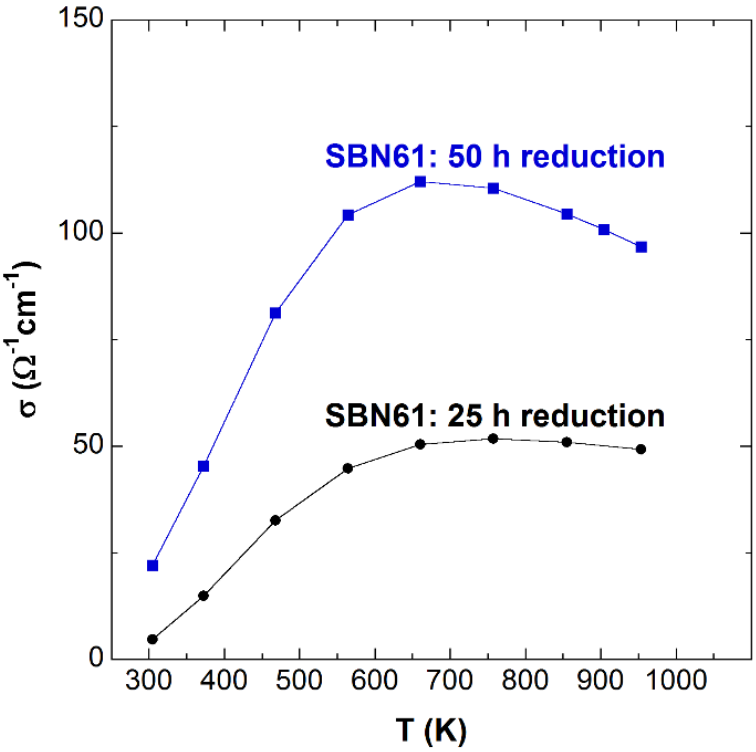

Figure 6.7. The electrical conductivity of SBN61[001] single crystals after reduction at 1000 °C for different time durations.

in $d\sigma/dT$. In the first region (region I), typical semiconductor behavior is displayed with an increase in σ as the temperature is raised. This regime of relatively constant, positive $d\sigma/dT$ persists up to approximately 615 K, at which point the gradient begins to show a noticeable decrease. In the area of the plot denoted as region II, $d\sigma/dT$ is significantly reduced and even becomes negative above 800 K, indicating a metallic-like temperature dependence of the electrical conductivity. Interestingly, the magnitude of the Seebeck coefficient exhibits a nearly constant increase from 450 – 900 K. The parallel increase of both $|S|$ and σ in region I can yield some insight into the electrical conductivity mechanism. For a non-degenerate, broad-band *n*-type semiconductor with a thermally activated carrier concentration, the Seebeck coefficient may be expressed as:[162,163]

$$S = -\frac{k_B}{q}\left(\frac{E_c - E_F}{k_B T} + A\right) = -\frac{k_B}{q}\left(\ln\frac{N_c}{n} + A\right) \tag{6.5}$$

where E_c and E_F are the conduction band and Fermi level energy, respectively, N_c is the effective density of states in the conduction band, n is the carrier concentration, and A is often viewed as a constant, the value of which depends on interactions between the crystal lattice and electrons in the conduction band. According to Eq. (6.5), an increase in carrier concentration with T can serve to reduce $|S|$ while increasing the electrical conductivity. However, if the carrier concentration does not change with temperature, $|S|$ may be proportional to the logarithm of T due to the dependence of N_c on $T^{3/2}$.[164] In addition, a rise in σ with T can be observed if electron transport occurs via thermally-activated polaron hopping, as charge carriers can more easily overcome the energy barrier associated with hopping to an adjacent site.

To identify the nature of electron transport in region I of Figure 6.8(a), the electrical conductivity data were fit according to the small polaron hopping (SPH) model [see Eq. (2.18)].

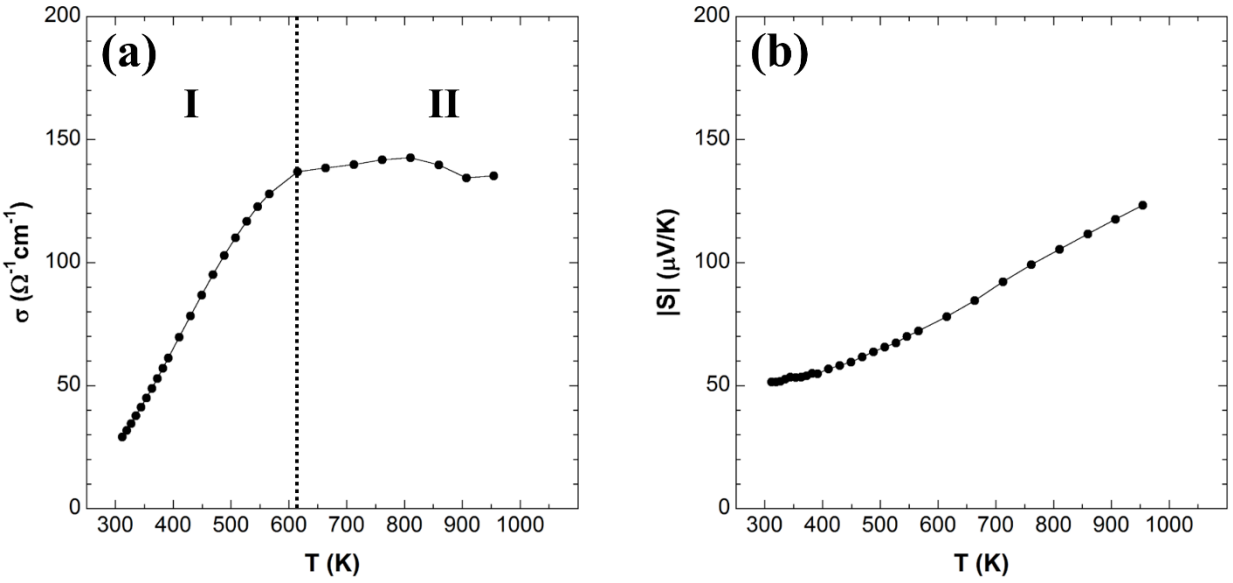

Figure 6.8. (a) Electrical conductivity and (b) $|S|$ with respect to temperature for an SBN50 sample reduced at 1000 °C for 25 h; two separate regions can be identified in the σ-T plot based on the value of $d\sigma/dT$.

Plots of $\ln(\sigma T^s)$ vs. $(10^3/T)$, where s = 1 for adiabatic hopping (solid black circles) and 3/2 for non-adiabatic hopping (solid blue squares), are displayed in Figure 6.9. It is evident that the electrical conductivity data in the temperature range of 300 – 545 K can be closely modeled according to adiabatic or non-adiabatic small polaron hopping with activation energies (E_a) of 126 and 143 meV, respectively. For adiabatic hopping, the motion of an electron is sufficiently rapid such that it is able to adjust to the instantaneous positions of atoms in the material.[165] In contrast, an electron is unable to follow rapid lattice fluctuations in the non-adiabatic case and thus, the probability of hopping is lower when compared to that in the adiabatic regime.[166] Regardless, it appears that thermally-activated small polaron hopping is the likely electrical conductivity mechanism in reduced SBN from room temperature to approximately 550 K. Further evidence to support SPH behavior was obtained by Hall measurements conducted at 400 K for an SBN50 sample reduced

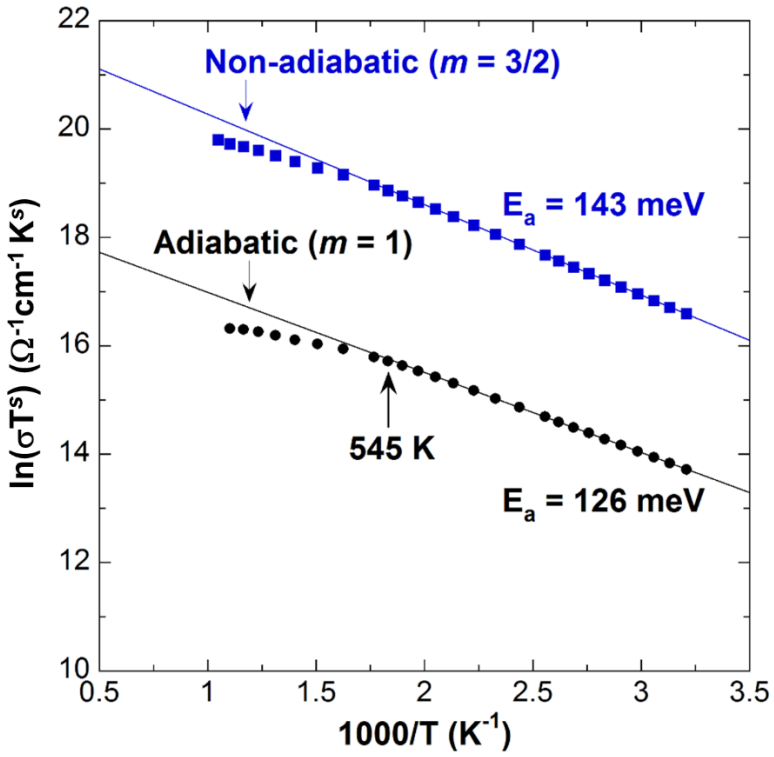

Figure 6.9. Plots of $\ln(\sigma T^s)$ vs. $10^3/T$ generated with the electrical conductivity data in Figure 6.8(a); fitting was performed in the temperature range of 300 – 545 K. The exponent s = 1 for adiabatic hopping (solid black circles) and 3/2 for non-adiabatic hopping (solid blue squares).

at 1000 °C in N_2/H_2 for 3 h. The lower reduction duration was necessary in order to increase the voltage signal and enhance the signal-to-noise ratio. Based on the σ values acquired after a 3 h reduction, the measured carrier concentration was 1.7×10^{21} cm^{-3}, which corresponds to an electronic mobility of ~0.1 $cm^2/V \cdot s$. Such a low value is consistent with conduction via the SPH mechanism. In a study on Cr-doped SBN61 single crystals, the room temperature electron mobilities from photo-induced Hall current measurements in directions parallel and perpendicular to the polar *c*-axis were calculated as 4 and 1.3 $cm^2/V \cdot s$, respectively.[167] Polaron hopping was also identified in research on Ce-doped SBN61 single crystals, where the electron mobility was calculated as 2.7 $cm^2/V \cdot s$ at 300 K.[168]

From a simple graphical analysis of the data shown in Figure 6.9 (i.e., a comparison of correlation coefficients obtained from the fitting), it is rather difficult to determine whether the nature of SPH is adiabatic or non-adiabatic. Therefore, further investigation of the small polaron models is necessary. For an *n*-type semiconductor with a range of localized states near the conduction band edge, the hopping mobility (μ_{hop}) may be written as:[120]

$$\mu_{hop} = P\left[\left(\frac{qa_p^2 v_{ph}}{k_B T}\right)\exp\left(-\frac{w}{k_B T}\right)\right] \tag{6.6}$$

where a_p is the polaron hopping distance, v_{ph} is the optical phonon frequency, w is the activation energy associated with mobility, and P is the probability that an electron will follow the motion of the lattice in order to hop. As reported by D. Emin, P is approximately unity for adiabatic jumps and much less than 1 for non-adiabatic hopping.[169,170] In fact, the probability parameter introduces an additional temperature dependence for the non-adiabatic case, which in turn causes the pre-exponential in Eq. (6.6) to vary with $T^{-3/2}$ rather than T^{-1}.[171] Due to the nature of electron-phonon interactions, mobilities on the order of 0.1 – 1.0 $cm^2/V \cdot s$ (as observed in the Hall measurement

results described earlier) are expected for polaron hopping. Consequently, a calculated pre-exponential factor that is ~0.1 – 1.0 $cm^2/V \cdot s$ is a good indication of adiabatic hopping, as this implies that $P \sim 1$. Since the conduction mechanism is nearest neighbor small polaron hopping, (regardless of whether it be adiabatic or non-adiabatic), the polaron hopping distance (a_p) can be approximated as the distance between Nb cations (or twice the Nb-O distance), which from previous XRD studies has been determined as ~3.94 Å for SBN48.[150] For the optical phonon frequency, substitution of the Debye temperature (Θ_D = 468 K from earlier work)[103] into the expression $\nu_{ph} = k_B\Theta_D/h$, where h is Planck's constant, yields a value of 9.75×10^{12} s^{-1}.[172] Ultimately, the pre-exponential factor in Eq. (6.6) was calculated as 0.44 $cm^2/V \cdot s$, signaling that the small polaron hopping behavior of SBN above room temperature could be adiabatic.

It is well known that for systems in which small polaron hopping is observed, strong electron-phonon coupling results in a thermally-activated jump rate above some fraction of the Debye temperature (typically ~$\Theta_D/2$).[173] However, below ~$\Theta_D/2$ there is a lack of high-energy phonon modes available and thus, the temperature dependence of the electrical conductivity should change. In particular, charge transport at sufficiently low temperatures may be modeled according to Mott's variable range hopping (VRH) expression [see Eq. (2.17)].[174,175] Given the strong evidence for small polaron behavior in region I of Figure 6.8, the low-temperature electrical conductivity of reduced SBN50 was examined.

Shown in Figure 6.10(a) is a plot of $\ln(\sigma T)$ vs $10^3/T$ generated from electrical conductivity data obtained over a temperature range of 105 – 300 K; an SBN50 specimen reduced at 1000 °C for 25 h in N_2/H_2 was used for the tests. Excellent fits to the adiabatic SPH model were observed from room temperature down to ~230 K [solid line in Figure 6.10(a)]. However, attempts to fit the data below 230 K were less successful, as the correlation coefficients rapidly diverged from unity.

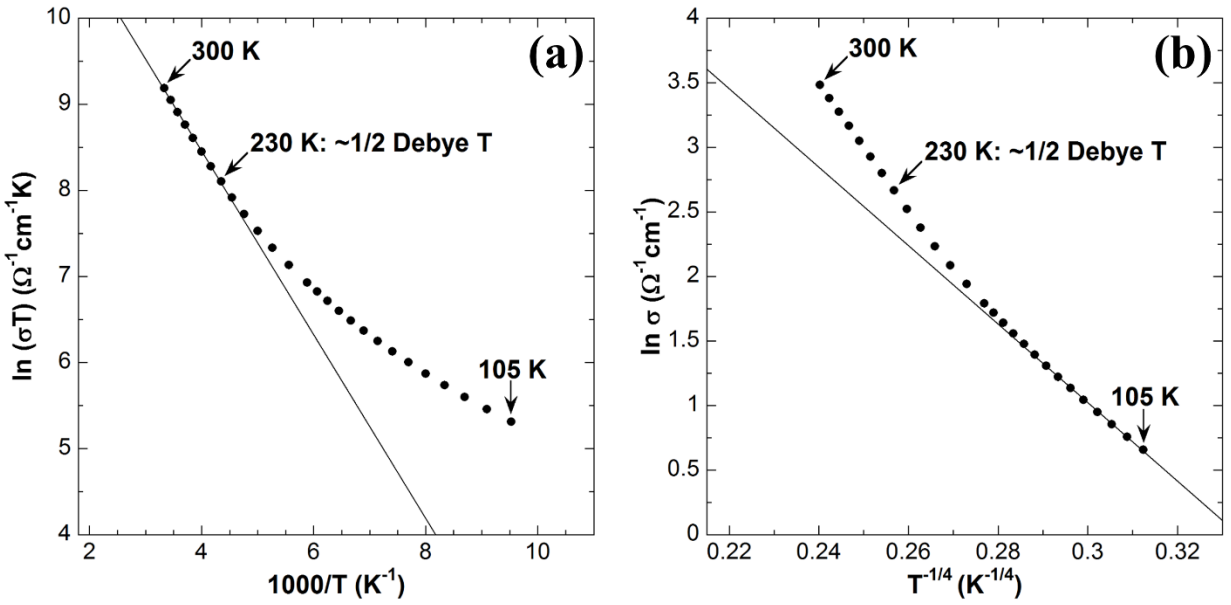

Figure 6.10. Plots of (a) ln(σT) vs $10^3/T$ (SPH model) and (b) lnσ vs. $T^{-1/4}$ (VRH model) from 105 to 300 K for SBN50 reduced at 1000 °C for 25 h in N_2/H_2. The lines in (a) and (b) were generated by fitting data from 230 – 300 K and 105 – 150 K, respectively.

Such a scenario indicates a possible change in the temperature dependence of the electrical conductivity around $\Theta_D/2$, which may be approximated as ~234 K from previous research.[103] Therefore, the low-temperature σ data were also fitted with a three dimensional [i.e., d = 3 in Eq. (2.17)] variable range hopping expression; the results are presented in Figure 6.10(b). Here, very good fits were obtained from 105 K to ~150 K, while at higher temperatures the correlation coefficients once again began to diverge from unity. Thus, it appears that the electrical conductivity of highly reduced SBN50 displays a $\exp(-T_0/T)^{-1/4}$ temperature dependence at low temperatures up to ~$\Theta_D/2$, followed by a transition to SPH behavior at higher temperatures. It should be noted that the underlying mechanisms responsible for the temperature dependence of σ above 100 K has been a source of considerable debate. In particular, Emin has noted that the single-phonon jump rate approximations of Miller and Abraham are often employed to justify an extension of Mott's VRH work to temperatures above 100 K.[176,177] While such assumptions are reportedly valid for the specific conditions of hopping between impurity states at liquid helium temperatures (~4 K), they

may not be applicable when describing charge transport among elemental states at elevated temperatures. Instead, Emin proposed a multi-phonon process where the temperature dependence of the jump rate resembles that of VRH behavior from liquid helium temperatures to $\Theta_D/2$.

Additional information on the nature of localized charge transport in reduced SBN may be gleaned from the fitting parameters in Figure 6.10(b). Referring to Eq. (2.17), the characteristic temperature coefficient, T_0, represents the slope of the $\ln\sigma$ vs. $T^{-1/4}$ plot; it may be expressed as:

$$T_0 = \frac{18\alpha^3}{k_B N(E_F)} \tag{6.7}$$

where $N(E_F)$ is the density of localized states at the Fermi level and α is the inverse of the localization length. In previous research on single crystalline SBN55, the density of localized states obtained from low-temperature (10 K) heat capacity measurements was found to be ~7.4×10^{26} $eV \cdot m^3$.[178] From this information and the slope of the VRH plot, the localization length can be estimated. In the context of this work, α^{-1} can be defined as the electron wave decay length for a localized state in a disordered system.[179,180] By rearranging Eq. (6.7), the localization length was estimated to be 6.4 Å, which is comparable to values obtained for doped $CaMnO_3$ (6.2 – 6.3 Å).[119] According to Sun *et al.*, localization lengths on this scale are consistent with VRH arising from Anderson localization, which will be discussed later in this section.[119]

Upon calculating the localization length, the temperature-dependent hopping distance (R_{hop}) and average hopping energy (W_{hop}) may be determined from the following expressions:[166,172]

$$R_{hop} = \left[\frac{9}{8\pi N(E_F)\alpha k_B T} \right]^{1/4} \tag{6.8}$$

$$W_{hop} = \frac{3}{4\pi R_{hop}^3 N(E_F)} \tag{6.9}$$

Here, R_{hop} and W_{hop} at 105 K were calculated as 2.4 nm and 23 meV, respectively. These values are comparable to those derived in earlier work. In research on TiO_2 thin films, R_{hop} and W_{hop} were found to be 2.31 nm and 29.9 meV at 225 K, respectively.[166]

Thus far, we have identified possible VRH behavior in reduced SBN50 at temperatures below $\Theta_D/2$, followed by a transition to SPH from ~230 K to approximately 550 – 600 K. To formulate a more complete scenario of charge transport in reduced SBN, the mechanism responsible for the transition to a metallic-like temperature dependence ($d\sigma/dT < 0$) in region II of Figure 6.8(a) must be elucidated. A good starting point for this discussion is the concept of disorder and how it relates to the SBN system. Even in its unreduced state, the SBN structure itself is highly disordered, with oxygen vacancies distributed randomly among tetragonal A1 and pentagonal A2 lattice sites. It is believed that these oxygen vacancies at alkaline cation positions contribute to the evolution of random and localized electric fields that act to stabilize dipoles on the nanoscale.[96,181] The resulting polarized nanoregions act as an additional source of disorder in SBN, promoting both relaxor characteristics and an inherently low thermal conductivity due to enhanced phonon scattering at domain boundaries. Reduction annealing also serves to enhance the disorder in SBN ceramics via the introduction of point defects (i.e., oxygen vacancies). Considering all of these factors, the next logical step is explore the possibility that disorder may play a significant role in the change in sign of $d\sigma/dT$ at elevated temperatures. It is from this perspective that the concept of Anderson localization must be introduced.

There are two well-known phenomena associated with charge localization and a subsequent change in the electrical conductivity of a material from one form to another. The first is related to electron-electron interactions (correlation) where, according to Mott, a metal-insulator transition occurs if the electron interaction energy exceeds the Fermi energy.[182] A second path to localization was proposed by Philip Anderson and involves the influence of disorder on electron diffusion characteristics.[183] It is this latter mechanism that will form the basis of the current discussion on the electrical behavior of reduced SBN. From an elementary standpoint, the presence of randomly distributed vacancies and structural distortions in materials such as SBN can have a profound impact on the overlap of atomic orbitals.[184] This in turn can lead to significant alterations of both the band structure and the electrical conductivity over different temperature regimes.

To examine the role of disorder on electron transport, Anderson studied the effects of a random potential superimposed on a periodic potential. Shown in Figure 6.11(a) is a one-dimensional representation of a potential well array with a lattice spacing (a) when no random potential is present. In the tight-binding approximation, such periodicity is associated with electron delocalization within a relatively narrow bandwidth (B), as displayed by the density of states function to the right of the figure.[185] However, in the disordered system illustrated in Figure 6.11(b), the lattice spacing stays more or less the same, while the depth of the potential wells is altered by a random potential with a mean of U_0. At a particular ratio of U_0/B, a transition from delocalized to localized electron transport occurs: this is referred to as an Anderson transition. The presence of a random potential arising from disorder leads to an extended density of states function with characteristic "tails" at its edges. One of the key concepts related to Anderson localization and its effect on the electrical conductivity is the notion of a mobility edge that separates localized and extended states. For a given n-type material with a certain degree of disorder, electrons will

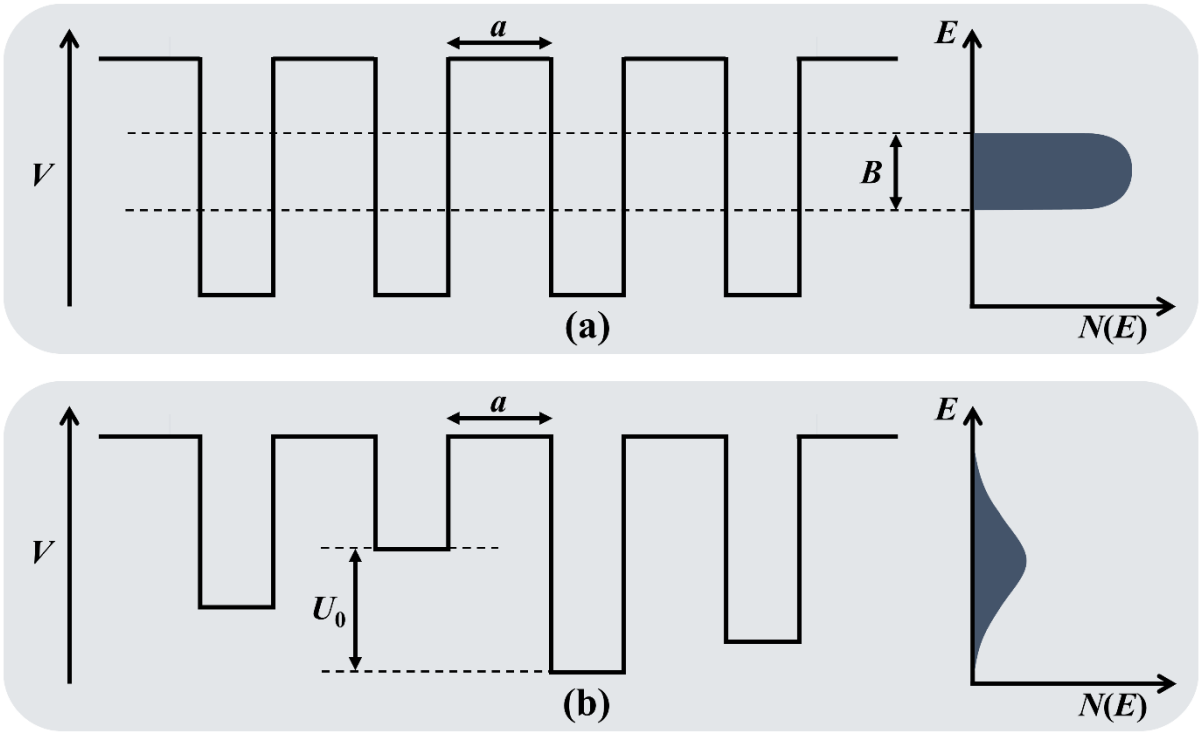

Figure 6.11. An array of potential wells with (a) no random potential and a bandwidth of B and (b) a disorder-induced random potential with mean U_0. The lattice spacing a remains unchanged, but disorder induces broadening of the density of states (right). Figure was redrawn from the work of Mott.[186]

be localized if the energy of the mobility edge, E_c, is larger than the Fermi energy (E_F). Electronic conduction may then proceed via hopping among localized states, as observed in this work for reduced SBN at temperatures below ~550 K.

The data obtained over the course of this study appear to support a scenario of charge transport outlined in a very recent study by Bock *et al*. for reduced polycrystalline SBN ceramics.[33] Shown in Figure 6.12 is the proposed density of states for reduced SBN. Upon annealing SBN in a reducing environment, an impurity band composed of oxygen vacancy donor states is formed between the O 2*p* valence band the Nb 4*d* conduction band. However, due to the effects of disorder, the impurity and conduction bands are sufficiently broadened in a manner consistent with Figure 6.11(b). The resulting overlap between the bands produces a pseudogap similar to that described in earlier work on amorphous semiconducting alloys by Cohen *et al*.[187] As a consequence of the

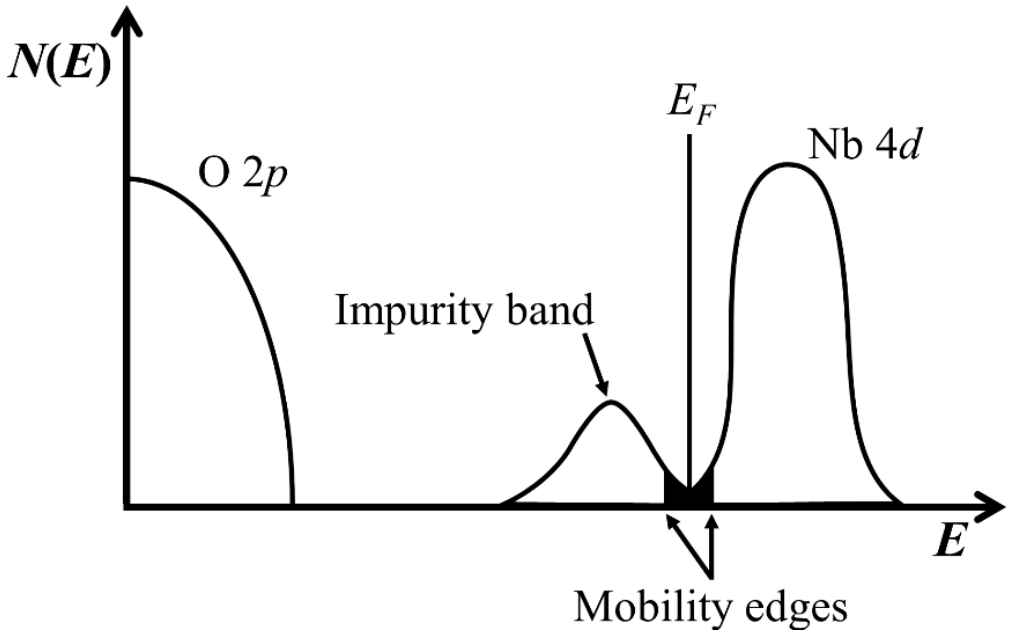

Figure 6.12. Proposed density of states for reduced SBN. An impurity band formed from oxygen vacancy donor states overlaps with the Nb 4*d* conduction band; the Fermi level resides in the pseudogap formed between the two bands. Localized states (shaded regions) are separated from free electron states by a mobility edge in the Nb 4*d* conduction band.

overlap, it is possible that a certain number of electrons in the tail of the impurity band possess a higher energy than electrons in non-bonding states at the tail of the conduction band. These impurity band electrons subsequently fall into states located in the conduction band tail, and the Fermi energy lies near the center of the psuedogap. Impurity donor states are locally neutral when occupied by electrons, while conduction band states are neutral when unoccupied. Positively-charged unoccupied states in the donor band are thus neutralized by corresponding negative charges in the conduction band tail. Within the pseudogap and in the vicinity of the Fermi level, electrons are effectively localized (shaded region of Figure 6.12). Extended (i.e., delocalized) electron states are separated from localized states by an upper mobility edge near the bottom of the Nb 4*d* conduction band. Upon heating SBN up to a certain temperature, a sufficient number of localized electrons are excited above the mobility edge into free electron states. These electrons

ultimately dominate the conductivity behavior and thus, a transition to a metallic-type temperature dependence of σ is observed.

Strong evidence for the existence of localized electron states in reduced SBN has been demonstrated through the variable range and small polaron hopping data discussed earlier. However, trends in the Seebeck coefficient can also be utilized to glean information regarding the excitation of electrons across the mobility edge into delocalized states. Referring to Eq. (6.5), if electrons in the valence band attained the necessary energy to be excited above the mobility edge and into the conduction band, then a decrease in $|S|$ may be observed at elevated temperatures due to the increase in carrier concentration. This certainly does not appear to case, as an increase in $|S|$ occurs over the entire range of testing temperatures. Alternatively, if a constant carrier concentration is maintained and localized electrons in the vicinity of E_F are promoted above the mobility edge, then $|S|$ should be proportional to the natural logarithm of T at elevated temperatures, since the density of states is proportional to $T^{3/2}$ (as discussed earlier). More specifically, a parabolic density of states function should yield a linear relationship between $|S|$ and $\ln(T)$ with a slope of 129 μV/K.[164,188] To investigate this scenario, the $|S|$ data in Figure 6.8(b) were plotted against $\ln(T)$; the results are displayed in Figure 6.13(a). As evident in the graph, a good linear fit to the data was observed over a temperature range of 615 – 955 K. Inspection of the electrical conductivity findings in Figure 6.8(a) reveals that it is over this same temperature region that the value of $d\sigma/dT$ significantly decreases and even becomes negative. Excellent linear fits were also obtained above ~615 K for an SBN61 single crystal reduced for 25 h, as shown in Figure 6.13(b). Furthermore, the slopes of both linear fits in Figure 6.13 were approximately 103 μV/K, indicating that the density of states functions for the polycrystalline SBN50 and single crystal SBN61 samples are quite similar. The deviation in the values of the slopes from 129 μV/K is likely

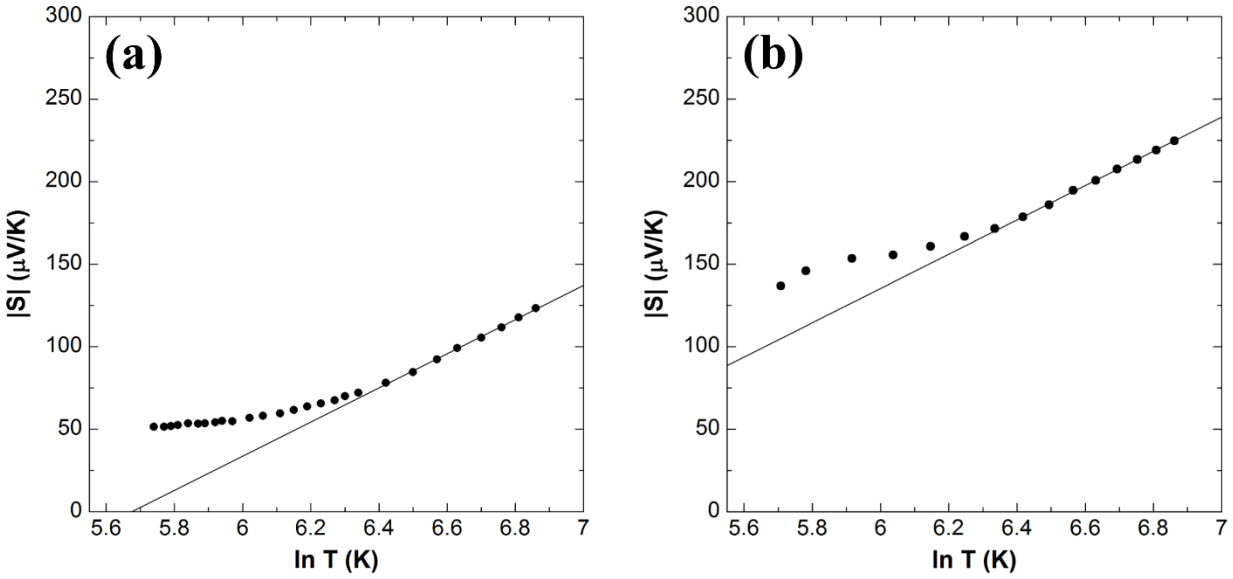

Figure 6.13. Plots of |*S*| vs. ln(*T*) for (a) polycrystalline SBN50 and (b) single crystalline SBN61; both samples were reduced for 25 h. Excellent linear fits to the data were obtained from 615 – 955 K.

the result of reduced SBN ceramics possessing a more complex electronic structure with density of states functions that are not perfectly parabolic. Regardless, the linear nature of the |*S*| vs. ln(*T*) plots at elevated temperatures supports the notion that a change in $d\sigma/dT$ arises due to the excitation of localized electrons across a mobility edge and into extended states at higher *T*.

Given the trends discussed above, valence band photoemission data previously obtained for reduced SBN50 specimens were revisited. Shown in Figure 6.14 are the XPS spectra acquired from polycrystalline SBN50 reduced for 1 and 25 h. Both samples show photoemission from O 2*p* valence states over a binding energy range of ~4 – 10 eV. However, an additional peak centered at a binding energy of approximately 1.5 eV appears within the band gap for the SBN specimen reduced for 25 h. While no definitive conclusions can yet be made, it is possible that this smaller peak corresponds to photoemission from the impurity band shown in the schematic of Figure 6.12.

The results outlined in this section shed light on a particular dilemma related to the TE properties of reduced SBN. Namely, the inherent disorder associated with SBN ceramics has the desirable effect of lowering the thermal conductivity via enhanced phonon scattering. However,

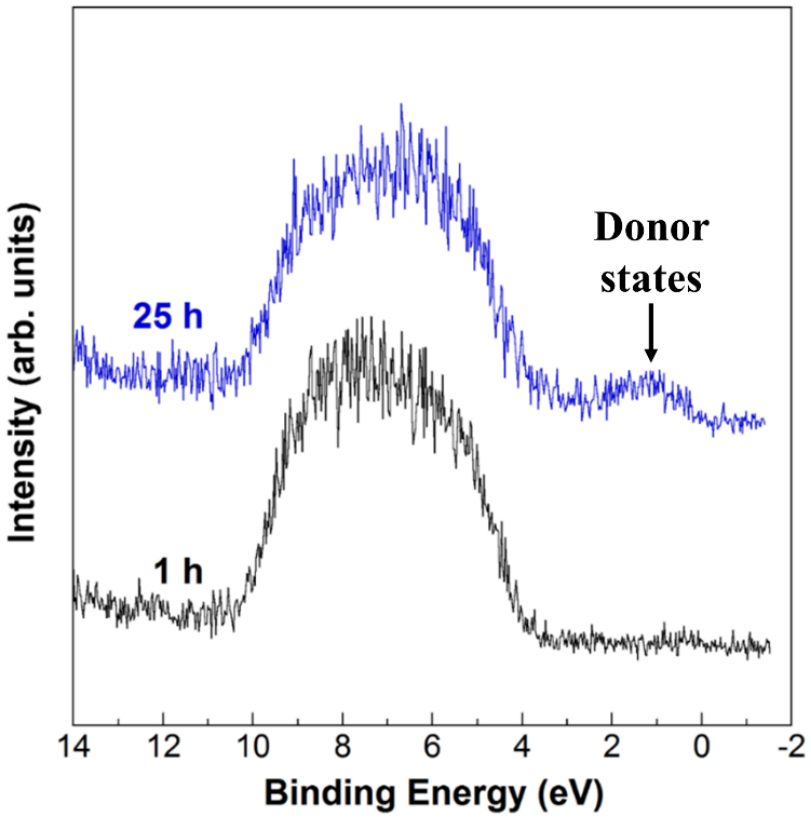

Figure 6.14. XPS data obtained for SBN50 specimens reduced for 1 and 25 h. The appearance of a peak centered around 1.5 eV in the 25 h sample may be due to photoemission from the impurity band described in Figure 6.12.

the same disorder suppresses the electron mobility and thus, reduces the electrical conductivity even after long reduction durations. It then becomes apparent that a new strategy must be employed to enhance the TE performance of reduced SBN. With this in mind, preliminary research into the use of pore formers to produce favorable microstructures will now be discussed.

6.5. Effect of pore formers

Given the findings detailed in the previous section, preliminary experiments involving the use of pore formers were devised with two primary objectives in mind: 1) suppressing κ_l by hindering phonon propagation and 2) maintaining previously measured values of the power factor by avoiding large decreases in the electronic mobility. Under optimized processing conditions, the

pores should be distributed homogeneously so that a coherent pathway for electrical conduction exists. In this work, polymethylmethacrylate (PMMA) with a mean particle diameter of ~160 nm was selected as the pore forming agent based on promising results reported by Ohtaki *et al*. for Al-doped ZnO (as discussed in Chapter 2).

Shown in Figure 6.15(a) – (c) are the respective Seebeck coefficient, electrical conductivity, and power factor values obtained for SBN50 prepared with (5 wt% PMMA) and

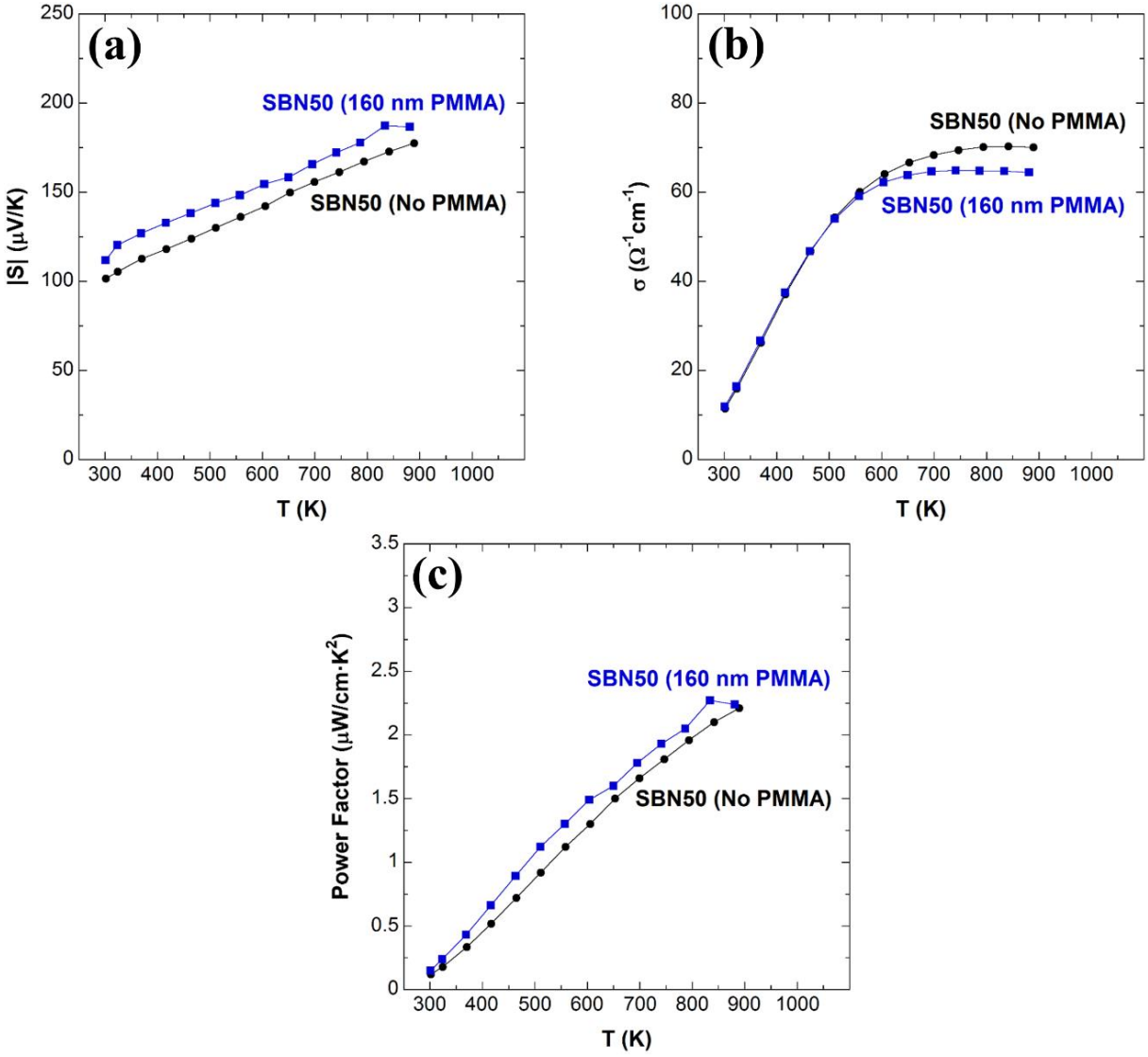

Figure 6.15. (a) Seebeck coefficient, (b) electrical conductivity, and (c) power factor obtained for reduced SBN50 with (solid blue squares) and without (solid black circles) the use of PMMA pore formers.

without PMMA pore formers; both samples were reduced for 25 h at 1000 °C. Interestingly, the magnitude of the Seebeck coefficient was increased by ~9% in the sample fabricated with PMMA, while the electrical conductivity of the two specimens was nearly identical up to ~600 K. Consequently, the power factor from room temperature to ~600 K was, on average, approximately 24% higher for the specimen processed with PMMA.

To further investigate the effect of pore forming agents on TE performance, thermal conductivity data was obtained for the samples in Figure 6.15; the results are shown in Figure 6.16(a). A significant reduction in κ by an average of ~44% was observed for the sample processed with PMMA pore formers. The glass-like thermal conductivity of SBN has been noted in previous research and is attributed to both polarized nanoregions and the random distribution of vacancies at alkaline cation sites.[29,103,153] In fact, phonon mean free paths of ~5 Å, on the order of the SBN unit cell (a = 12.484 Å, c =3.957 Å for SBN48)[150] have been reported for SBN48 single crystals at 300 K.[103] The overall increase in κ with temperature for both specimens may be due in some part to the gradual elimination of polarized nanoregions as the Burns temperature is approached.

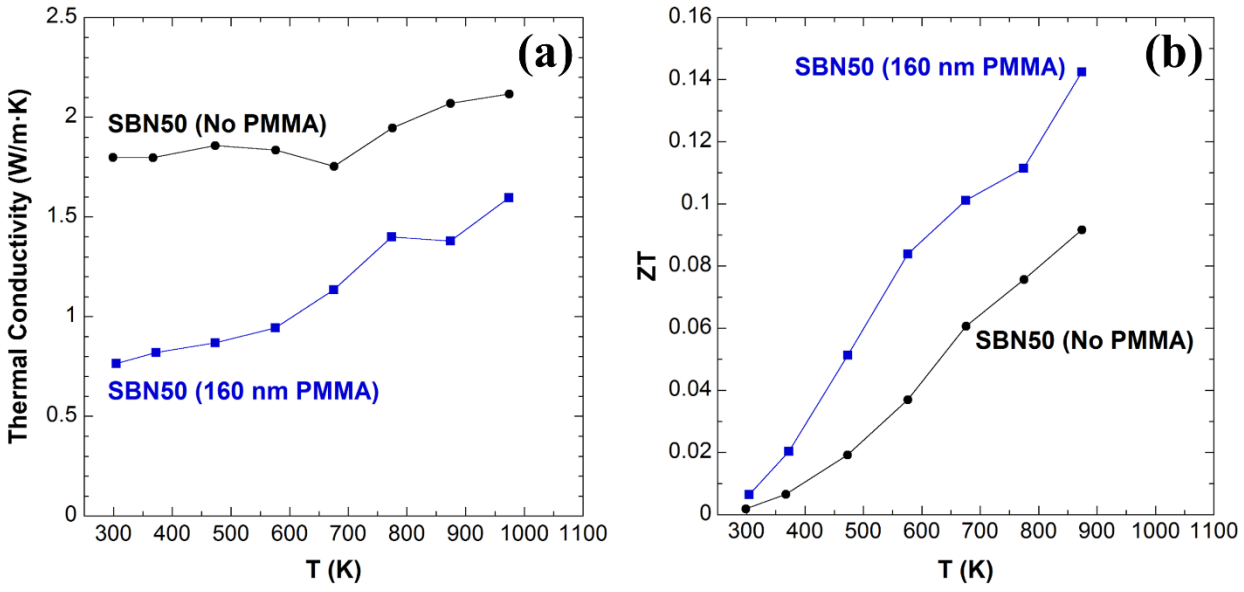

Figure 6.16. (a) Thermal conductivity and (b) *ZT* obtained for reduced SBN50 processed with (solid blue squares) and without (solid black circles) PMMA pore formers.

Regardless, the sizable reduction in κ achieved through the use of pore formers led to a substantial increase in *ZT*, as illustrated in Figure 6.16(b). When compared to the conventionally prepared SBN50 sample, the specimen processed with PMMA exhibited a ~182% increase in *ZT* from 300 to 575 K and an average increase of ~128% over the entire temperature range.

Given the observed increase in $|S|$ and reduction in κ with the introduction of PMMA, the morphology of the tested samples was examined. Shown in Figure 6.17(a)-(b) and (c)-(d) are SEM images obtained for SBN50 prepared with and without PMMA, respectively. The vaporization of PMMA during sintering led to the evolution of a large number of pores with various sizes. While it is unclear whether these pores served to increase $|S|$ via electron energy filtering, it is likely that

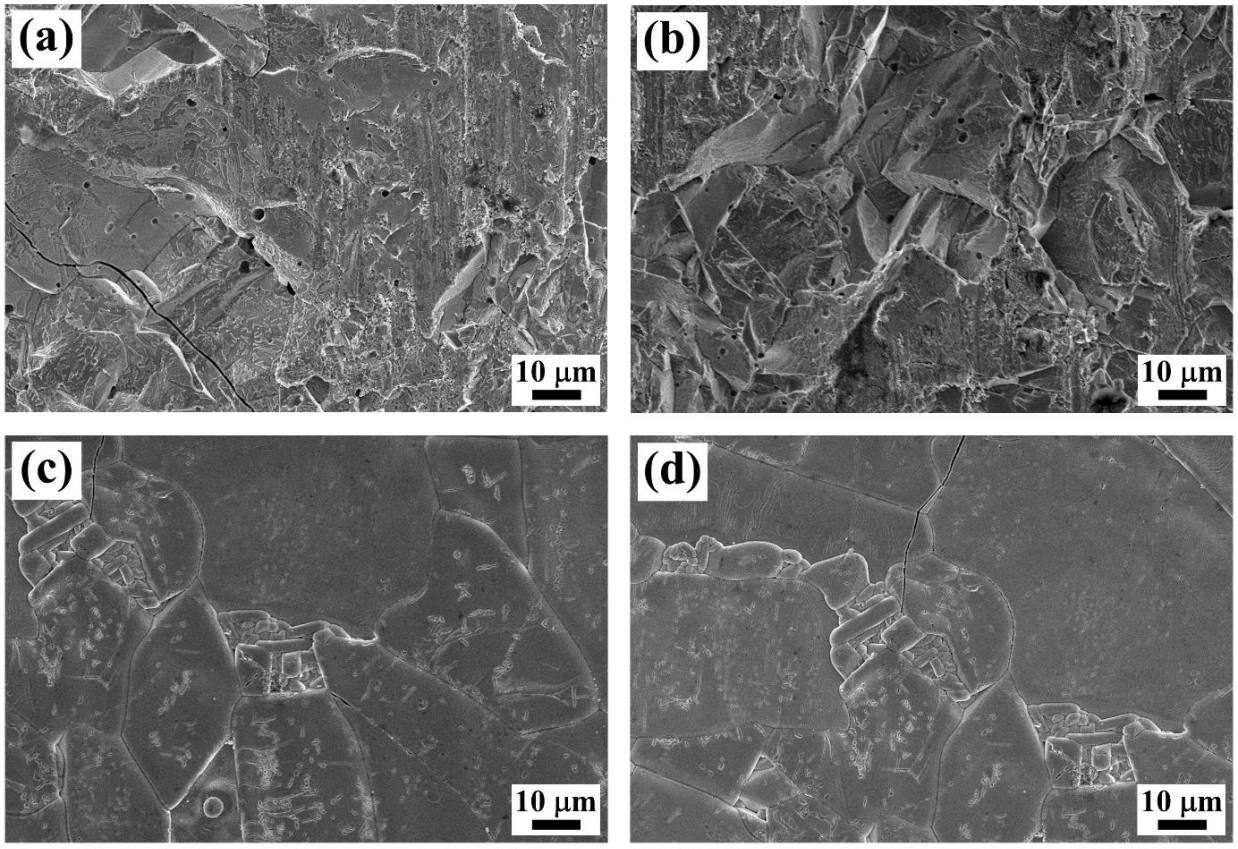

Figure 6.17. SEM images obtained at different locations for SBN50 prepared (a)-(b) with PMMA and (c)-(d) no PMMA. Numerous pores with different sizes are evident (a)-(b) due to the vaporization of PMMA during sintering.

the random pore distribution serves to scatter phonons with a range of different wavelengths, leading to a significant decrease in κ. Indeed, when compared to SBN50 prepared with no PMMA, an almost 60% decrease in the thermal diffusivity (K) was measured at 300 K for the specimen prepared with 5 wt% PMMA. Since $\kappa = C_p K \rho$, where C_p is the heat capacity and ρ is the density, the overall value of κ would also be reduced. While the heat capacity (C_p) of both specimens was calculated according to the relation $3R/A_w$ (where R is the universal gas constant and A_w is the average atomic weight), composition was not varied here and thus, measurements of C_p obtained via differential scanning calorimetry should not exhibit an appreciable change. One rather surprising result was that no considerable disparity in the relative density (ρ_{rel}) of the samples was observed. On the contrary, the relative density of the sample prepared with PMMA was found to be slightly higher (ρ_{rel} = 94.9%) than the specimen fabricated with no PMMA (ρ_{rel} = 92.8%).

From the results detailed in this section, it appears that the use of pore formers is an effective strategy to enhance the TE properties of reduced SBN ceramics. However, as noted in Chapter 2, one particular disadvantage of certain *n*-type TE oxide systems is their tendency to oxidize in air at elevated temperatures. Therefore, in the final section of this chapter, our findings related to the stability of reduced SBN will be discussed.

6.6. Stability of reduced SBN

As stated in Chapter 2, oxidation is major issue that limits the environment in which reduced *n*-type thermoelectrics may be able to function effectively. Therefore, in *n*-type oxide systems where reduction annealing is the primary mechanism to increase σ, it is imperative that an analysis of the oxidation characteristics be conducted. To this end, an investigation into the thermal stability of reduced SBN50 was carried out. As an initial experiment, loose SBN50 powder was

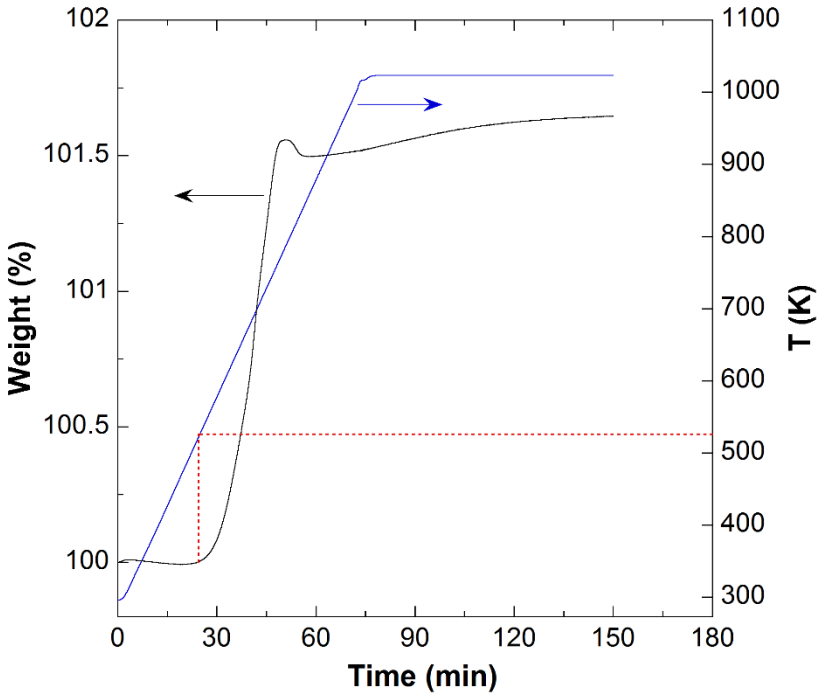

Figure 6.18. Weight gain and temperature profile for SBN50 powder reduced for 5 h in N_2/H_2(5%).

first reduced in N_2/H_2(5%) at 1000 °C for 5 h. Thermogravimetric analysis (TGA) was then carried out to elucidate the oxidation kinetics. The results of the TGA measurements are presented in Figure 6.18. During heating in air, the overall mass of the powder sample increased by approximately 1.5%. Furthermore, the apparent onset of rapid oxidation during heating occurred at a temperature of approximately 525 K (~250 °C).

To evaluate the effects of repeated thermal cycling in a low-pressure inert environment, the SBN50 sample used to generate the data in Figure 6.8 was subject to two follow-up TE tests. Shown in Figure 6.19(a) are the original electrical conductivity results (black circles) along with the data acquired during the second (blue squares) and third (red diamonds) follow-up tests; the σ values obtained during heating are denoted with filled markers, while those measured during cooling are represented by open markers. It is apparent from the figure that, upon cooling from the peak testing temperature, a significant reduction in σ is observed during the initial test run. For the second test, the electrical conductivity obtained when heating initially appears to coincide with

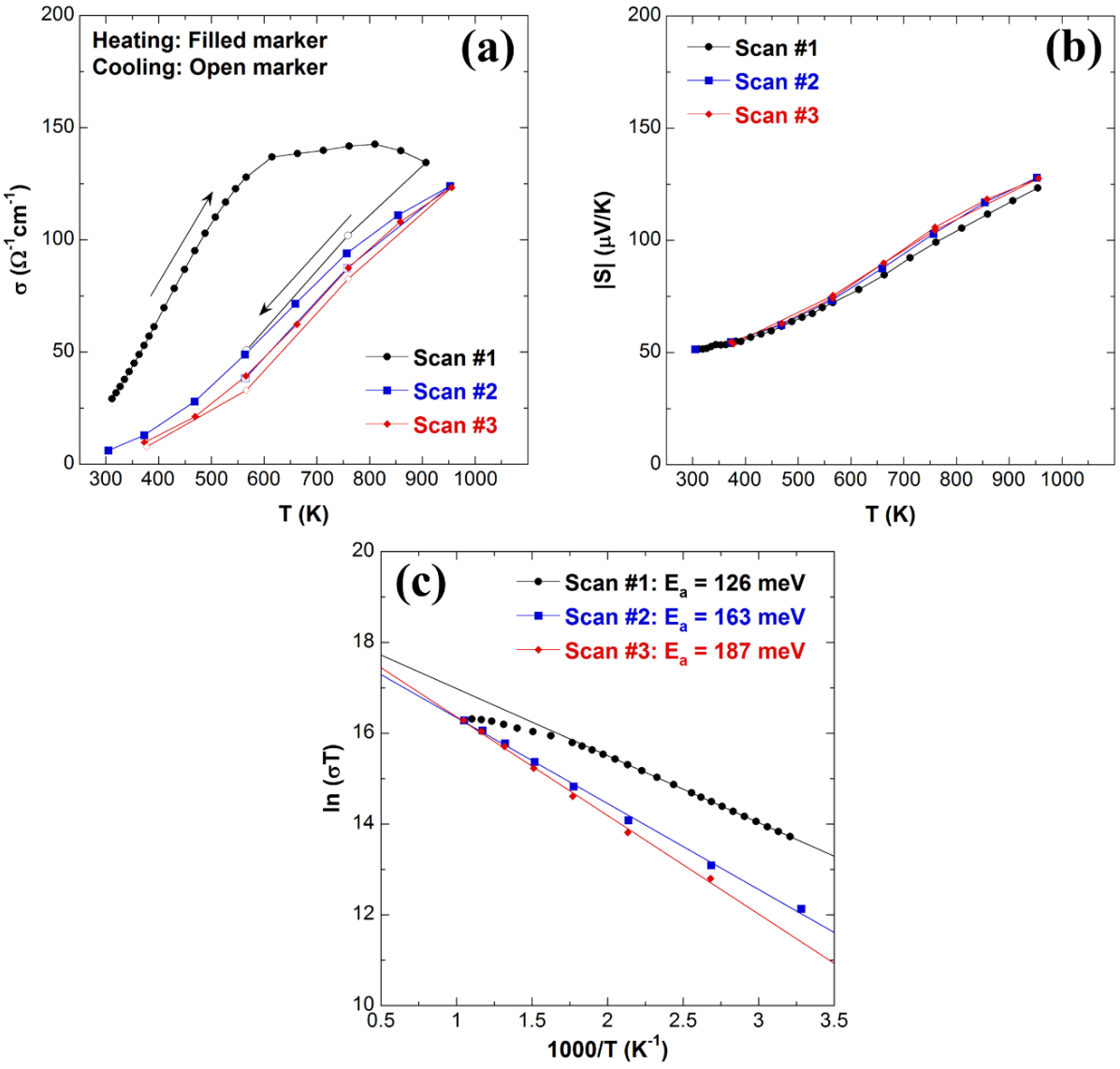

Figure 6.19. (a) Electrical conductivity of the sample in Figure 6.8 during the initial (black circles), second (blue squares), and third (red diamonds) TE tests; the σ values obtained during heating are denoted with filled markers, while those measured during cooling are represented by open markers. (b) Seebeck coefficients obtained for the samples in (a) during heating. (c) Plot of $\ln(\sigma T)$ vs. $10^3/T$ generated with σ data from (a); only the results from the heating portion of the tests are shown.

that measured during the cooling portion of the first test, but then diverges from the latter and shows lower values after 550 K. Furthermore, the average percent decrease in σ upon cooling during the second test is significantly lower (14.4%) than that in the first test (44.2%). For the third and final test, the σ values measured during heating are nearly identical to those obtained over the

cooling cycle of the second test at all testing temperatures, while the percent decrease in σ is slightly smaller (13.7%).

There are a few possible scenarios that may explain the observed decreases in the electrical conductivity during testing. Firstly, slight oxidation of the samples cannot be ruled out, as a small increase in $|S|$ was observed after the initial TE test [Figure 6.19(b)]. An uptake of oxygen would serve to reduce the carrier concentration and increase $|S|$ according to Eq. (6.5). An additional mechanism that could be partially responsible for the trend in σ is grain boundary passivation as a result of annealing in an oxygen-deficient environment containing hydrogen.[190] During the reduction of SBN specimens in N_2/H_2, it is possible that dangling bonds at grain boundaries, which would serve as traps for electrons, are passivated by hydrogen atoms, resulting in an increase of the electron mobility. However, when a TE test is initially conducted, hydrogen gas is driven out of the material at the grain boundaries as the temperature is raised, thereby exposing traps that hinder electron transport. Such a scenario, along with slight oxidation, may explain the data shown in Figure 6.19(c), where an increase in the polaron hopping activation energy is observed with subsequent testing.

In an attempt to identify the temperature at which the electrical conductivity degrades during cycling, an SBN50 specimen reduced at 1000 °C for 25 h in N_2/H_2 was heated to, and cooled from 460, 560, 660, and 770 K during testing; the resulting electrical conductivity and Seebeck coefficient values are shown in Figure 6.20(a) and (b), respectively. No significant changes in σ are observed upon heating to 460 and 560 K. However, when the sample was heated to 660 K and then cooled, a noticeable change in the electrical conductivity was evident. Subsequent heating up to 760 K led to even larger decreases in σ upon cooling. In contrast, the Seebeck coefficient exhibited little change or even a slight decrease during the cooling cycles.

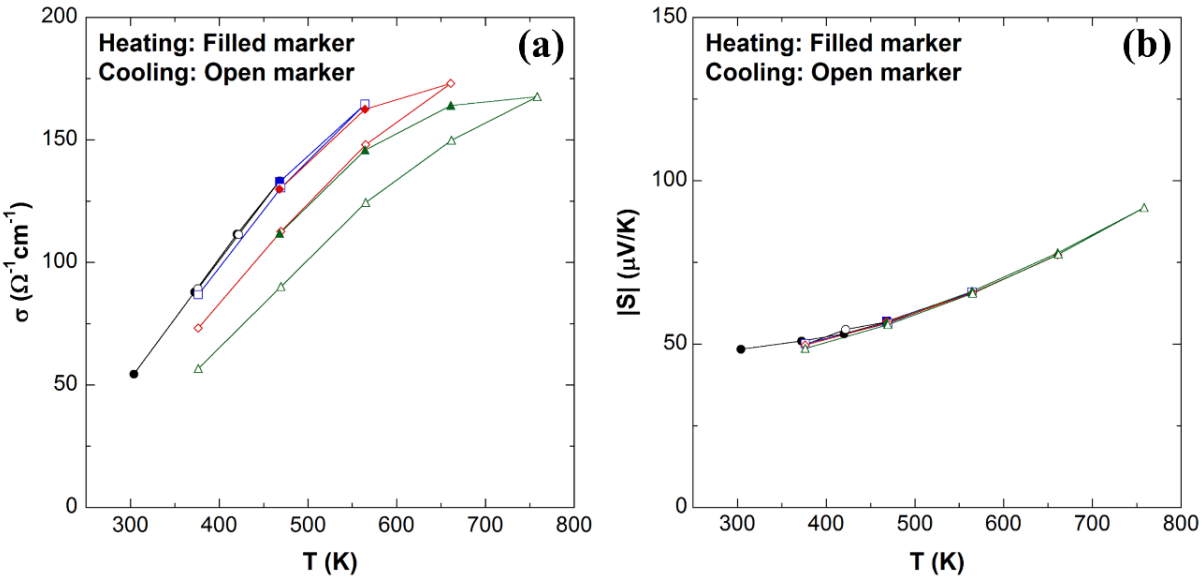

Figure 6.20. (a) Electrical conductivity and (b) Seebeck coefficient obtained for an SBN50 sample reduced at 1000 °C for 25 h in N_2/H_2; values were obtained as the specimen was heating to and cooled from 460, 560, 660, and 770 K.

Chapter 7. Conclusions

7.1. Summary of research findings

In this work, the defect structure, charge transport mechanisms, and TE behavior of the *n*-type relaxor ferroelectric $Sr_xBa_{1-x}Nb_2O_6$ (SBN100*x*) were explored. A highly efficient and simple solution combustion synthesis (SCS) route was first formulated to fabricate SBN nanoparticles. X-ray diffraction (XRD) patterns confirmed that ultrafine, phase-pure SBN powders with a range of different Sr:Ba ratios were produced by the devised SCS method. The ability to synthesize single-phase SBN with different compositions allowed for a reliable study of site occupancy in the complex and disordered tetragonal tungsten bronze SBN lattice. Furthermore, the use of reduction annealing to produce electrically conductive, oxygen-deficient SBN specimens enabled an examination of both the defect structure and charge transport behavior.

X-ray photoelectron spectroscopy (XPS) analysis was employed to evaluate both cation site occupancy in unreduced $Sr_xBa_{1-x}Nb_2O_6$ compositions (x = 0.2, 0.3, 0.5, and 0.61) and local binding states in reduced SBN50. The higher binding energy component of Sr $3d_{5/2}$ photoemission was associated with Sr cations at A2 sites in the TTB lattice, presumably due to increased coordination by oxygen atoms at this location. Upon reducing SBN50 in both Ar/H_2 and N_2/H_2 environments, a change in emission intensity towards lower valence was noted in the Nb 3*d* XPS spectra. Such a finding is consistent with the notion that the increased electrical conductivity (σ) of reduced SBN is the result of evolved oxygen donating electrons back to the transition metal cation. Interestingly, a shift in both the Sr-A2 and Ba $3d_{5/2}$ components to lower binding energy was observed as the reduction time was increased, supporting a scenario of preferential oxygen vacancy formation adjacent to A2 sites.

Using SBN50 as a representative composition, the TE characteristics of specimens reduced at temperatures of 900 – 1150 °C were explored. A peak power factor ($S^2\sigma$, where S is the Seebeck coefficient) of 1.78 μW/cm·K^2 was ultimately obtained after a 1000 °C reduction heat treatment. An analysis of the Nb 3*d* XPS spectra, conducted after subtracting out the Nb^{5+} photoemission data, revealed the growth of two lower valence Nb peaks at different binding energies as the reduction temperature was increased. Upon further examination of these lower valence peaks, it was found that intensity ratio of the higher binding energy peak to lower binding energy peak was maximum for the specimen reduced at 1000 °C, indicating that XPS may be used as tool for optimizing the reduction conditions. Furthermore, the alteration of the reduction temperature allowed for a determination of the oxygen vacancy formation enthalpy, which was subsequently estimated to be ~3.85 eV at 300 K. The room temperature thermal conductivity (κ) of SBN50 was also found to be quite low, as κ values of 1.03 and 1.46 W/m·K were obtained for the material in its as-sintered state and after reduction at 1000 °C, respectively.

At a fixed temperature of 1000 °C, SBN50 specimens were reduced for different time durations, and the resulting TE properties were investigated. A peak power factor of 3.1 uW/cm·K^2 was measured at ~950 K for SBN50 reduced for 25 h. Moreover, an interesting trend in σ, which was also detected for the samples reduced at different temperatures, was continually observed. Specifically, the electrical conductivity initially exhibits a temperature dependence consistent with that of a conventional *n*-type semiconductor, i.e., $d\sigma/dT > 0$. However, as the testing temperature is increased above ~600 K, the electrical conductivity presents a more metallic-like temperature dependence with negative $d\sigma/dT$ values. While a transition in the temperature dependence of σ was noted, the values of $|S|$ showed a consistent increase over the entire range of testing temperatures.

Such a finding pointed to the possibility that the carrier concentration remains relatively constant during testing, while a change in the electron mobility occurs at elevated temperatures.

In previous work by other research groups, it was proposed that the observed trends in $d\sigma/dT$ were the result of polarized nanoregions (PNRs) hindering the mass percolation of electrons up to the Burns temperature (T_B, ~625 K for SBN), at which point the PNRs are eliminated. To test this hypothesis, a polycrystalline specimen of $Ca_{0.18}Ba_{0.82}Nb_2O_6$ (CBN18), which is isostructural to SBN but has a much higher T_B, was reduced under conditions identical to those employed for SBN50. A comparison of the TE properties measured for CBN18 and SBN50 revealed that the $d\sigma/dT$ transition in the former occurred at a temperature approximately 100 K lower that in SBN50, thereby casting doubt on the notion that PNRs are primarily responsible the inhibition of metallic-like electrical conduction behavior.

In an attempt to elucidate the mechanisms of charge transport in reduced SBN, additional electrical conductivity data were acquired over different temperature regimes for SBN50 reduced at 1000 °C for 25 h. For temperatures in the range of 105 – 150 K, a $\exp(-T_0/T)^{-1/4}$ dependence of σ was observed. Such behavior indicates the possibility of polaronic conduction via the variable range hopping (VRH) mechanism at low temperatures. From linear fitting of the low temperature results, a localization length of 6.4 Å, consistent with VRH due to Anderson localization, was calculated. At temperatures of ~160 to 220 K, there appears to be a gradual change in the dependence of σ, consistent with theoretical calculations of a transition in the polaron transport behavior around one-half of the Debye temperature ($\Theta_D/2$ ~230 K for SBN). Electrical transport then proceeds according to the small polaron hopping (SPH) mechanism over a temperature range of approximately 230 to ~550 K. Ultimately, significant deviations from the small polaron model are observed above ~550 K, and the electrical conductivity begins to display a more metallic-like

temperature dependence, as evident by a decrease and eventual change in sign (from positive to negative) of $d\sigma/dT$.

Given both the inherent randomness of the TTB structure and the existence of PNRs in SBN ceramics, a scenario of disorder-induced electron localization (Anderson localization) was utilized to explain the charge transport behavior in reduced SBN. In particular, the random distribution of vacancies at Sr/Ba sites, combined with structural distortions and the presence of PNRs in SBN, leads to the formation of a mobility edge that separates localized and delocalized electron states. At lower temperatures (below 550 – 600 K, depending on the degree of reduction), electrical conduction proceeds via polaron hopping between localized states, with the Fermi level situated in a pseudogap formed by a donor impurity band and the Nb 4*d* conduction band. At a certain elevated temperature (~615 K for SBN50 reduced for 25 h at 1000 °C), electrons are activated above the mobility edge and the σ-T behavior resembles that of a metal in accordance with an Anderson transition. The activation of electrons from localized states around the Fermi level to extended states in the conduction band is supported by high-temperature Seebeck coefficient data showing a linear relationship between $|S|$ and ln T above 615 K.

From the results obtained over the course of this study, it became apparent that the inherent disorder associated with reduced SBN ceramics has the desirable effect of lowering κ while at the same time suppressing the electron mobility and reducing σ, even after long reduction durations. Therefore, a strategy of using pore formers was devised with the goal of suppressing κ further by inhibiting phonon transport, while maintaining previously measured values of the power factor by avoiding large decreases in the electron mobility. In subsequent experiments, an average power factor increase of ~24% was obtained from room temperature to ~600 K for an SBN sample sintered with 5 wt% polymethylmethacrylate (PMMA) as sacrificial pore former. More

importantly, when compared to SBN50 processed with no PMMA, a significant reduction in κ by an average of ~44% was observed from 300 – 800 K for the sample fabricated with pore formers. This decrease in κ, when combined with the enhancement in the power factor, produced *ZT* values that were an average of ~128% higher than those calculated for SBN50 prepared with no PMMA. At 873 K, a peak *ZT* of 0.14 was achieved through the use of PMMA, while SBN50 processed with no PMMA exhibited a maximum *ZT* of 0.09 at the same temperature.

Lastly, the thermal stability of reduced SBN was investigated. Thermogravimetric analysis (TGA) revealed that reduced SBN50 readily oxidizes in air above ~525 K (~250 °C). Moreover, the electrical conductivity of reduced SBN50 specimens was found to decrease after repeated testing in an inert (He) environment up to ~950 K, possibly due to slight re-oxidation and/or the elimination of adsorbed hydrogen at grain boundaries. Subsequent measurements performed in the same inert environment showed that heating reduced SBN50 up to ~560 K has only a minimal impact on σ, while increasing the temperature to above ~660 K leads to substantial decreases in the electrical conductivity.

7.2. Areas for future work

The results presented in this dissertation provide a basis from which further improvements in the TE performance of SBN may be achieved. It is the expectation that, if certain key areas related to SBN are adequately developed, significant advances could be made in the field of *n*-type TE oxides as a whole. Therefore, in this concluding section, promising avenues for future research will be briefly described.

As detailed throughout this dissertation, the dominant strategy of increasing the electrical conductivity of SBN is to subject the material to a high-temperature reduction annealing treatment

so as increase the carrier concentration via the introduction of oxygen vacancies. However, as discussed in Section 6.6, repeated cycles of heating and cooling leave open the possibility of re-oxidation, which could deteriorate the functionality of the SBN thermoelectrics. Packaging protocols could temporarily ameliorate this issue, but for a self-sustainable system, a more long-term solution is preferred. One way to resolve this problem may be the incorporation of suitable dopants with different charges into the SBN structure. In an ideal scenario, point defects arising from specific doping profiles would be compensated by the generation of electrons to preserve electroneutrality, thereby increasing the electrical conductivity without the need for reduction annealing. Furthermore, if sufficiently heavy dopant atoms are utilized, further decreases in κ may be attained.

Due to the inherent disorder associated with SBN, the phenomenon of electron localization must always be considered when optimizing TE performance. Even if a suitable dopant protocol is developed, it is likely that the effects of disorder and strong electron-phonon interaction in SBN will serve to hamper the electron mobility. Therefore, efforts should be focused on bolstering the power factor through an increase in $|S|$, while reducing the already low thermal conductivity of SBN even further. Given the success of the initial PMMA experiments detailed above, the research should be expanded to include a wider array of pore former compositions, concentrations, and size distributions. In addition, pore formers may be used with appropriate texturing techniques to further enhance the TE characteristics. The success of such work may be expanded so as to explore the potential of other TE oxide systems.

Appendix A. Sol-gel fabrication of SBN50

One of the advantages of the devised SCS method is that it allows phase pure SBN powder to be produced in a simple and highly efficient manner. In contrast, current sol-gel techniques designed for the fabrication of SBN nanoparticles often require centrifugation or filtering steps to create a stable niobium precursor.[129,191] Such procedures both hinder efficiency and introduce the possibility of Nb loss. Consequently, the development of a sol-gel method where SBN nanoparticles can be synthesized in one reaction vessel (i.e., a one-pot synthesis technique) would be of great interest to researchers in the field of complex ferroelectric oxides.

Considering the above issues, a one-pot sol-gel route for fabricating SBN nanoparticles was formulated based on previous work related to the synthesis of Nb_2O_5 nanoparticles.[192] A schematic of the proposed sol-gel technique is displayed in Fig. A1. Here, niobium oxalate is first

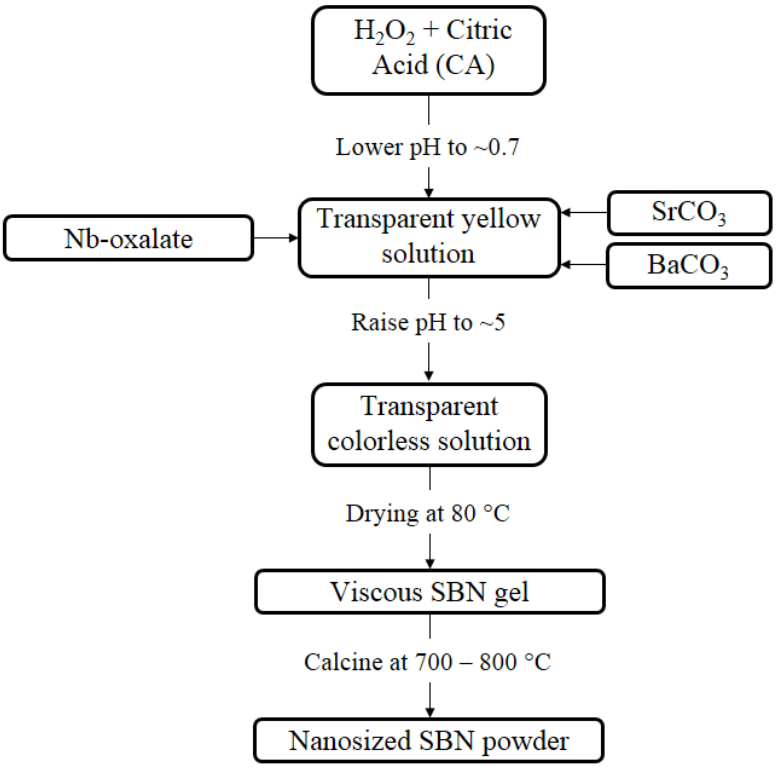

Figure A1. A schematic of the proposed sol-gel technique for fabricating SBN nanoparticles.

decomposed in a solution of hydrogen peroxide (13:1 molar ratio of H_2O_2 to oxalate) and citric acid (2:1 molar ratio of citric acid to Nb atoms). The pH of the solution is then lowered to ~0.7 via the addition of nitric acid. Sr and Ba atoms are introduced in the form of metal carbonates, which leads to the rapid evolution of CO_2. As the pH is raised to ~5, ionization of the citric acid ensues and a stable Nb peroxo-citrato complex is created. Subsequent drying of this solution at ~80 °C produces a hardened gel that, when calcined, yields SBN nanoparticles.

The XRD pattern of SBN50 powder fabricated by the devised sol-gel method and calcined at 800 °C for 2 h is presented in Fig. A2; red vertical lines denote the positions of SBN50 peaks from the powder diffraction file. All reflections in the pattern correspond to those of tetragonal tungsten bronze SBN, and no secondary phase formation is evident. TEM images were also obtained to examine the particle size of the sol-gel derived SBN50 powders. As shown in Figure A3, the SBN particles appear to be roughly spherical with a size of less than 100 nm.

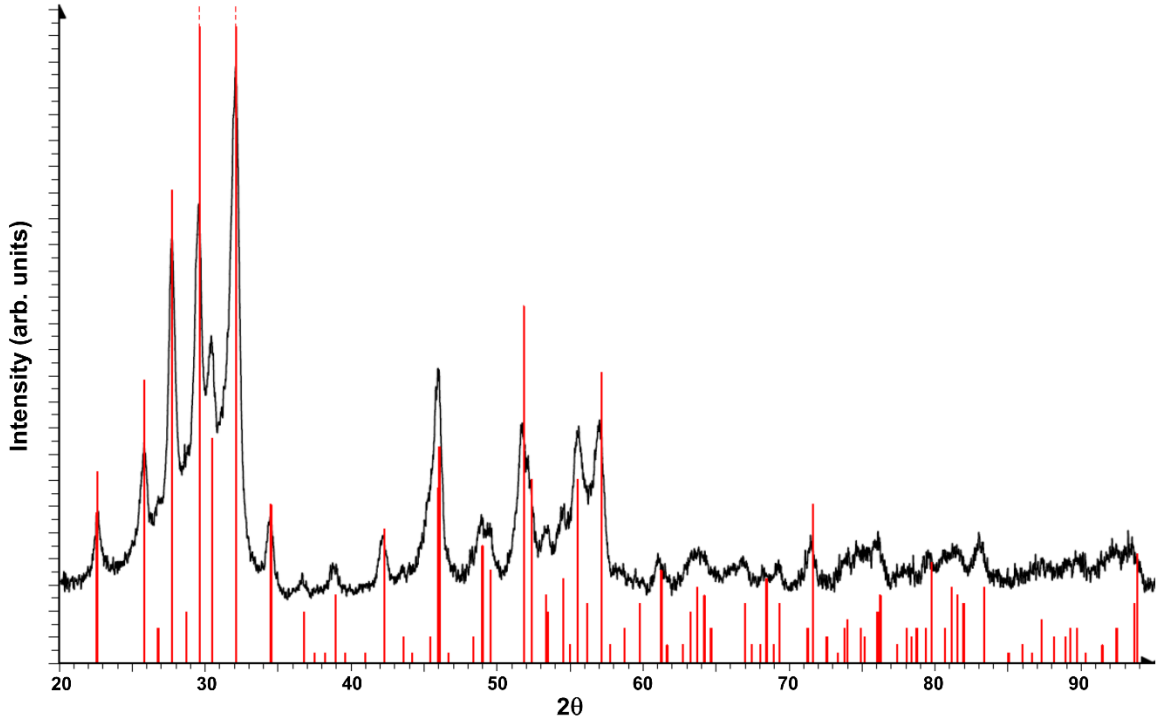

Fig. A2. XRD pattern obtained for sol-gel derived SBN50 powder calcined at 800 °C; red vertical lines denote the positions of peaks from the SBN50 reference spectrum.

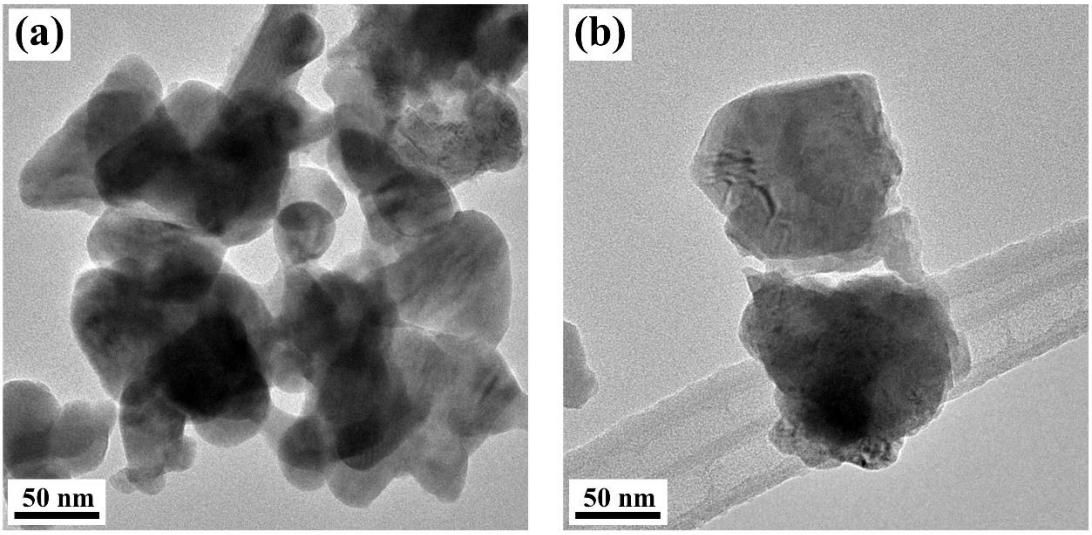

Fig. A3. (a) and (b) TEM images obtained for sol-gel derived SBN50 powder calcined at 800 °C.

Appendix B. Sinter-forging of SBN

The macroscopic properties of single crystalline SBN are known to be highly anisotropic, and improved dielectric and thermoelectric characteristics have been observed along the *c*-axis, the direction of ferroelectric polarization in SBN.[34,193] However, polycrystalline specimens are preferred over single crystals in practical applications due to the cost and difficulties associated with the single crystal growth process. While polycrystalline SBN samples do possess advantages in terms of processing, one significant drawback is that the random arrangement of grains in a polycrystalline structure hinders the full exploitation of enhanced TE properties along the *c*-axis. One route to bridging the gap between the long-range order of single crystals and the random, relatively shorter range of order in polycrystalline SBN is to synthesize textured polycrystalline specimens with preferred [00*l*] orientation.

Due to its simplicity, effectiveness, and compatibility with current processing protocols, the technique of sinter-forging was chosen to induce texturing in polycrystalline SBN specimens. Here, a uniaxial compressive load is applied to cold-pressed pellets during sintering to promote anisotropic grain growth. Over the time that the load is applied, grain growth is inhibited in the direction of pressing and, since SBN crystals grow preferentially along the [001] direction,[194] polycrystalline specimens with (00*l*) planes oriented perpendicular to the pressing direction may be produced. In addition to the alignment of NbO_6 octahedra, grain boundary scattering may be minimized after sinter-forging due to the growth of elongated grains in the [001] direction.

Initial sinter-forging experiments for SBN50 were conducted at 1250 °C under a pressure of 1 MPa applied for 4 h. However, XRD characterization revealed no [00*l*] texturing. After increasing the pressure to 10 MPa at the same temperature, some possible texturing was observed, but overall the results were inconclusive. Ultimately, it was found that an increase in the sintering

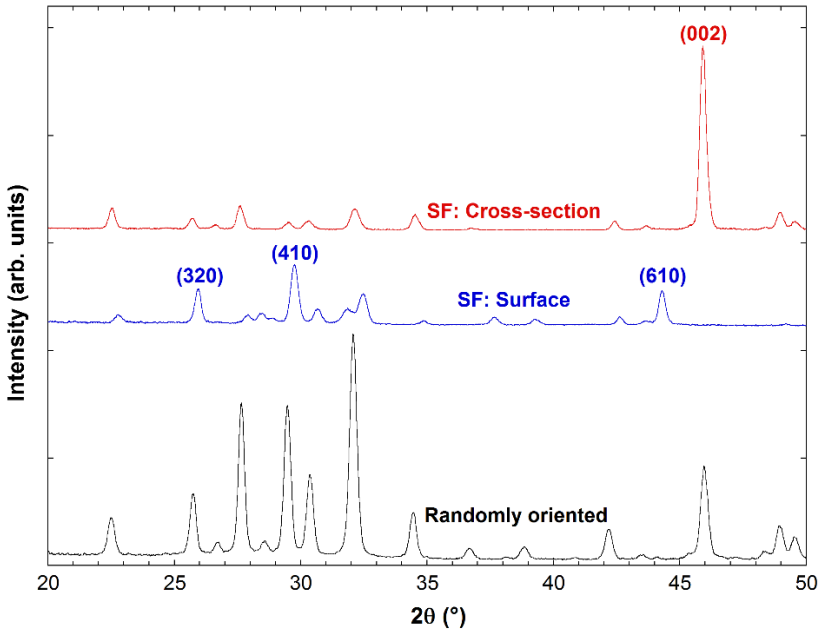

Fig. B1. XRD patterns obtained for SBN50 sinter-forged at 1300 °C under a pressure of 10 MPa; the pattern for randomly-oriented SBN50 is included for comparison. The spectrum labeled "SF: Surface" was acquired from the specimen surface with a normal parallel to the pressing direction, while the pattern denoted as "SF: Cross-section" was obtained from the surface with a normal perpendicular to the pressing direction.

temperature had a profound effect on the degree of texture. This is evident by noting that the reflections of maximum intensity in randomly-oriented, polycrystalline SBN are produced from (311) planes. By increasing the sinter-forging temperature from 1250 to 1300 °C, the (311):(002) peak intensity ratio decreased by more than an order of magnitude, from 1.46 to 0.12. The XRD patterns obtained from SBN50 sinter-forged at 1300 °C under 10 MPa of pressure are shown in Fig. B1; the pattern for randomly-oriented, single-phase SBN50 is included for comparison. Here, "SF: Surface" denotes the XRD spectrum acquired from the specimen surface with a normal parallel to the pressing direction, while "SF: Cross-section" denotes the XRD data obtained from the sample cross-section, i.e., the surface with a normal perpendicular to the pressing direction. As evident in the figure, reflections from (*hk*0) planes have maximum intensity in the XRD pattern of the sample surface, while the XRD data from the specimen cross-section is dominated by a large (002) peak.

Appendix C. SBN with a bi-modal grain distribution

In this section, the fabrication of composite SBN specimens consisting of micro- and nano-sized SBN particles will be detailed. The goal when employing such structures in TE applications would be to induce a sort of percolation effect, where electrons "select" the path of lowest resistance when moving through the material.[72] In this case, the path of least resistance would be an interconnected channel of larger SBN grains, which can be established by the incorporation of micro-sized SBN particles produced via solid-state synthesis. At the same time, the motion of phonons is dictated by the lattice and, due to the presence of SBN nanoparticles (fabricated via SCS), low values of κ may be maintained due to phonon scattering. A certain volume percentage of nanoparticles in the specimens may also serve to increase the Seebeck coefficient via the energy filtering mechanism. To preserve a bimodal grain structure during densification of the composites, spark plasma sintering (SPS) was employed, as the fast sintering times associated with the technique serve to limit grain growth while producing a dense final product.

A conventional solid-state synthesis method was employed to fabricate micron-sized SBN50 powder. Here, $BaCO_3$, $SrCO_3$, and Nb_2O_5 were milled for 48 h in ethanol using yttria-stabilized zirconia media. The mixture was then dried at 80 °C and calcined for 3 h at 1200 °C in air. Examination of the powder with a Horiba LA-950 particle size analyzer showed the average particle diameter to be ~ 5μm. Displayed in Fig. C1 are SEM images obtained for spark plasma sintered specimens produced from 100% nanoparticles, 50% nanoparticles-50% micron-sized powders, and 100% micron-sized powder, respectively. The difference in the grain structure of the specimens is quite evident.

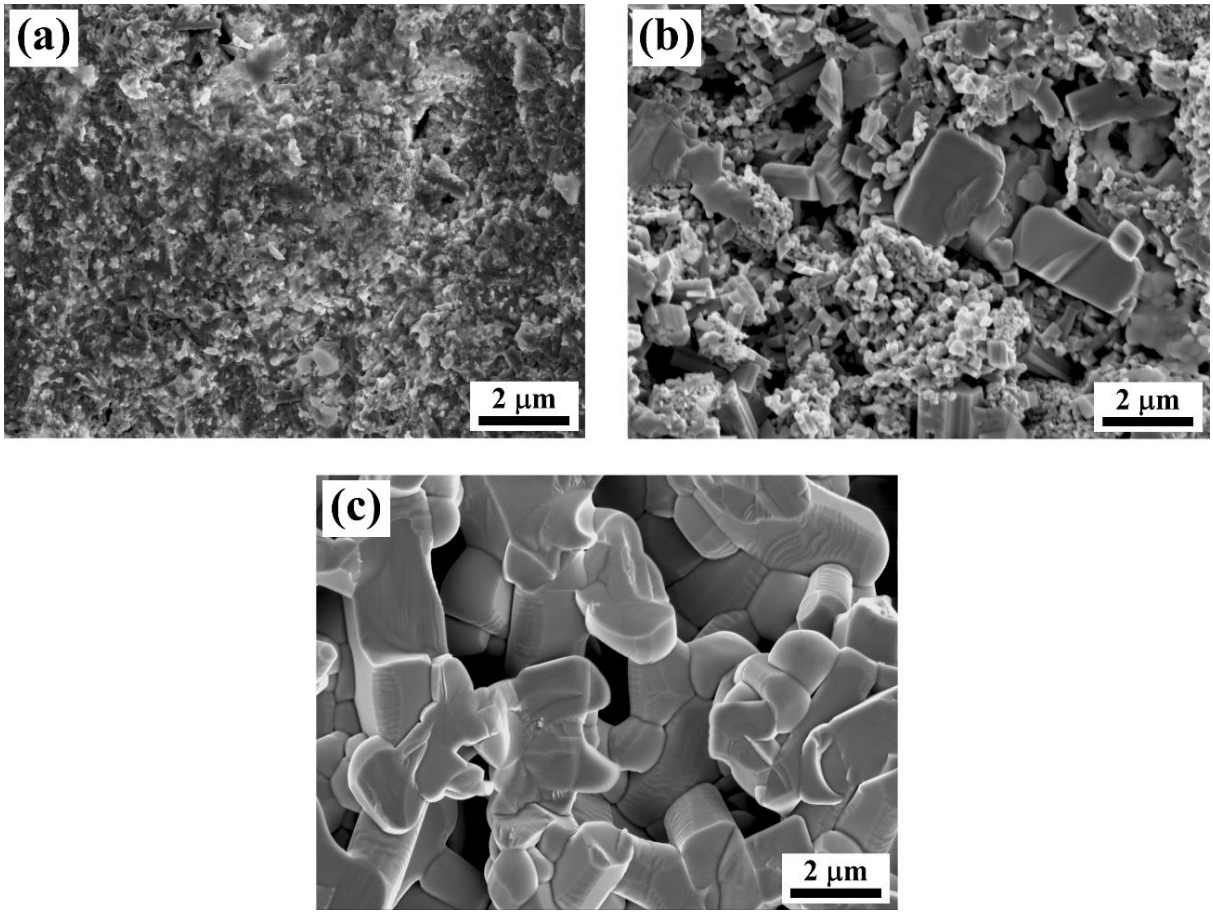

Fig. C1. SEM images of spark plasma sintered SBN pellets made from (a) 100% nanoparticles, (b) 50% nanoparticles and 50% micro-sized particles, and (c) 100% micron-sized particles.

References

1 A. Shakouri, Annual Review of Materials Research **41,** 399-431 (2011).

2 D. M. Rowe, Renewable Energy **16,** 1251-1256 (1999).

3 K. Koumoto, I. Terasaki, and R. Funahashi, MRS Bulletin **31,** 206-210 (2006).

4 T. M. Tritt, Annual Review of Materials Research **41,** 433-448 (2011).

5 H. J. Goldsmid, in *CRC Handbook of Thermoelectrics*, edited by D. M. Rowe (CRC Press, New York, 1995).

6 J. Androulakis, P. Migiakis, and J. Giapintzakis, Applied Physics Letters **84,** 1099-1101 (2004).

7 F. J. DiSalvo, Science **285,** 703-706 (1999).

8 L. E. Bell, Science **321,** 1457-1461 (2008).

9 D. M. Rowe, International Journal of Innovations in Energy Systems and Power **1,** 13-23 (2006).

10 G. Min and D. M. Rowe, Journal of Power Sources **38,** 253-259 (1992).

11 D. M. Rowe and G. Min, Journal of Power Sources **73,** 193-198 (1998).

12 G. J. Snyder and E. S. Toberer, Nature Materials **7,** 105-114 (2008).

13 C. B. Satterthwaite and R. W. Ure Jr., Physical Review **108,** 1164-1170 (1957).

14 R. J. Lewis, *Sax's Dangerous Properties of Industrial Materials*, Vol. 2, 8th ed. (Van Nostrand Reinhold, New York, 1992).

15 H. Goldsmid, Materials **7,** 2577-2592 (2014).

16 X. W. Wang, H. Lee, Y. C. Lan, G. H. Zhu, G. Joshi, D. Z. Wang, J. Yang, A. J. Muto, M. Y. Tang, J. Klatsky, S. Song, M. S. Dresselhaus, G. Chen, and Z. F. Ren, Applied Physics Letters **93** (2008).

17 K. Koumoto, Y. Wang, R. Zhang, A. Kosuga, and R. Funahashi, Annual Review of Materials Research **40,** 363-394 (2010).

18 J. He, Y. Liu, and R. Funahashi, Journal of Materials Research **26,** 1762-1772 (2011).

19 M. Ohtaki, H. Koga, T. Tokunaga, K. Eguchi, and H. Arai, Journal of Solid State Chemistry **120,** 105-11 (1995).

20 I. Terasaki, Y. Sasago, and K. Uchinokura, Physical Review B **56,** 12685-12687 (1997).

21 M. Ito, T. Nagira, D. Furumoto, S. Katsuyama, and H. Nagai, Scripta Materialia **48,** 403-408 (2003).

22 Y. Wang, Y. Sui, J. Cheng, X. Wang, and W. Su, Journal of Alloys and Compounds **477,** 817-821 (2009).

23 J. Sui, J. Li, J. He, Y.-L. Pei, D. Berardan, H. Wu, N. Dragoe, W. Cai, and L.-D. Zhao, Energy & Environmental Science **6,** 2916-2920 (2013).

24 M. Ohtaki and R. Hayashi, in *Enhanced Thermoelectric Performance of Nanostructured ZnO: A possibility of selective phonon scattering and carrier energy filtering by nanovoid structure*, Vienna, 2006, p. 276-279.

25 L. Bocher, M. H. Aguirre, D. Logvinovich, A. Shkabko, R. Robert, M. Trottmann, and A. Weidenkaff, Inorganic Chemistry **47,** 8077-8085 (2008).

26 A. M. Glass, Applied Physics Letters **13,** 147 (1968).

27 M. D. Ewbank, R. R. Neurgaonkar, W. K. Cory, and J. Feinberg, Journal of Applied Physics **62,** 374-380 (1987).

28 P. V. Lenzo, Applied Physics Letters **11,** 23 (1967).

[29] S. Lee, J. A. Bock, S. Trolier-McKinstry, and C. A. Randall, Journal of the European Ceramic Society **32,** 3971-3988 (2012).
[30] K. H. Lee, S. W. Kim, H. Ohta, and K. Koumoto, Journal of Applied Physics **101,** 083707 (2007).
[31] Y. Lu, K. Sagara, L. Hao, Z. Ji, and H. Yoshida, Materials Transactions **53,** 1208-1211 (2012).
[32] S.-H. Park and H.-I. Yoo, Physical chemistry chemical physics **11,** 391-401 (2009).
[33] J. A. Bock, S. Trolier-McKinstry, G. D. Mahan, and C. A. Randall, Physical Review B **90,** 115106 (2014).
[34] S. Lee, R. H. T. Wilke, S. Trolier-McKinstry, S. J. Zhang, and C. A. Randall, Applied Physics Letters **96** (2010).
[35] A. Sakai, T. Kanno, K. Takahashi, Y. Yamada, and H. Adachi, Journal of Applied Physics **108** (2010).
[36] T. J. Seebeck, Abhandlungen der Königlichen Akademie der Wissenschaften zu Berlin aus den Jahren 1820-1821**,** 289-346 (1822).
[37] T. J. Seebeck, Abhandlungen der Königlichen Akademie der Wissenschaften zu Berlin. Aus den Jahren 1822 und 1823**,** 265-373 (1825).
[38] N. Hawkins, *Hawkins Electrical Guide, Number One* (Theo Audel & Co., New York, 1914).
[39] E. Velmre, Proceedings of the Estonian Academy of Sciences Engineering **13,** 276-282 (2007).
[40] R. E. Bentley, *The Theory and Practice of Thermoelectric Thermometry*, Vol. 3 (Springer, Singapore, 1998).
[41] H. C. Oersted, Journal für Chemie und Physik **29,** 275-281 (1820).
[42] J. Martin, T. Tritt, and C. Uher, Journal of Applied Physics **108** (2010).
[43] G. Bakan, N. Khan, H. Silva, and A. Gokirmak, Scientific Reports **3,** 1-5 (2013).
[44] T. D. Sparks, Ph.D. Thesis, Harvard University, 2012.
[45] W. D. Callister, *Materials Science and Engineering: An Introduction*, 7th ed. (John Wiley & Sons, New York, 2007).
[46] J. C. Peltier, Annales de Chimie et de Physique **56,** 371-386 (1834).
[47] D. M. Rowe, in *CRC Handbook of Thermoelectrics*, edited by D. M. Rowe (CRC Press, Boca Raton, 1995).
[48] A. P. Gonçalves and C. Godart, in *New Materials for Thermoelectric Applications: Theory and Experiment*, edited by V. Zlatić and A. C. Hewson (Springer, Dordrecht, 2013).
[49] A. F. Ioffe, *Semiconductor Thermoelements and Thermoelectric cooling* (Infosearch, Ltd., London, 1957).
[50] K. Koumoto, R. Funahashi, E. Guilmeau, Y. Miyazaki, A. Weidenkaff, Y. Wang, and C. Wan, Journal of the American Ceramic Society **96,** 1-23 (2013).
[51] C. Wood, Energy Conversion and Management **24,** 317-329 (1984).
[52] T.-t. E. Chan, J. M. LeBeau, R. Venkatasubramanian, P. Thomas, J. Stuart, and C. C. Koch, Applied Physics Letters **103,** 144106 (2013).
[53] N. W. Ashcroft and N. D. Mermin, *Solid State Physics*, 1st ed. (Holt, Rinehart and Winston, Philadelphia, 1976).
[54] H. Fritzsche, Solid State Communications **9,** 1813-1815 (1971).
[55] T. M. Tritt and M. A. Subramanian, MRS Bulletin **31,** 188-194 (2006).

[56] A. J. Minnich, M. S. Dresselhaus, Z. F. Ren, and G. Chen, Energy & Environmental Science **2,** 466-479 (2009).
[57] J. P. Heremans, V. Jovovic, E. S. Toberer, A. Saramat, K. Kurosaki, A. Charoenphakdee, S. Yamanaka, and G. J. Snyder, Science **321,** 554-557 (2008).
[58] L. D. Hicks and M. S. Dresselhaus, Physical Review B **47,** 16631-16634 (1993).
[59] J. P. Heremans, Acta Physica Polonica A **108,** 609-634 (2005).
[60] J. P. Heremans, C. M. Thrush, and D. T. Morelli, Journal of Applied Physics **98,** 063703 (2005).
[61] G. D. Mahan and J. O. Sofo, Proceedings of the National Academy of Sciences of the United States of America **93,** 7436-7439 (1996).
[62] D. T. Morelli and G. P. Meisner, Journal of Applied Physics **77,** 3777-3781 (1995).
[63] B. C. Sales, D. Mandrus, and R. K. Williams, Science **272,** 1325-1328 (1996).
[64] T. C. Harman, M. P. Walsh, B. E. Laforge, and G. W. Turner, Journal of Electronic Materials **34,** L19-L22 (2005).
[65] W. Kim, J. Zide, A. Gossard, D. Klenov, S. Stemmer, A. Shakouri, and A. Majumdar, Physical Review Letters **96,** 045901 (2006).
[66] J. M. O. Zide, D. Vashaee, Z. X. Bian, G. Zeng, J. E. Bowers, A. Shakouri, and A. C. Gossard, Physical Review B **74,** 205335 (2006).
[67] J. L. Mi, X. B. Zhao, T. J. Zhu, and J. P. Tu, Applied Physics Letters **91,** 172116 (2007).
[68] T. Tsubota, M. Ohtaki, K. Eguchi, and H. Arai, Journal of Materials Chemistry **7,** 85-90 (1997).
[69] G. A. Slack, in *CRC Handbook of Thermoelectrics*, edited by D. M. Rowe (CRC Press, New York, 1995).
[70] G. A. Slack, in *Solid State Physics*; *Vol. 34*, edited by H. Ehrenreich, F. Seitz, and D. Turnbull (Academic Press, Inc., New York, 1979).
[71] K. Fujita, T. Mochida, and K. Nakamura, Japanese Journal of Applied Physics **40,** 4644-4647 (2001).
[72] J. F. Li, W. S. Liu, L. D. Zhao, and M. Zhou, NPG Asia Materials **2,** 152-158 (2010).
[73] S. Walia, S. Balendhran, H. Nili, S. Zhuiykov, G. Rosengarten, Q. H. Wang, M. Bhaskaran, S. Sriram, M. S. Strano, and K. Kalantar-zadeh, Progress in Materials Science **58,** 1443-1489 (2013).
[74] J. R. Sootsman, D. Y. Chung, and M. G. Kanatzidis, Angewandte Chemie International Edition **48,** 8616-8639 (2009).
[75] Y. Wang, N. S. Rogado, R. J. Cava, and N. P. Ong, Nature **423,** 425-428 (2003).
[76] W. Koshibae and S. Maekawa, Physical Review Letters **87,** 236603 (2001).
[77] W. Koshibae, K. Tsutsui, and S. Maekawa, Physical Review B **62,** 6869-6872 (2000).
[78] Data obtained from the "ISI Web of Knowledge" database with search option for topic "thermoelectric oxide" https://webofknowledge.com (accessed Jan. 30, 2015).
[79] N. V. Nong, C.-J. Liu, and M. Ohtaki, Journal of Alloys and Compounds **509,** 977-981 (2011).
[80] D. Wang, L. Chen, Q. Yao, and J. Li, Solid State Communications **129,** 615-618 (2004).
[81] T. Okuda, K. Nakanishi, S. Miyasaka, and Y. Tokura, Physical Review B **63,** 113104 (2001).
[82] O. Yamashita, S. Tomiyoshi, and K. Makita, Journal of Applied Physics **93,** 368-374 (2003).
[83] A. Nag and V. Shubha, Journal of Electronic Materials **43,** 962-977 (2014).

[84] H. Muta, K. Kurosaki, and S. Yamanaka, Journal of Alloys and Compounds **350,** 292-295 (2003).
[85] S. Ohta, H. Ohta, and K. Koumoto, Journal of the Ceramic Society of Japan **114,** 102-105 (2006).
[86] J. F. Wager, D. A. Keszler, and R. E. Presley, *Transparent Electronics* (Springer Science and Business Media, New York, 2007).
[87] D. Berardan, E. Guilmeau, A. Maignan, and B. Raveau, Solid State Communications **146,** 97-101 (2008).
[88] M. Ohtaki, Journal of the Ceramic Society of Japan **119,** 770-775 (2011).
[89] Y. Kinemuchi, M. Mikami, K. Kobayashi, K. Watari, and Y. Hotta, Journal of Electronic Materials **39,** 2059-2063 (2009).
[90] M. Ohtaki, K. Araki, and K. Yamamoto, Journal of Electronic Materials **38,** 1234-1238 (2009).
[91] H. Goldsmid, Materials **2,** 903-910 (2009).
[92] F. A. Kröger, *The Chemistry of Imperfect Crystals*, Vol. 2, 2nd ed. (American Elsevier Publishing Company, Inc., New York, 1974).
[93] S. Lambert, H. Leligny, and D. Grebille, Journal of Solid State Chemistry **160,** 322-331 (2001).
[94] Y. Miyazaki, K. Kudo, M. Akoshima, Y. Ono, Y. Koike, and T. Kajitani, Japanese Journal of Applied Physics **39,** L531-L533 (2000).
[95] G. Xu, R. Funahashi, M. Shikano, I. Matsubara, and Y. Zhou, Applied Physics Letters **80,** 3760-3762 (2002).
[96] M. I. Marques and C. Arago, Europhysics Letters **71,** 124-130 (2005).
[97] A. A. Bokov and Z.-G. Ye, Journal of Materials Science **41,** 31-52 (2006).
[98] P. B. Jamieson, S. C. Abrahams, and J. L. Bernstein, Journal of Chemical Physics **48,** 5048-5057 (1968).
[99] H. Y. Lee and R. Freer, Journal of Applied Physics **81,** 376-382 (1997).
[100] V. Gopalan, K. L. Schepler, V. Dierolf, and I. Biaggio, in *The Handbook of Photonics*, 2nd ed., edited by M. C. Gupta and J. Ballato (CRC Press, Boca Raton, 2007).
[101] N. Kobayashi, in *Preparation and Properties of Solid State Materials*; *Vol. 6*, edited by W. R. Wilcox (Marcel Dekker Inc., NY, 1981).
[102] C. Nikasch and M. Göbbels, Journal of Crystal Growth **269,** 324-332 (2004).
[103] C. L. Choy, W. P. Leung, T. G. Xi, Y. Fei, and C. F. Shao, Journal of Applied Physics **71,** 170 (1992).
[104] A. Speghini, M. Bettinelli, U. Caldino, M. O. Ramirez, D. Jaque, L. E. Bausa, and J. G. Sole, Journal of Physics D-Applied Physics **39,** 4930-4934 (2006).
[105] C. David, T. Granzow, A. Tunyagi, M. Wöhlecke, T. Woike, K. Betzler, M. Ulex, M. Imlau, and R. Pankrath, Physica Status Solidi (a) **201,** R49-R52 (2004).
[106] P. K. Patro, A. R. Kulkarni, and C. S. Harendranath, Journal of the European Ceramic Society **23,** 1329-1335 (2003).
[107] V. V. Shvartsman, B. Dkhil, and A. L. Kholkin, Annual Review of Materials Research **43,** 423-449 (2013).
[108] J. Dec, W. Kleemann, T. Woike, and R. Pankrath, The European Physical Journal B - Condensed Matter and Complex Systems **14,** 627-632 (2000).
[109] C. J. Huang, K. Li, X. Q. Liu, X. L. Zhu, and X. M. Chen, Journal of the American Ceramic Society **97,** 507-512 (2014).

[110] J. Zhang, G. Wang, F. Gao, C. Mao, F. Cao, and X. Dong, Ceramics International **39,** 1971-1976 (2013).
[111] D. Goldschmidt, Physical Review B **34,** 5558-5561 (1986).
[112] I. K. Naik and T. Y. Tien, Journal of Physics and Chemistry of Solids **39,** 311-15 (1977).
[113] C. Ruscher, E. Salje, and A. Hussain, Journal of Physics C: Solid State Physics **21,** 3737-3749 (1988).
[114] R. D. Averitt, Nature Physics **4,** 14-15 (2008).
[115] R. C. Buchanan, in *Ceramic Materials for Electronics*, 3rd ed., edited by R. C. Buchanan (Marcel Dekker, Inc., New York, 2004).
[116] J. Goodenough, Progress in Solid State Chemistry **5,** 145-399 (1971).
[117] M. Gao, R. Pankrath, S. Kapphan, and V. Vikhnin, Applied Physics B: Lasers and Optics **68,** 849-858 (1999).
[118] M. Gao, S. Kapphan, R. Pankrath, and J. Zhao, Physica Status Solidi B **217,** 999-1006 (2000).
[119] Y. Sun, X. Xu, and Y. Zhang, Journal of Physics: Condensed Matter **12,** 10475-10480 (2000).
[120] N. F. Mott and E. A. Davis, *Electronic Processes in Non-Crystalline Materials* 2nd ed. (Oxford University Press, New York, 1979).
[121] T. Holstein, Annals of Physics **8,** 343-389 (1959).
[122] T. Holstein, Annals of Physics **8,** 325-342 (1959).
[123] D. Adler, in *Solid State Physics*; *Vol. 21*, edited by F. Seitz, D. Turnbull, and H. Ehrenreich (Academic Press, Inc., New York, 1968).
[124] R. Koc and H. U. Anderson, Journal of Materials Science **27,** 5477-5482 (1992).
[125] S. Lee, S. Dursun, C. Duran, and C. A. Randall, Journal of Materials Research **26,** 26-30 (2011).
[126] J. G. Carrio, Y. P. Mascarenhas, W. Yelon, I. A. Santos, D. Garcia, and J. A. Eiras, Materials Research **5,** 57-62 (2002).
[127] S. B. Deshpande, H. S. Potdar, P. D. Godbole, and S. K. Date, Journal of the American Ceramic Society **75,** 2581-2585 (1992).
[128] P. K. Patro, R. Khatirkar, I. Samajdar, A. R. Kulkarni, and C. S. Harendranath, Journal of the European Ceramic Society **27,** 2255-2263 (2007).
[129] S. G. Lu, C. L. Mak, and K. H. Wong, Journal of the American Ceramic Society **84,** 79-84 (2001).
[130] S. G. Lu, C. L. Mak, and K. H. Wong, Journal of the American Ceramic Society **86,** 1333-1337 (2003).
[131] W. Sui, S. Luan, R. Song, and C. Wang, Journal of Ceramic Processing Research **12,** 716-720 (2011).
[132] Y. Li, J. P. Zhao, and B. Wang, Materials Research Bulletin **39,** 365-374 (2004).
[133] A. B. Panda, A. Pathak, and P. Pramanik, Bulletin of Materials Science **25,** 501-503 (2002).
[134] E. M. Rodriguez, A. Speghini, F. Piccinelli, L. Nodari, M. Bettinelli, D. Jaque, and J. G. Sole, Journal of Physics D-Applied Physics **42,** 102003 (2009).
[135] L. A. Chick, L. R. Pederson, G. D. Maupin, J. L. Bates, L. E. Thomas, and G. J. Exarhos, Materials Letters **10,** 6-12 (1990).
[136] J. J. Kingsley and K. C. Patil, Materials Letters **6,** 427-432 (1988).
[137] S. S. Manoharan and K. C. Patil, Journal of the American Ceramic Society **75,** 1012-1015 (1992).

[138] C. S. Dandeneau, T. W. Bodick, R. K. Bordia, and F. S. Ohuchi, Journal of the American Ceramic Society **96,** 2230-2237 (2013).
[139] P. K. Patro, A. R. Kulkarni, and C. S. Harendranath, Materials Research Bulletin **38,** 249-259 (2003).
[140] Y. Yang, Y. Liu, J. Meng, B. Dou, M. Hao, and X. Liu, Ferroelectrics **334,** 97-103 (2006).
[141] R. N. Das and P. Pramanik, Nanostructured Materials **11,** 325-330 (1999).
[142] J. M. Jehng and I. E. Wachs, Journal of Raman Spectroscopy **22,** 83-89 (1991).
[143] R. D. Bringans, M. A. Olmstead, R. I. G. Uhrberg, and R. Z. Bachrach, Physical Review B **36,** 9569-9580 (1987).
[144] S. R. Jain, K. C. Adiga, and V. R. P. Verneker, Combustion and Flame **40,** 71-79 (1981).
[145] D. A. Fumo, M. R. Morelli, and A. M. Segadaes, Materials Research Bulletin **31,** 1243-1255 (1996).
[146] C. S. Dandeneau, Y. Yang, B. W. Krueger, M. A. Olmstead, R. K. Bordia, and F. S. Ohuchi, Applied Physics Letters **104,** 101607 (2014).
[147] R. A. Fischer and H. Parala, in *Chemical Vapour Deposition: Precursors, Processes and Applications*, edited by A. C. Jones and M. L. Hitchman (The Royal Society of Chemistry, Cambridge, 2009), p. 417.
[148] R. F. Janninck and D. H. Whitmore, Journal of Physics and Chemistry of Solids **27,** 1183-1187 (1966).
[149] J. F. Moulder, W. F. Stickle, P. E. Sobol, and K. D. Bomben, in *Handbook of X-ray Photoelectron Spectroscopy*, edited by J. Chastain (Perkin-Elmer Corp., Eden Prarie, MN, 1992).
[150] S. Podlozhenov, H. A. Graetsch, J. Schneider, M. Ulex, M. Wohlecke, and K. Betzler, Acta Crystallographica Section B-Structural Science **62,** 960-965 (2006).
[151] R. Niemann, K. Buse, R. Pankrath, and M. Neumann, Solid State Communications **98,** 209-213 (1996).
[152] R. C. Baetzold, Physical Review B **48,** 5789-5796 (1993).
[153] E. Fischer, W. Hassler, and E. Hegenbarth, Physica Status Solidi A **72,** K169-K171 (1982).
[154] C. Kittel, Physical Review **75,** 972-974 (1949).
[155] D. Flahaut, T. Mihara, R. Funahashi, N. Nabeshima, K. Lee, H. Ohta, and K. Koumoto, Journal of Applied Physics **100** (2006).
[156] A. Janotti and C. G. Van de Walle, Physical Review B **76,** 165202 (2007).
[157] A. F. Kohan, G. Ceder, D. Morgan, and C. G. Van de Walle, Physical Review B **61,** 15019-15027 (2000).
[158] M. E. Manley, J. W. Lynn, D. L. Abernathy, E. D. Specht, O. Delaire, A. R. Bishop, R. Sahul, and J. D. Budai, Nature Communications **5** (2014).
[159] M. Tachibana and E. Takayama-Muromachi, Physical Review B **79,** 100104 (2009).
[160] S. Ke, H. Fan, H. Huang, H. L. W. Chan, and S. Yu, Journal of Applied Physics **104,** 024101 (2008).
[161] C. S. Pandey, J. Schreuer, M. Burianek, and M. Mühlberg, Physical Review B **87,** 094101 (2013).
[162] R. Dannenberg, S. Baliga, R. J. Gambino, A. H. King, and A. P. Doctor, Journal of Applied Physics **86,** 514-523 (1999).
[163] S. R. Gilbert, L. A. Wills, B. W. Wessels, J. L. Schindler, J. A. Thomas, and C. R. Kannewurf, Journal of Applied Physics **80,** 969-977 (1996).
[164] Q. R. Hou, B. F. Gu, and Y. B. Chen, Nano **6,** 167-171 (2011).

[165] D. Emin and T. Holstein, Physical Review Letters **36,** 323-326 (1976).
[166] A. Yildiz, F. Iacomi, and D. Mardare, Journal of Applied Physics **108,** 083701.
[167] A. Gerwens, K. Buse, E. Kratzig, N. Korneev, and S. Stepanov, Journal of the Optical Society of America B **15,** 2143-2146 (1998).
[168] K. Buse, A. Gerwens, S. Wevering, and E. Krätzig, Journal of the Optical Society of America B **15,** 1674-1677 (1998).
[169] D. Emin, Physical Review B **46,** 9419-9427 (1992).
[170] D. Emin, C. H. Seager, and R. K. Quinn, Physical Review Letters **28,** 813-816 (1972).
[171] H. L. Tuller and A. S. Nowick, Journal of Physics and Chemistry of Solids **38,** 859-867 (1977).
[172] W. Khan, A. H. Naqvi, M. Gupta, S. Husain, and R. Kumar, Journal of Chemical Physics **135,** 054501 (2011).
[173] E. Gorham-Bergeron and D. Emin, Physical Review B **15,** 3667-3680 (1977).
[174] N. F. Mott, Philosophical Magazine **19,** 835-852 (1969).
[175] N. F. Mott, Journal of Non-Crystalline Solids **8-10,** 1-18 (1972).
[176] D. Emin, Physical Review Letters **32,** 303-307 (1974).
[177] A. Miller and E. Abrahams, Physical Review **120,** 745-755 (1960).
[178] G. Mattausch, T. Felsner, E. Hegenbarth, B. Kluge, and S. Sahling, Phase Transitions **59,** 189-223 (1996).
[179] V. Ambegaokar, B. I. Halperin, and J. S. Langer, Physical Review B **4,** 2612-20 (1971).
[180] L. Pichon, E. Jacques, R. Rogel, A. C. Salaun, and F. Demami, Semiconductor Science and Technology **28,** 025002 (2013).
[181] T.-T. Fang and H.-Y. Chung, Applied Physics Letters **94,** 092905 (2009).
[182] N. Mott, Proceedings of the Royal Society of London. Series A, Mathematical and Physical Sciences **382,** 1-24 (1982).
[183] P. W. Anderson, Physical Review **109,** 1492-1505 (1958).
[184] T. Siegrist, P. Jost, H. Volker, M. Woda, P. Merkelbach, C. Schlockermann, and M. Wuttig, Nature Materials **10,** 202-208 (2011).
[185] P. Meredith, C. J. Bettinger, M. Irimia-Vladu, A. B. Mostert, and P. E. Schwenn, Reports on Progress in Physics **76,** 034501 (2013).
[186] N. Mott, Journal of Physics C: Solid State Physics **20,** 3075-3102 (1987).
[187] M. H. Cohen, H. Fritzsche, and S. R. Ovshinsky, Physical Review Letters **22,** 1065-1068 (1969).
[188] R. Moos, A. Gnudi, and K. H. Hardtl, Journal of Applied Physics **78,** 5042-5047 (1995).
[189] E. W. Lemmon and R. T. Jacobsen, International Journal of Thermophysics **25,** 21-69 (2004).
[190] W. M. Kim, Y. H. Kim, J. S. Kim, J. Jeong, Y. J. Baik, J. K. Park, K. S. Lee, and T. Y. Seong, Journal of Physics D-Applied Physics **43,** 365406 (2010).
[191] S. Wanmei, L. Shijun, S. Ranran, and W. Chunlong, Journal of Ceramic Processing Research **12,** 716-720 (2011).
[192] Y. Narendar and G. L. Messing, Chemistry of Materials **9,** 580-587 (1997).
[193] W. H. Huang, D. Viehland, and R. R. Neurgaonkar, Journal of Applied Physics **76,** 490-496 (1994).
[194] J. P. Wilde, D. H. Jundt, L. Galambos, and L. Hesselink, Journal of Crystal Growth **114,** 500-506 (1991).